Title
Understanding iceberg and glacier melt from ocean observations in Greenland fjords

Author
Lindeman, Margaret Ruth

Publication Date
2022

UNIVERSITY OF CALIFORNIA SAN DIEGO

Understanding iceberg and glacier melt from ocean observations in Greenland fjords

A dissertation submitted in partial satisfaction of the
requirements for the degree Doctor of Philosophy

in

Oceanography

by

Margaret Ruth Lindeman

Committee in charge:

Professor Fiamma Straneo, Chair
Professor Jennifer A. Burney
Professor Helen A. Fricker
Professor Sarah N. Giddings
Professor Jennifer A. MacKinnon
Professor Amina T. Schartup

2022

The Dissertation of Margaret Ruth Lindeman is approved, and it is acceptable in quality and form for publication on microfilm and electronically.

University of California San Diego

2022

EPIGRAPH

You can't think of your troubles while solving a crossword.

Margaret Farrar
New York Times Crossword editor, 1942-69

Icy hazard at sea
On the surface it might not look like much
Name suffix meaning "mountain"
North Atlantic shipping menace
The Titanic's undoing
Block at sea
Icy detachment
Rescue site for a polar bear
Floating mass in the North Atlantic
What the Titanic had a disastrous encounter with
Danger for a submarine
Something coming off the shelf?
Former piece of an ice shelf
Chunk of ice in the ocean
Floating block of ice

New York Times Crossword clues for BERG, *September 2016–May 2022*
ed. Will Shortz
compiled by XWord Info

TABLE OF CONTENTS

LIST OF FIGURES

LIST OF TABLES

ACKNOWLEDGMENTS

It's a given that my advisor, Fiamma Straneo, is a brilliant and creative scientist, but my favorite thing about working with her has been that she is a good person and she works with good people. I am so grateful for the opportunities I have had and connections I have made as part of her group, and I look forward to many reunions to come. Fiamma, thank you for bringing me on board and sticking with me through some rough patches. Thanks also to Rosalba Ciampi and Yani & Kea for making me feel so welcome, from Falmouth to Mission Hills.

Working with my all-star committee has been such a privilege. Helen Fricker was the first professor I contacted at Scripps and has been an integral part of my time here as the co-leader of our ice-ocean group and champion of the Scripps Polar Center. I was fortunate to take two courses with Sarah Giddings, who is a fantastic teacher on top of her formidable estuarine expertise. Jen MacKinnon, Bobby and I have had a nice email you sent us during your excellent Arctic Ocean seminar course taped to our office wall for the past 3 years. Jen Burney has the most incredible range of knowledge and even joined my qualifying exam remotely from her sabbatical in France. Amina Schartup entrusted me with an extremely cool project and has been so supportive as I've stumbled my way through basic trace metal chemistry. Mary-Louise Timmermans, who was originally on my committee, is another scientific heavy hitter who (along with Andrew Wells) nevertheless spent a lot of the summer of 2017 working patiently with me and helping me build confidence when I desperately needed it. I am so grateful to all of you for being so generous with your time, energy, and knowledge.

It's safe to say I wouldn't be an oceanographer if it weren't for Collin Roesler, whom I met on my first day at Bowdoin College in 2011, and impossible to know where I would have landed if Mary-Lou Zeeman hadn't found me my first opportunity to do fieldwork in West Greenland in 2014. David and Denise Holland of NYU took me along on an amazing research cruise in Disko Bay — probably the only thing that could have pulled me away from working with the lovely Jim Hench of the Duke Marine Lab, who hosted me for an REU in 2013. Michael King, Emily Peterman, and Cathryn Field, among many others at Bowdoin, also had indelible impacts on my growth as a scientist. Olaf Boebel, Ralph Timmermann, and Torsten Kanzow at the Alfred Wegener Institut in Bremerhaven, Germany took me on as a fresh college graduate and gave me my first taste of full-time research. They also put me in an office with Janin Schaffer and Svenja Ryan, for whose friendship I will always be thankful!

Fiamma has built a wonderful group at Scripps since 2017, starting with Jamie Holte, who is the glue that keeps everything together, and has always been willing to help me out with research, have a cup of coffee, or even whip cream by hand when needed. Our postdocs Tiago Biló, Isabela Le Bras, Donald Slater, and Till Wagner have been fantastic mentors and friends, even as they have moved on to new positions. I have been so lucky to work with and learn from the other students in our group, Alex Hamel, Monica "Clean Hands" Nelson, Aurora Roth, and Bobby Sanchez. The addition of Helen's group (Susheel Adusumilli, Philipp Arndt, Maya Becker, Marnie Bryant, Chloe Gustafson, and Cyrille Mosbeux), other Scripps Polar folks (including Momme Hell and Hayden Johnson), and visitors like Marta Faulkner, Morven Muilwijk, Lars Henrik Smedsrud, and Dave Sutherland, among many others, made the group environment even richer (and more fun). And thank you to everyone "behind the scenes" at Scripps, including Blanca Aguilar, Diane Boomer, Gilbert Bretado, Maureen McGreevy, Sean Pfeiffer, Tomomi Ushii, Shelley Weisel, and Lauren Wood.

I am grateful also to everybody involved in my two field seasons in Sermilik Fjord, especially MIMEX co-PIs Claudia Cenedese and Hanu Singh, and Donald Slater, who was there for the lowest lows and the highest highs. Special gratitude is owed to the crew of the M/V Adolf Jensen, from Qaqortoq, South Greenland: my final two chapters would never have happened without Louie and Anders, in particular. Thanks to the organizers and attendees of the 2017 WHOI Geophysical Fluid Dynamics summer school, the 2018

"Ice Disko" winter school in Qeqetarsuaq, West Greenland, and the 2019 Advanced Climate Dynamics Course in Yosemite (especially Morven Muilwijk, who was at all three of them).

I am so fortunate to have started at Scripps with the most wonderful cohort imaginable, the "Yakpen": Will Chapman, Luke Kachelein, Mike Kovatch, Ratnaksha Lele, Jacob Morgan, Theresa Morrison, Jessica Ng, and Mike Sierks. Thanks also to my PO mentors Isa Arzeno and Bia Villas Boas, and the many other students I have been so lucky to share my time here with, as well as my housemates over the years, Hunter Akins, Dillon Amaya, Julia Dohner, MacKenzie Elmer, Momme Hell, Kim McComas (and Dany), Carrie McIntosh, Jacob Morgan, Theresa Morrison, and Max Rintoul. Thanks to the Data Lagers (Derek Alcorn, Emma Beer, Dan Blatter, Nick Lau, Emma & Casey Wall, Zoe Yin, et al.) for all the mandatory fun, my All We Can Save circle (especially Bonnie Ludka for initiating the group) for your thoughtful and compassionate companionship during a difficult season, and everyone at the Pannikin for giving me a "third place" when I needed one. Zoe Walker, the months we had you here were some of my most fun and memorable times in San Diego. Bobby, Susheel, and Maya, thank you for sticking with me through many long months and years in the basement (and on Zoom, and in various public parks, and so on) — your insights and friendship shaped my Scripps experience in the best ways. Jacob, thank you for your steady support and the adventures we shared. Theresa, I could never have dreamed a more brilliant, funny, kind partner-in-PO (etc.) than you. Art nights and retreats and dinners with you and Jessica have buoyed me at some of the lowest moments. Annie Adelson, you're always gold to me.

To my family, especially my parents, Lucy and Mark, my sister Harriet, and my grandparents, Mike, Pam, Sharon, and Dan, as well as all of my aunts, uncles, cousins, and chosen family: living far away from you is the worst part of this whole thing, and I am so grateful to you for always welcoming me home so generously. Thank you for your support, encouragement, and enthusiasm for my next steps. I miss you all terribly — especially Tom, Joan, and Peggy — and love you more than I can express.

“The UC San Diego community holds great respect for the land and the original people of the area where our campus is located. The university is built on the un-ceded territory of the Kumeyaay Nation. Today, the Kumeyaay people continue to maintain their political sovereignty and cultural traditions as vital members of the San Diego community. We acknowledge their tremendous contributions to our region and thank them for their stewardship.” — the UC San Diego Intertribal Resource Center

Chapter 3, in full, is a reprint of the material as it appears in Journal of Geophysical Research: Oceans, 2020. DOI:10.1029/2020JC016091. Margaret R. Lindeman, Fiammetta Straneo, Nat J. Wilson, John M. Toole, Richard A. Krishfield, Nicholas L. Beaird, Torsten Kanzow, and Janin Schaffer. The dissertation author was the primary investigator and author of this paper.

Chapter 4 is currently in preparation to be submitted for publication. The dissertation author was the primary investigator and author of this material.

Chapter 5 is currently in preparation to be submitted for publication. Margaret R. Lindeman, Fiammetta Straneo, Amina Schartup, Hannah M. Adams, and Monica J.S. Nelson. The dissertation author was the primary investigator and author of this material.

VITA

2015	B.A., Earth & Oceanographic Science and Mathematics, Bowdoin College
2018	M.S., Scripps Institution of Oceanography, University of California San Diego
2022	Ph.D., Scripps Institution of Oceanography, University of California San Diego

ABSTRACT OF THE DISSERTATION

Understanding iceberg and glacier melt from ocean observations in Greenland fjords

by

Margaret Ruth Lindeman

Doctor of Philosophy in Oceanography

University of California San Diego, 2022

Professor Fiamma Straneo, Chair

The glacial fjords that connect the Greenland Ice Sheet to the North Atlantic control ocean heat transport toward the ice sheet and the downstream fate of glacier meltwater. This thesis builds on a growing body of research into Greenland fjord dynamics, focusing on aspects of glacier-fjord systems that are especially challenging to observe: sub-annual ocean variability beneath a floating ice tongue; iceberg meltwater properties and distribution; and the distribution and cycling of environmental mercury.

Ice discharge to the ocean can be moderated by ice tongues, floating extensions of glaciers that buttress the upstream ice flow. In Chapter 3, an ice-tethered mooring record from beneath the 79 North Glacier ice tongue shows that ocean warming observed on the continental shelf is advected into the fjord and reaches the glacier grounding line within 6 months, indicating that basal melt of the ice tongue is sensitive to regional ocean variability.

Icebergs calved from tidewater glaciers are a major component of fjord freshwater and heat budgets in fjords, but there are few observations to constrain iceberg melt models. In Chapter 4, meltwater plume intrusions are identified based on their temperature and salinity properties in two surveys of a large iceberg in Sermilik Fjord in southeast Greenland. The intrusions are distributed around the iceberg between 80-250 m depth and drive upwelling over vertical scales averaging 15-50 m, with the plume height primarily controlled by stratification. A standard melt plume model does not recreate the observed melt concentrations even with adjustments to the model coefficients, suggesting that more substantial modifications to the model physics are needed to accurately simulate iceberg melt and upwelling.

In Chapter 5, results from a recent survey in Sermilik Fjord show that glacially modified waters are depleted in the toxic trace element mercury relative to regional ocean waters, indicating that glacier melt is not a significant source of environmental mercury in that system. We hypothesize that mercury is removed from the water column in the ice melange region near the glacier terminus through scavenging and settling of suspended sediments from iceberg melt and runoff.

Chapter 1

Introduction

1.1 Background

Beginning in the late 1990s, mass loss from the Greenland Ice Sheet (GrIS) accelerated significantly, increasing the rate of global sea level rise. Changes in ice sheet mass are determined by the surface mass balance, the difference between snow accumulation and atmosphere-driven surface melt runoff, and by discharge, which is the loss of ice directly to the ocean through iceberg calving and ocean melting of glacier termini.

Particularly striking changes were observed at marine-terminating glaciers, many of which retreated dramatically (Figure 1.1). These dynamic changes at the ice sheet margins brought increased attention to the role of glacial fjords, which connect the ice sheet to the ocean. It is hypothesized that ocean warming could have triggered the observed acceleration of GrIS glaciers, and on the other side, that the increased freshwater flux to the North Atlantic could affect ocean circulation.

Two underlying questions therefore motivate research into ice-ocean interactions in Greenland's fjords. First, how do fjord processes control the supply of ocean heat to glacier termini? Second, how do they modify the properties of glacier melt that is exported to the ocean?

1.2 Greenland: the world's largest island

The GrIS is vast and complex, but its dynamics are sensitive to changes at its margins, where marine-terminating glaciers meet the ocean within fjords. The ocean properties on the continental shelf, in turn, are set further afield, beginning with processes in the subtropical Atlantic and Arctic Oceans (Figure 1.1).

1.2.1 Ocean properties on the northeast Greenland shelf

Warm, salty waters from the subtropical Atlantic Ocean are transported by the North Atlantic Current to the eastern limb of the cyclonic Irminger Gyre (Våge et al., 2011; Straneo et al., 2012). Here the Irminger Current bifurcates, with a fraction of the Atlantic Water (AW) transported to the north by the Norwegian-West Spitsbergen Current system. The current again divides near Fram Strait, where about half of the AW recirculates and returns southward in the East Greenland Current (EGC; Marnela et al., 2013; de Steur et al., 2014; Hattermann et al., 2016). Some of this AW is transported onto the continental shelf, where it mixes with colder, fresher waters exported from the Arctic Ocean, forming Atlantic Intermediate Water (AIW; Bourke et al., 1987; Budéus and Schneider, 1995). Cold, fresh Arctic waters are exported through Fram Strait and then transported southward along the continental shelf, where they are freshened further by sea ice melt and GrIS meltwater runoff, creating Polar Water (PW; Håvik et al., 2017).

At Nioghalvfjerdsfjorden (79 North Fjord) in northeast Greenland (Figure 1.1), the floating ice tongue, which is about 100 m deep at the calving front, effectively blocks shallow PW from entering the cavity (Wilson and Straneo, 2015). AIW is therefore the primary shelf water mass in the fjord. The AIW inflow, and thus the heat supply toward the ice tongue, is hydraulically controlled by a sill near the calving front, which makes it sensitive to remotely-forced fluctuations in the thickness of the water mass layers on the shelf (Schaffer et al., 2020; Zhao et al., 2019; Münchow et al., 2020).

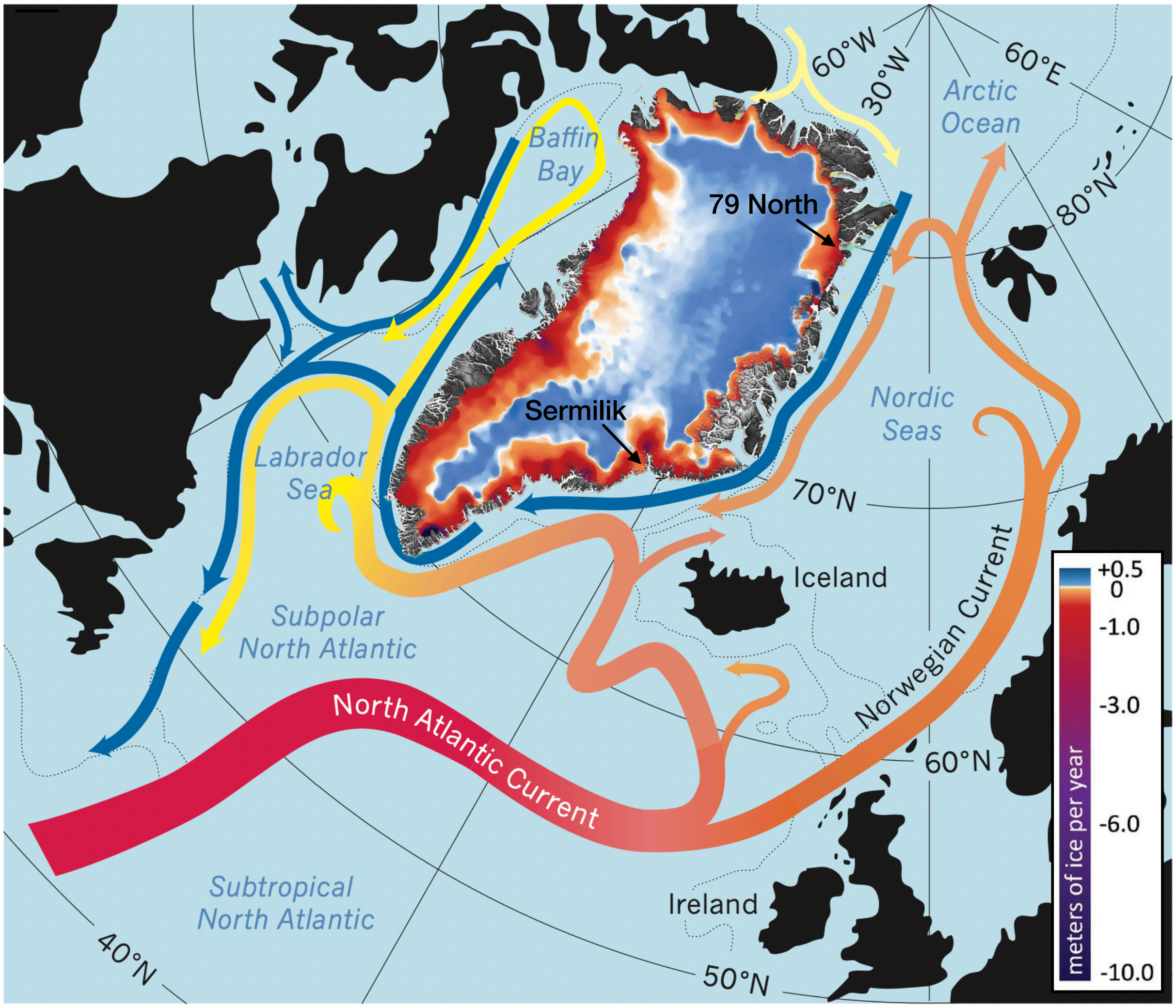

Figure 1.1. Schematic of large-scale ocean circulation around Greenland (Straneo et al., 2013) with ice sheet mass loss between 2003 and 2019 (Smith et al., 2020). 79 North Fjord (the setting for Chapter 3) and Sermilik Fjord (the setting for Chapters 4 and 5) are labeled.

1.2.2 Ocean properties on the southeast Greenland shelf

When the Irminger Current bifurcates near the Denmark Strait, the majority of the AW recirculates to the west and flows southward with the East Greenland Current along the continental shelf break. The East Greenland Coastal Current (EGCC) carries PW south along the continental shelf from the Denmark Strait to Cape Farewell (Sutherland and Pickart, 2008; Le Bras et al., 2018).

The ocean waters that flow into Sermilik Fjord from the continental shelf in southeast Greenland are primarily comprised of warm, salty AW below a permanent pycnocline at around 160 m depth, with a PW layer above (Straneo et al., 2010, 2012). During the winter, exchange between the fjord and the shelf is primarily driven by shelf variability, particularly wind-driven fluctuations of the pycnocline depth (Jackson et al., 2014; Sanchez et al., 2021). During the summer, winds are weaker and seasonally-enhanced export of glacially modified waters (GMW) above the pycnocline sustains a buoyancy-driven exchange flow (Straneo et al., 2011; Jackson and Straneo, 2016).

1.3 Progress on understanding glacier-ocean interactions in Greenland fjords

1.3.1 Helheim Glacier and Sermilik Fjord: a tidewater glacier–fjord system

The majority of Greenland's marine-terminating glaciers are tidewater glaciers, which have a vertical calving front in contact with the ocean (Figure 1.2a). Helheim Glacier is the largest outlet glacier in southeast Greenland, and terminates at the head of Sermilik Fjord (Figure 1.1). Ocean heat drives melting of the glacier terminus and calved icebergs throughout the year, with some variability in melt rates due to changes in the ocean water mass properties and strength of the exchange flow. Melting ice requires a significant latent heat input, which in these contexts is supplied by the ocean, driving substantial cooling. The resulting cold melt mixture is referred to as submarine melt water (SMW).

The largest driver of seasonal variability in the Helheim-Sermilik system and similar glacial fjords is the onset of atmosphere-driven surface melt and resulting runoff during summer. A complex hydrologic system routes most surface meltwater from supraglacial lakes and rivers to the ice sheet bed via cracks and moulins (Chu, 2014). As the meltwater flows through subglacial channels, it picks up sediments that have been physically eroded by the motion of the ice sheet above and drives further chemical weathering of the bedrock (Bhatia et al., 2013; Wadham et al., 2019). When it reaches the ice sheet margins, the surface meltwater is discharged into the ocean at the grounding line of Helheim Glacier, about 600 m below the surface at the head of Sermilik Fjord (Straneo et al., 2012; Straneo and Cenedese, 2015). This release of subglacial runoff (SGR) generates a turbulent buoyant plume, which rises toward the surface (or a subsurface neutral buoyancy depth), enhancing melt of the glacier terminus and driving significant upwelling of AW (Jenkins, 2011; Beaird et al., 2018). During the summer, the GMW layer generated by the SGR plume is warmer and richer in nutrients than the PW found at similar depths on the shelf, enhancing primary productivity and iceberg melt (Straneo et al., 2011; Cape et al., 2019; Moon et al., 2018). The two glacial inputs, SGR from surface melt and SMW from terminus and iceberg melt, together constitute about 10% of the summer GMW export, with upwelled AW forming close to 90% of the GMW volume (Beaird et al., 2018).

1.3.2 Nioghalvfjerdsbræ and -fjorden (79 North Glacier and Fjord): one of Greenland's last floating ice tongues

Less commonly, in cold water, a floating ice tongue may extend beyond the glacier grounding line, analogous to the wide ice shelves common around Antarctica (Figure 1.2b). Three large ice tongues remain around Greenland, with the largest at 79 North Glacier in the northeast. The processes of glacial modification inside the ice tongue cavity have a

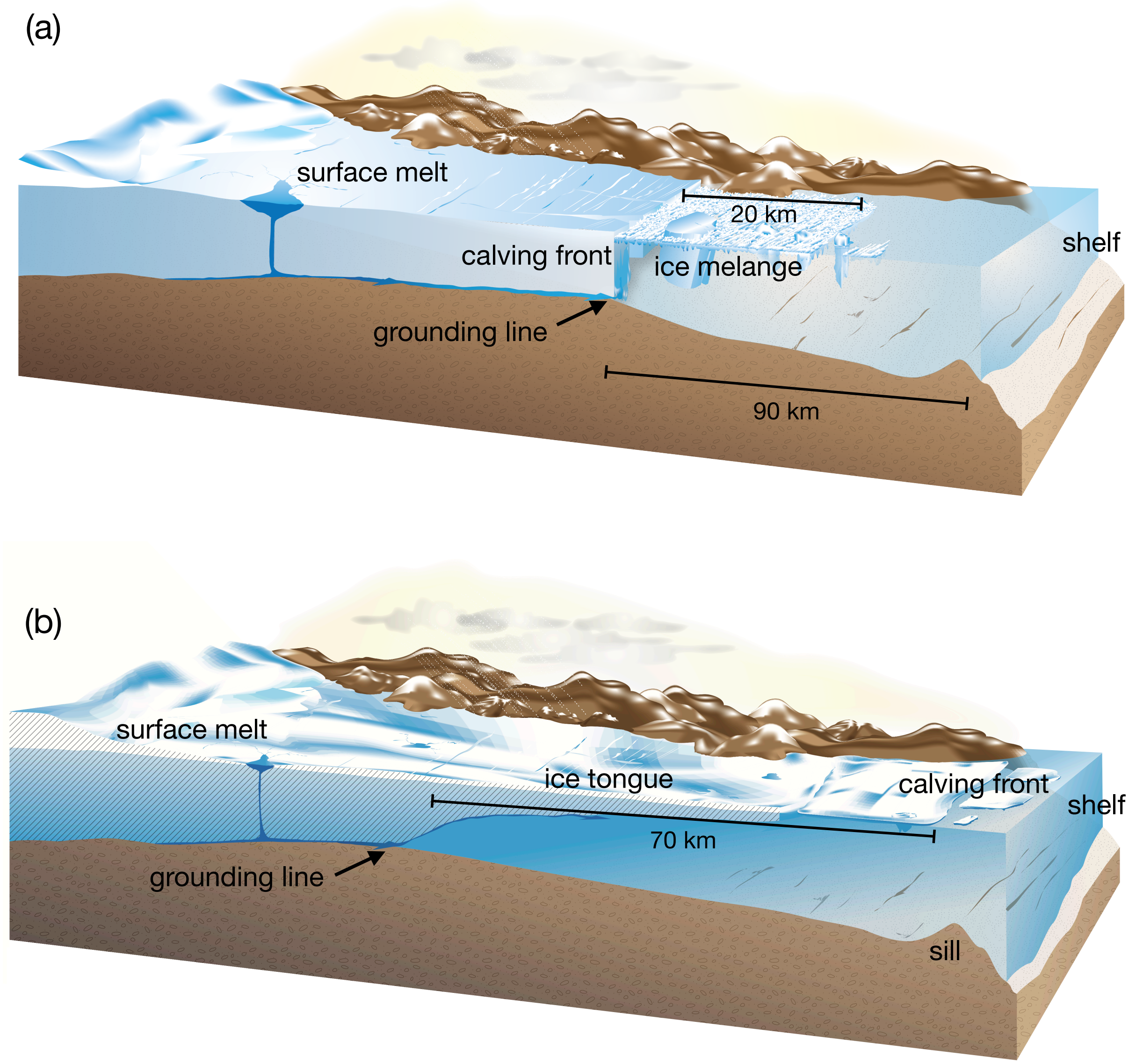

Figure 1.2. Fjord schematics for (a) a typical tidewater glacier system, with length scales corresponding to Sermilik Fjord, and (b) a floating ice tongue, corresponding to 79 North Fjord (not to scale).

different configuration than at a tidewater glacier. In the case of 79 North, where the ice tongue extends to the mouth of the fjord, submarine melt of the ice tongue base occurs along the length of the fjord, though melt rates are highest near the grounding line where the ice is thickest and thus subjected to the highest thermal driving (Wilson and Straneo, 2015; Wilson et al., 2017). Subglacial runoff plumes, similarly, remain in contact with the ice base, where they are steered by basal channels and Coriolis force (Millgate et al., 2013; Washam et al., 2019). Previous observations of ice tongue disintegration around Greenland suggest that their stability is largely determined both by the supply of ocean heat and by fjord geometry (Holland et al., 2008a; Mouginot et al., 2015).

1.4 Questions about Greenland's glacial fjords in the ice sheet–ocean system

As described above, substantial progress has been made over the past 15 years in understanding drivers of GrIS and ocean variability and the fjord processes that connect them, through a combination of observations, modeling, and theory. However, observations of certain locations and processes remain scarce. This thesis aims to build on this growing knowledge base by using the methods outlined in Chapter 2 to address some of the remaining gaps in our knowledge of Greenland fjords.

Chapter 3: Ocean circulation and variability beneath Nioghalvfjerdsbræ (79 North Glacier) ice tongue

Because ice tongues are comprised of glacier ice that is on the order of 100s of meters thick, accessing the ocean cavity underneath to make observations is challenging. Previous studies of 79 North Fjord thus relied primarily on a few individual temperature and salinity profiles, all of which were collected during summer, or on mooring records from the shelf outside the fjord. We use the first mooring record of temperature, salinity, and current velocity from within the 79 North ice tongue cavity to address the following questions:

- What are the dominant timescales and mechanisms of subannual variability in the 79 North ice tongue cavity?
- How do we expect observed ocean variability to affect ice tongue stability?

Chapter 4: Observational constraints on iceberg melt processes in Sermilik Fjord, southeast Greenland

Submarine melting of icebergs constitutes a significant fraction of the Sermilik Fjord heat and freshwater budgets. In contrast to terminus melt, iceberg melt is distributed along the fjord, which likely contributes to spatial variation in buoyancy-driven circulation. However, our knowledge of iceberg melt in fjords comes primarily from laboratory experiments and model simulations, which are largely unconstrained by ocean observations. We identify iceberg meltwater signatures in temperature and salinity profiles from a 2018 survey of a large iceberg in Sermilik Fjord and compare the observations to idealized simulations. The primary questions addressed in Chapter 4 are:

- How do ocean properties determine the distribution of iceberg meltwater in Sermilik Fjord?
- How well do existing parameterizations capture iceberg melt and upwelling rates?

Chapter 5: Physical controls on mercury distribution in Sermilik Fjord

A 2021 study found very high concentrations of toxic mercury in surface waters downstream of land-terminating glaciers in Southwest Greenland. Because there were very few other measurements of mercury around Greenland, it was unknown whether this finding was likely to extend to other regions, or how the distribution of glacier-sourced mercury would differ in a fjord with a marine-terminating glacier. We analyze mercury concentrations over the full water column of Sermilik Fjord from an August 2021 survey to answer:

- Is glacier meltwater a significant source of mercury to Sermilik Fjord?
- How do fjord processes determine the distribution and transport of mercury within this system?

1.4.1 Thesis outline

Each study presented in this thesis relies on the interpretation of oceanographic observations, primarily profiles of temperature and salinity, to identify signatures of ice melt. Chapter 2 provides a brief introduction to the temperature and salinity characteristics of subglacial runoff, submarine meltwater, the regional ocean water masses, and the typical resulting water mass mixtures within a glacial fjord. The melt parameterization and plume model applied in Chapters 3 and 4 are also presented.

In Chapter 3, we present a nine-month timeseries of ocean temperature, salinity, and velocity from a mooring beneath the 79 North ice tongue. A mean estuarine circulation is observed throughout the year with fluctuations inferred to be driven by variability on the shelf. Ocean warming observed on the continental shelf is advected into the fjord and reaches the glacier grounding line within 6 months, suggesting that basal melt and thus stability of the ice tongue is sensitive to regional ocean variability. We also show that the fjord overturning circulation is likely strengthened during summer by the release of surface runoff at the grounding line, as observed in other glacial fjords, seasonally enhancing ocean heat transport.

In Chapter 4, we use observations and melt plume simulations to characterize the upwelling and spatial distribution of meltwater around a large iceberg in Sermilik Fjord. Meltwater intrusions are identified in observations collected between 70-240 m away from the iceberg edge, both upstream and downstream of the iceberg. Melt plume height, calculated from the intrusion properties, is significantly higher below the pycnocline relative to the highly stratified upper water column, in agreement with theory, suggesting that upwelling of melt from large icebergs may enhance circulation in the deeper AW layer.

However, the simulations underestimate the observed melt concentration. We discuss the assumption of shear-controlled melt rate implicit in the model and suggest that it may not be valid in this relatively cold, low-shear environment.

Finally, in Chapter 5 we present results from an August 2021 field campaign indicating that glacially modified waters exported from Sermilik Fjord are significantly depleted in mercury relative to ocean waters on the shelf. This finding is contrasted to a recent study that found very high mercury concentrations in glacial melt in West Greenland. Our results suggest that it is unlikely that meltwater Helheim Glacier is a significant source of mercury to the fjord. Furthermore, we hypothesize that Sermilik Fjord is actually a net sink of oceanic mercury due to settling of sediments from subglacial runoff and iceberg melt, which could scavenge mercury from the water column.

Building on the existing understanding of glacial fjord dynamics, this thesis uses ocean observations, complemented by simple models and theory, to reach insights into drivers of fjord-scale variability, small-scale processes of iceberg melt, and relationships between ice-ocean interactions and biogeochemical cycles.

Chapter 2

Methods: identifying glacially modified waters in ocean observations

The primary tools used to identify glacially modified waters (GMW) in this thesis are measurements of ocean temperature and salinity, arguably the most traditional set of ocean observations. Submarine meltwater (SMW) and subglacial runoff (SGR) each have characteristic temperature and salinity signatures, so we can identify the fingerprints of glacial modification through comparison to measurements of upstream ocean properties on the shelf.

2.1 Temperature-salinity plots

Temperature-salinity (T-S) plots are commonly used in physical oceanography to show mixing between water masses. The representation of the two glacial endmembers in T-S space is introduced in the methods section of each chapter and we provide additional background here. Here the water masses are presented in the context of Sermilik Fjord, but the underlying processes are the same at 79 North, and the T-S characteristics and variability there are discussed in detail in Chapter 3.

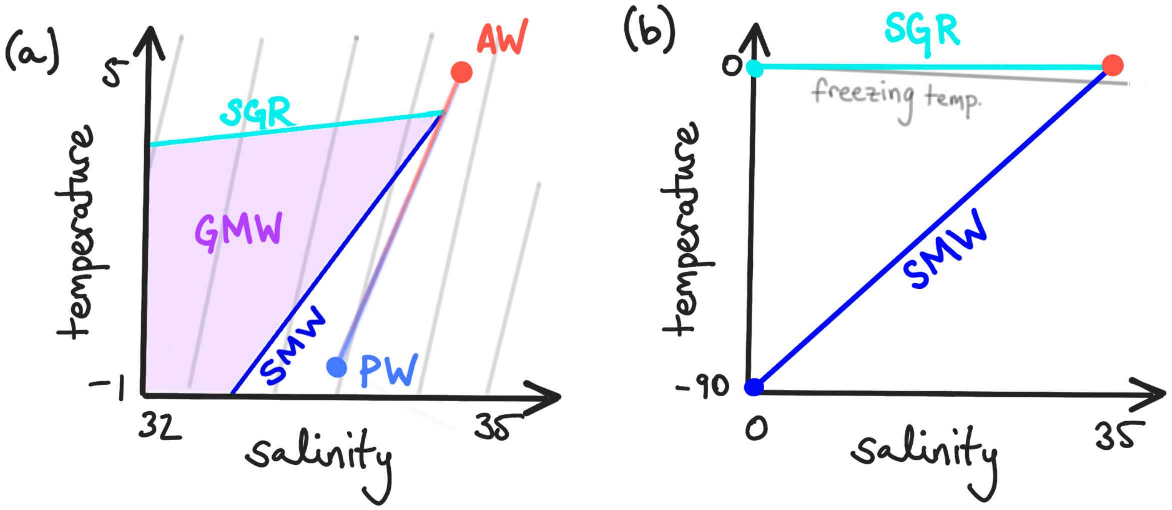

Figure 2.1. Temperature-salinity plot schematics. (a) The primary subsurface water masses on the shelf, AW (red) and PW (blue), are connected by a mixing line. The SGR (teal) and SMW (dark blue) mixing lines intersect the background T-S slope at properties corresponding to about 600 m depth in the fjord. During summer, fjord properties typically fall into the purple region labeled GMW, which comprises a mixture of shelf waters, SGR, and SMW. Isopycnal contours are in grey with density increasing from left to right. (b) The same T-S plot zoomed out to show the endmember values for SGR and SMW. The liquidus (freezing temperature as a function of salinity) is shown in grey.

2.1.1 Shelf water masses

The ocean on the Greenland continental shelf is salinity-stratified, and during summer, the T-S structure below 50 m is characterized by a mixing line connecting warm salty Atlantic Water (AW) to cold fresh Polar Water (PW; Figure 2.1a). The fjord inherits this basic structure in which temperature increases with depth over the subsurface water column.

2.1.2 Subglacial runoff

Runoff can simply be characterized as fresh water at the freezing point, i.e. temperature 0°C and salinity 0 g kg^{-1} (Figure 2.1b). For SGR, the mixing line intersects the ambient fjord properties at around 600 m, the depth at which it is released (Figure 2.1a). Because the salinity gradient is much larger than the temperature gradient in this setting, the primary effect of mixing with SGR is freshening. The slope of the runoff line is shallower than the AW-PW mixing line, so mixing of deep AW with fresh SGR drives upwelling of a mixture that is warmer than waters at the equivalent density on the shelf.

2.1.3 Submarine melt

Ocean-driven melting can also be represented by a mixing line with fresh water, but in contrast to runoff, the heat required to melt the ice is supplied by the ocean. This is taken into account through the definition of an "effective temperature" for SMW,

$$T_{\text{eff}} \equiv T_f - \frac{L}{c_w} - \frac{c_i}{c_w}(T_f - T_i), \tag{2.1}$$

where T_f is the freezing temperature (a function of salinity and pressure), L is the latent heat of fusion, c_w and c_i are the specific heat capacities of water and ice, and T_i is the ice temperature (Gade, 1979). The typical value of T_{eff} is about -87°C, so the primary effect of submarine melt is cooling (Figure 2.1b). The intersection of the melt mixing line and the liquidus, or freezing temperature line, limits the maximum concentration of SMW.

In this salinity-stratified setting, the freshening makes the mixture less dense than the source water (Figure 2.1a). As with the runoff line, when the background T-S slope is steeper than the SMW mixing slope, the upwelled melt mixture will be warmer than waters at the same density on the shelf. When the background T-S slope is shallower than the SMW slope, the mixture will instead appear as a cold anomaly. The AW-PW slope on the shelf is typically steeper than the SMW mixing slope, but the addition of SGR tends to shoal the fjord T-S slope such that during summer, SMW in the fjord typically manifests as a cold along-isopycnal anomaly.

Given that the SGR plume also drives enhanced submarine melt, GMW in Sermilik typically includes a mixture of both SGR and SMW. Thus the T-S properties tend to fall in the wedge formed by the two mixing lines, rather than along one or the other (Figure

2.1a). One small-scale exception to this is where intrusions of iceberg melt, which is not directly influenced by SGR, can be identified, as described in Chapter 4.

2.2 Other signatures of glacial modification

Glacier melt has other distinctive properties that may help to identify it in GMW mixtures. For example, Beaird et al. (2018) analyze noble gas compositions from water samples in Sermilik Fjord in order to quantify the fractions of each endmember in the exported GMW. While this process is too expensive and time-consuming to repeat regularly, many CTDs (Conductivity, Temperature, and Depth loggers) are equipped with additional sensors to measure parameters such as turbidity and dissolved oxygen. In Chapter 5, we explore the potential and limitations for these properties to be used as tracers of GMW and consider how they may be incorporated into the interpretation of water mass composition and GMW export.

2.3 Melt parameterizations and buoyant plume theory

To contextualize the results in Chapter 3, we use the sub-ice tongue timeseries as input to an established model of ice melt (Holland and Jenkins, 1999; Jenkins et al., 2010). The parameterized melt rate depends in part on velocity, which in this case comes from the mooring velocity timeseries, in order to estimate the effect of observed current variability on melt rate.

The three-equation melt formulation consists of conservation equations for heat and salt and a constraint that the ice-ocean boundary remain at the freezing point:

$$\dot{m}[c_i(T_b - T_i) + L = c_w C_D^{1/2} \Gamma_T u(T - T_b), \tag{2.2a}$$

$$\dot{m} S_b = C_D^{1/2} \Gamma_S u(S - S_b), \text{ and} \tag{2.2b}$$

$$T_b = \lambda_1 S_b + \lambda_2 + \lambda_3 (h - z), \tag{2.2c}$$

where $\dot{m}$ is melt rate; c_i and c_w are the heat capacities of ice and water; T_b and S_b are temperature and salinity of the ice-ocean boundary layer; T_i is the ice temperature; L is the latent heat of fusion; C_D is the drag coefficient; Γ_T and Γ_S are the turbulent transfer coefficients of heat and salt; and λ_n are empirical coefficients in the liquidus equation.

In the application to the mooring record in Chapter 3, T, S, and u are observed values of temperature, salinity and velocity. There, two of the empirical coefficients are combined into a thermal Stanton number, defined as $St_T \equiv C_D^{1/2} \Gamma_T$.

In cases where the relevant velocity and ambient properties are expected to be set by an upwelling melt plume in contact with the ice face, such as at the grounding line of 79 North in Chapter 3 or in the iceberg surveys in Chapter 4, the melt parameterization is coupled to a buoyant plume model (Jenkins, 2011; Slater et al., 2016). For a 1-dimensional line plume, the conservation equations for fluxes of volume, momentum, heat, and salt, respectively, are:

$$\frac{d}{dl}(bu) = \alpha u \cos\theta + \dot{m}, \tag{2.3a}$$

$$\frac{d}{dl}(bu^2) = b g_p' \cos\theta - C_D u^2, \tag{2.3b}$$

$$\frac{d}{dl}(buT) = \alpha u T_a + \dot{m} T_b - C_D^{1/2} u \Gamma_T (T - T_b), \text{ and} \tag{2.3c}$$

$$\frac{d}{dl}(buS) = \alpha u S_a + \dot{m} S_b - C_D^{1/2} u \Gamma_S (S - S_b), \tag{2.3d}$$

where l is distance along the ice face; θ is the angle of the ice face relative to the vertical;

α is the entrainment coefficient; g'_p is the reduced gravity of the plume; and T_a and S_a are ambient temperature and salinity. The plume has thickness b, and the other plume variables, velocity u, temperature T, and salinity S, replace the observed values in the melt parameterization Equations 2.2a-c.

For 79 North, the ice base slope θ is calculated from an estimated profile of ice tongue thickness, and u is an along-slope velocity (Figure 2.2b). For the simulations of iceberg melt in Chapter 4, we assume a vertical wall geometry such that $l = z$, $\cos\theta = 1$, and u is the vertical plume upwelling velocity w (Figure 2.2a). In both cases the plume model is initialized with a negligible freshwater input in order to simulate ambient melt plumes, in contrast to buoyant plumes initiated by a significant SGR flux.

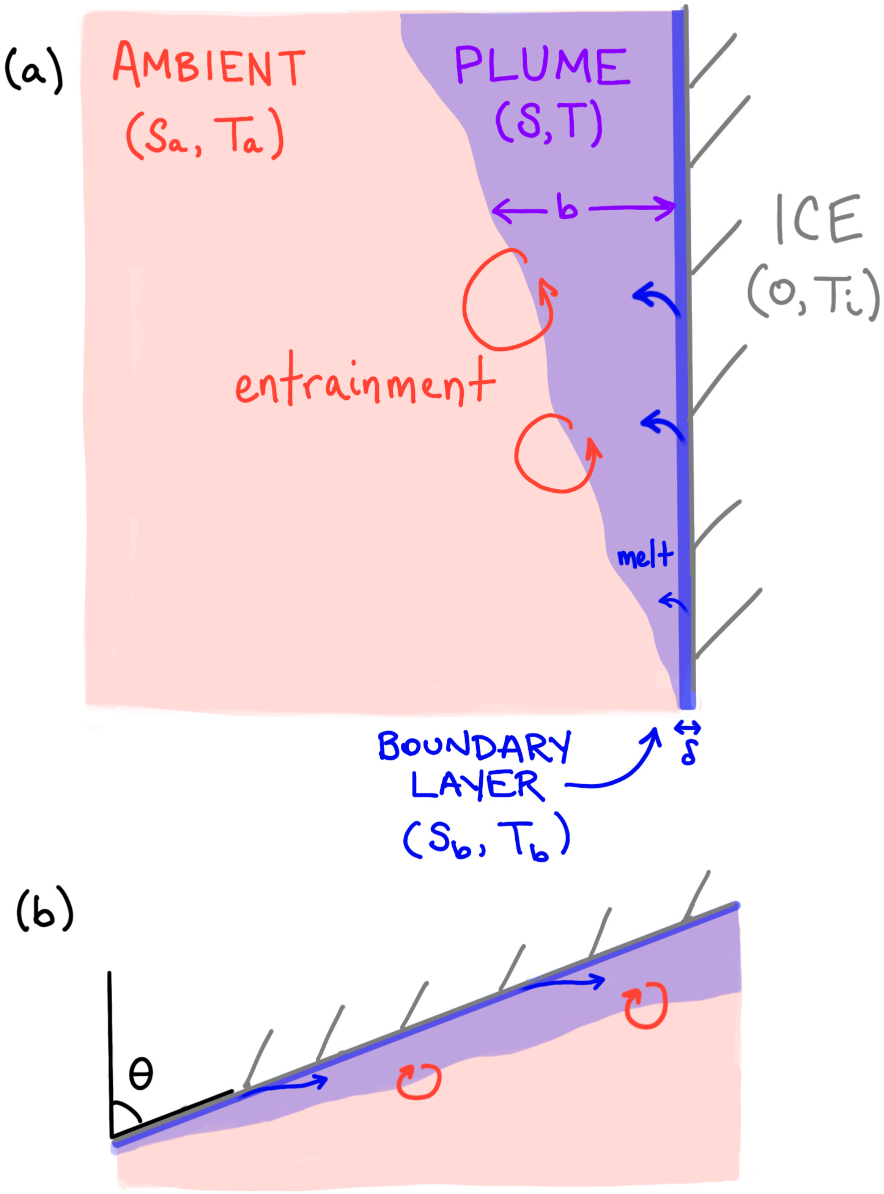

Figure 2.2. Plume schematics. (a) A melt plume at a vertical ice face with salinity S, temperature T, and thickness b (purple). The plume velocity is vertical. The ice-ocean boundary layer with salinity S_b, temperature T_b, and thickness δ (blue) separates the well-mixed plume from the ice, with temperature T_i (grey). The plume volume grows by melting of the ice face and entrainment of ambient waters with salinity S_a and temperature T_a. (b) Analogous schematic for a sloping ice base with angle θ from the vertical.

Chapter 3

Ocean circulation and variability beneath Nioghalvfjerdsbræ (79 North Glacier) ice tongue

3.1 Introduction

Ice tongues, floating extensions of glaciers, have historically been common features of many of Greenland's major outlet glaciers. However, several of these have broken apart over the past 20 years as ocean and air temperatures have warmed (Hill et al., 2018). Nioghalvfjerdsbræ (79 North Glacier: 79NG) terminates in a 70 km-long ice tongue, currently the largest in Greenland (Wilson et al., 2017), which is confined within Nioghalvfjerdsfjorden (79 North Fjord; Figure 3.1a). The 79NG ice tongue thinned by 30% between 1999 and 2014, but its extent has not decreased significantly (Mouginot et al., 2015). In contrast, the ice tongue of nearby Zachariæ Isstrøm (ZI) lost 95% of its area during the same period (Mouginot et al., 2015). The thinning of 79NG and collapse of ZI, the two major outlets of the Northeast Greenland Ice Stream (NEGIS), are thought to be driven by increased ocean melt driven by warming, as observed in the break-up of Sermeq Kujalleq ice tongue (also known as Jakobshavn Isbræ; Mouginot et al. (2015); Holland et al. (2008a); Motyka et al. (2011); Bjørk et al. (2015)). The loss of buttressing of upstream ice flow provided by the ZI and Sermeq Kujalleq ice tongues resulted in the retreat of their respective grounding lines along retrograde bed slopes and the acceleration of ice discharge (Mouginot et al., 2015; Joughin et al., 2014). The ocean's role in the evolution of 79NG ice tongue is therefore important to the future stability of NEGIS, which accounts for 12% of ice discharge from the Greenland Ice Sheet and holds a 1.1 m sea level equivalent (Dupont and Alley, 2005; Morlighem et al., 2014).

79NG Fjord is entirely covered by the ice tongue, and is connected to the continental shelf ocean via Dijmphna Sund to the north, and by several channels beneath the bathymetrically-pinned ice front to the east (Figure 3.1a; Mayer et al. (2000)). Previous studies of 79NG Fjord indicate that warm Atlantic Intermediate Water (AIW) present on the continental shelf flows into the ice tongue cavity through the eastern pinned front and drives significant melting of the ice tongue base, particularly in the vicinity of the grounding line (Wilson and Straneo, 2015; Wilson et al., 2017; Schaffer et al., 2017, 2020). The AIW is transformed through this process, becoming colder and fresher (and thus more buoyant) through the input of glacial meltwater. This glacial modification is thought to drive an estuarine-like circulation, with AIW flowing toward the grounding line at depth and shallow export of glacially-modified water through both branches of the fjord (Wilson and Straneo, 2015; Schaffer et al., 2020).

The warm AIW present on the continental shelf is sourced from Atlantic waters transported northward in the West Spitsbergen Current (WSC) toward Fram Strait, the primary gateway for heat, freshwater, and sea ice exchange between the Arctic Ocean and Nordic Seas (Marnela et al., 2013; de Steur et al., 2014). About half of WSC Atlantic water transport is recirculated in the 320 km-wide Fram Strait and returns southward in the East Greenland Current (EGC) (Marnela et al., 2013; de Steur et al., 2014; Hattermann et al., 2016). Schaffer et al. (2017) suggest that Atlantic waters in the EGC may be transported onto the 300 km-wide continental shelf via eddy- and tidally-driven mixing. AIW is thus created through mixing of Atlantic waters with colder Polar Water (PW) of Arctic origin present at shallow depths on the shelf. They estimate a 1.5 year timescale for ocean

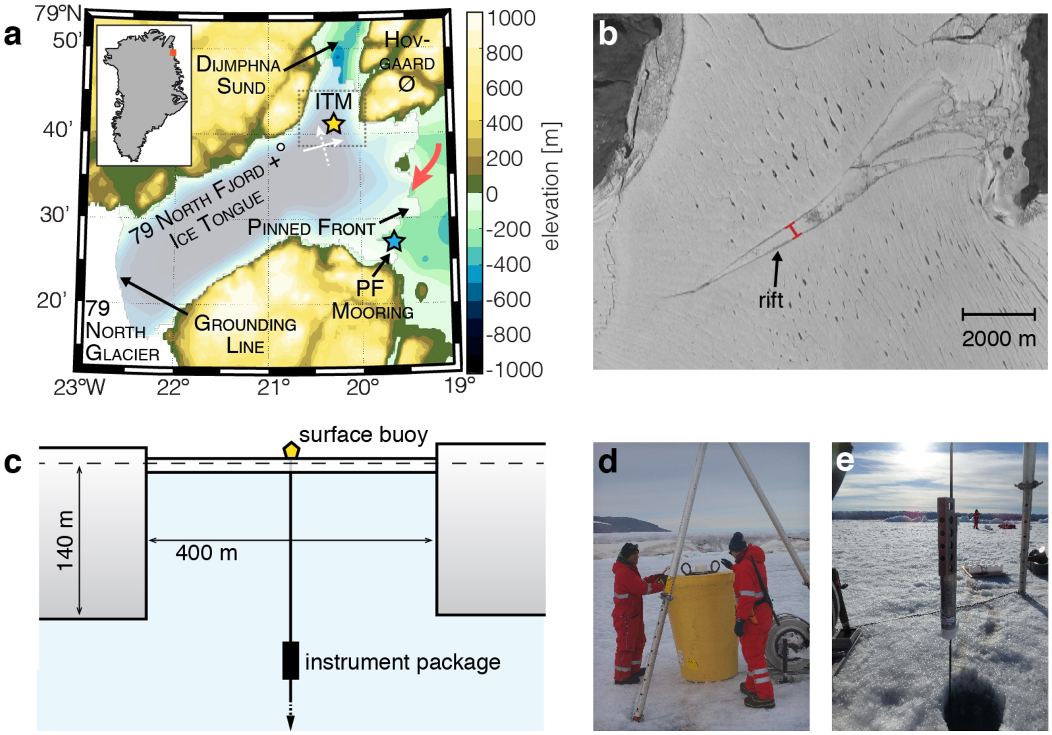

Figure 3.1. (a) Map of 79 North Fjord and ice tongue using BedMachine topography (Morlighem et al., 2017a,b), including locations of the Ice Tethered Mooring (ITM; yellow star) and Pinned Front mooring (PF; blue star). White arrows show the inferred along-fjord (solid) and cross-fjord (dashed) axes at the ITM site (see Section 3.3.2). The red arrow indicates the location of primary AIW inflow (Schaffer et al., 2020). The white circle indicates the location of the 1998 temperature profile shown in Figure 3.2a. Grey dotted box around ITM indicates location of satellite image in (b). Inset: Map of Greenland coastline with orange box indicating the location of 79 North Glacier and Fjord. (b) Satellite image of ice tongue rift (July 2013; image from Google & Maxar Technologies). The red line spanning the rift is 400 m long and indicates the approximate ITM location. (c) Schematic of ITM configuration (not to scale). The surface buoy sits on sea ice that formed where the ice tongue rifted apart. The draft of the ice tongue on either side of the rift is approximately 140 m, so the 150 m instrument is 10 m below the ice base. (d) ITM surface buoy at time of deployment. (e) Deployment of an ITM MicroCAT.

property anomalies in the WSC to be advected to the 79NG terminus. The temperature of northbound Atlantic waters in the WSC increased by 0.06°C year^{-1} from 1997-2010, which has likely affected AIW properties on the shelf, but with a smaller magnitude due to modification by mixing (Beszczynska-Möller et al., 2012; Schaffer et al., 2017). Warming of deep AIW within 79NG cavity is inferred from three ocean temperature profiles in summers 1998, 2009, and 2014 (Figure 3.2a; Wilson and Straneo (2015); Mayer et al. (2018)), but it is unknown whether these observations accurately reflect a significant trend, or are biased by subannual or interannual variability. Sustained warming of AIW reaching the 79NG ice tongue base would cause an increase in basal melt rate, but more measurements are needed to characterize the relationship between offshore ocean property changes, changes on the continental shelf, and their propagation into the 79NG cavity.

In addition to far-field ocean warming, atmospheric warming beginning around 2000 may have had significant impacts on variability in the 79NG cavity (Khan et al., 2014). Both air and ocean warming likely contributed to the break-up of the Norske Øer Ice Barrier (NØIB), a region of landfast sea ice on the continental shelf adjacent to 79NG and ZI, which was formerly quasipermanent but has broken up nearly every summer since 2001 (Sneed and Hamilton, 2016). In addition to the role of sea ice in modulating air-ocean exchanges, landfast sea ice can provide backstress on floating glacier fronts (Reeh et al., 2001), and the loss of the NØIB may have contributed to the destabilization of the ZI ice tongue (Khan et al., 2014). Furthermore, the northeastern sector of the Greenland Ice Sheet, which is drained primarily through 79NG and ZI, has seen a dramatic decrease in its surface mass balance since 2000, resulting in increasing runoff of ice melt (Mouginot et al., 2019; MacFerrin et al., 2019). A fraction of the ice sheet surface melt drains to the bed through cracks in the ice and is routed to the margins through subglacial channels, entering the ocean at glacier grounding lines, where it drives enhanced basal melt by increasing turbulent heat transfer to the ice base as it rises buoyantly (Chu, 2014; Straneo and Cenedese, 2015; Jenkins, 2011). At 79NG, additional surface melt is likely exported

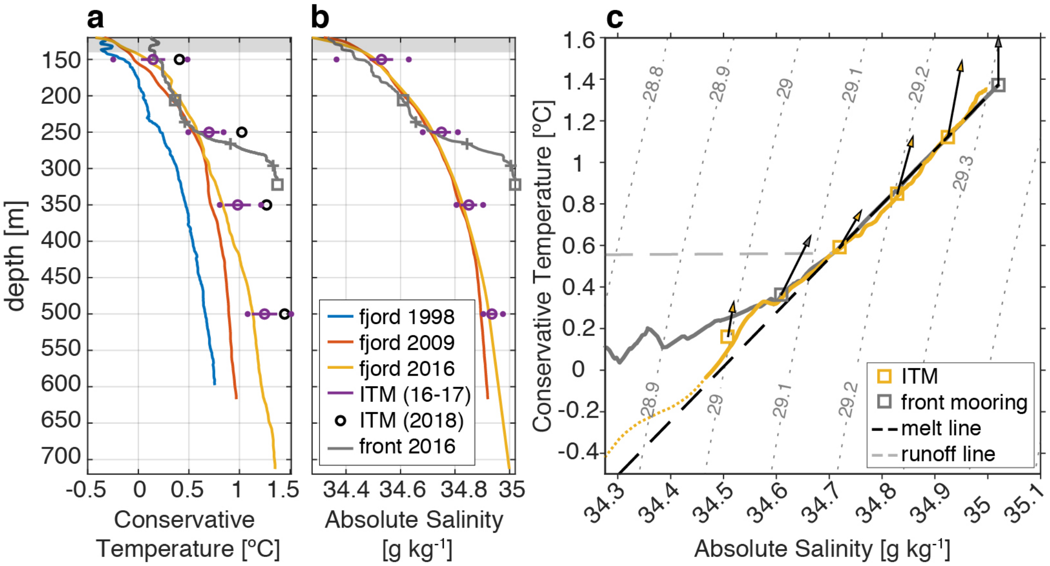

Figure 3.2. (a) Conservative Temperature and (b) Absolute Salinity profiles in the 79NG cavity from 1998 (blue; Schaffer and Mayer (2018)), 2009 (blue; Straneo (2020)), and 2016 (yellow). The location of the 1998 profile is shown in Figure 3.1a; the 2009 and 2016 profiles are from the ice tongue rift. The 2016 salinity profile above 150 m is from the XCTD (dotted line); between 150 m and 500 m (solid line) it is interpolated from ITM salinity observations (see Section 3.2). The time mean of the 2016-2017 time series of temperature and salinity at each ITM depth is plotted as an open circle (purple). One standard deviation is indicated by the purple line, with the record minimum and maximum indicated by purple dots. The average temperature at each depth during early summer 2018 is plotted as a black circle (see Section 3.2). August 2016 Conservative Temperature and Absolute Salinity profiles from the Pinned Front (PF) mooring location are plotted as grey lines, with squares indicating the depths of moored CTDs and crosses indicating the depths of moored thermistors. Shading above 140 m indicates the approximate ice tongue draft near the ITM location. (c) Conservative Temperature and Absolute Salinity from the August 2016 profiles at the ITM (yellow) and PF (grey) locations in August 2016. The squares indicate the mean temperature and salinity observed by each Microcat over the first 24 hours of the mooring records. The dashed lines indicate the mixing lines associated with basal melt (black) and subglacial runoff (light grey). The arrows indicate the change in temperature and salinity properties at each moored instrument through the end of each mooring record (July 2017 at the ITM, September 2017 at PF).

through supraglacial rivers and enters the surface ocean at the ice tongue terminus, as has been observed at e.g. Petermann Gletscher in northern Greenland (Johnson et al., 2011) and Nansen Ice Shelf in Antarctica (Bell et al., 2017).

The sensitivity of ice tongue melt to external ocean variability depends on its timing and magnitude as well as the timescales and mechanisms of exchange between the cavity and shelf (e.g. Holland (2017)). A melt-driven overturning circulation alone would drive a relatively slow exchange with the shelf (Wilson and Straneo, 2015), but recent studies indicate that AIW inflow into the 79NG cavity is hydraulically controlled by a sill outside the pinned front (Schaffer et al., 2020; Zhao et al., 2019) and may be modulated by remotely-forced topographic Rossby waves (Münchow et al., 2020). Studies of other Greenland fjords have shown that exchange is enhanced by energetic shelf-driven flows and discharge of summer surface melt at the grounding line, both of which can accelerate renewal of fjord waters (Washam et al., 2018; Straneo et al., 2010; Jackson et al., 2014). Tidal currents and eddies have also been found to significantly enhance basal melt of Antarctic ice shelves (Arzeno et al., 2014; Hattermann et al., 2012; Padman et al., 2018). Previous observations in the ice tongue cavity do not include ocean currents and provide snapshots only of summer conditions, so the key processes driving variability in the 79NG cavity properties and circulation, and by extension ice tongue melt, are unknown.

In this paper, we present the first moored record of temperature, salinity, and currents in the 79NG ice tongue cavity. We analyze variability of water masses and circulation in the cavity over the nine-month record, which spans from August 2016 to July 2017, compare this with time series of ocean- and glacier-driven variability to identify possible mechanisms, and discuss the implications for basal melting of the ice tongue. Our results suggest that external ocean forcing and glacier-driven processes both drive significant variability in ocean properties and circulation and thus ice tongue melt.

3.2 Data

An Ice Tethered Mooring (ITM) was deployed in the 79NG ice tongue rift near Hovgaard Ø during the PS100 expedition of the RV *Polarstern* in August 2016 (Figure 3.1a,d-e; Toole et al. (2016); AWI (2017)). The rift forms where the ice tongue splits into two branches, exposing the ocean surface and allowing sea ice to form, and is approximately 400 m wide in the vicinity of the ITM (Figure 3.1b). The sea ice thickness is on the order of meters, while the glacial ice draft in this area is approximately 140 m (Wilson et al., 2017), and the bottom depth is approximately 720 m (Figure 3.1c; Wilson and Straneo (2015)). The ITM location is approximately 13 km north and 18 km west of the primary AIW inflow location (Figure 3.1a; Schaffer et al. (2020)). The inductive mooring had Sea-Bird Electronics SBE37 MicroCAT Conductivity, Temperature, and Depth (CTD) instruments and Nortek Aquadopp current meters at 150 m, 250 m, 350 m, and 500 m, recording observations every 15 minutes. Two temperature and salinity profiles were also collected using Lockheed Martin XCTD-1s (eXpendable CTDs) at the time of deployment (Straneo and Wilson, 2020). All timeseries were low-pass filtered with a fourth order 33-hour Butterworth filter, and temperature and salinity measurements are reported as Conservative Temperature and Absolute Salinity (McDougall and Barker, 2011), unless otherwise specified. Uncertainties for each sensor are listed in Table 3.1. The ITM surface buoy transmitted real-time data and GPS locations every 24 hours through July 2017, excluding a two-month gap beginning in late winter, for a total of nearly nine months of data. During this time, the buoy position moved 450 m to the northeast, indicating a mean local ice flow speed of 1.3 m day^{-1}.

We assume that the ocean properties and circulation observed by the ITM below the ice shelf rift are representative of conditions at similar depths under the ice shelf base nearby. This assumption is particularly uncertain at 150 m, where ocean conditions are most likely to be affected by their proximity to the rift. Simulations by Jordan et al.

Table 3.1. Sensor uncertainties according to manufacturer specifications.

Sensor	Temperature [°C]		Salinity [g kg^{-1}]		Velocity [cm s^{-1}]
	Accuracy	*Resolution*	*Accuracy*	*Resolution*	*Accuracy*
MicroCAT	0.002	0.0001	0.004	0.0001	—
Aquadopp	0.01	0.01	—	—	0.5–0.6[a]
XCTD	0.02	0.01	0.04	0.02	—

[a] For observed velocity range.

(2014) suggest that an ice shelf rift affects the ocean below it most strongly when upstream ocean temperatures are close to freezing and currents are strong. In contrast, we find that temperatures at the ITM at 150 m are consistently well above freezing (Section 3.3.5), currents are relatively weak (Section 3.3.2), and stratification in the rift is stable (Figure 3.2b), limiting the potential for vertical mixing. While some influence from the rift cannot be ruled out, these factors support our interpretation of ITM observations as representative of cavity properties beneath the proximal ice base.

The pressure recorded by all ITM CTDs indicated shoaling of 14 m over the course of the record. This change occurred in several distinct events throughout the record that were observed simultaneously over all depths, suggesting that the wire rope at the surface buoy end was trapped in sea ice and lifted, likely by mechanical ice ridging. Because temperature increases with depth in this setting, this upward displacement of the sensors would be expected to move them into water that is colder and fresher (Figure 3.2a-b). At the time of the 2016 XCTD profile, shoaling of 14 m would be associated with cooling of 0.20°C at 150 m, 0.04°C at 250 m and 350 m, and 0.02°C at 500 m. At all depths, the temperature and salinity change induced by shoaling is much smaller in magnitude than the observed temperature variability (Section 3.3.1), but the reported warming is likely underestimated as a result of the shoaling.

The sea ice ridging is also a likely driver of the gaps in the mooring record, as it could have caused the ground lead to lose contact with the seawater, resulting in a loss of electrical continuity in the inductive modem loop. When the MicroCAT data ceased transmission in February and July 2017, the Aquadopp current meters, which also have temperature recorders, continued to transmit data for a few days longer. Data transmission from the Aquadopps also resumed for between four days (350 m) and two weeks (150 m) in June-July 2018. At each depth, a constant offset between the Aquadopp and MicroCAT temperature sensors was calculated from the overlapping parts of the timeseries and used to correct the Aquadopp sensor temperatures, which have a lower accuracy and resolution (Table 3.1). The 2018 Conservative Temperature values shown in Figure 3.2a are calculated using the mean temperature from this period and the mean salinity from the 2016-2017 record at each depth.

We compare the variability observed by the ITM within the cavity with a mooring record on the continental shelf outside the pinned ice front (Pinned Front mooring; PF), south of the presumed AIW inflow pathway (Figure 3.1a; Schaffer et al. (2019)). Its location is approximately 35 km southeast of the ITM and has a bottom depth of 322 m. This mooring was also deployed by the Alfred-Wegener Institute during the PS100 expedition in August 2016 and recovered in September 2017. The mooring was instrumented with temperature loggers at five depths between 206 m and 322 m, with conductivity measurements at the shallowest and deepest instruments. For the instruments with no conductivity sensors, Conservative Temperature was calculated using the Absolute Salinity at the corresponding depth from the CTD profile at the time of deployment (Figure 3.2b; grey crosses). An upward-looking 150 kHz ACDP (TRDI Workhorse Quartermaster) measured velocity at 4 m vertical resolution between 38 m and 314 m. Like the ITM timeseries, all PF timeseries were low-pass filtered with a fourth order 33-hour Butterworth filter. Mayer et al. (2000) found that the ice tongue draft at the terminus near PF was approximately 100 m, though the southern portion of the terminus has retreated by about 10 km due to calving since that survey (Khan et al., 2014).

Ice sheet surface melt calculated by the Regional Atmospheric Climate Model (RACMO; Noël et al. (2018)) over the 79NG Glacier catchment area defined by Slater et al. (2019) is used to estimate subglacial runoff, i.e. surface melt that is discharged to the ocean through subglacial channels at the grounding line. The total volume of surface melt is an upper bound on subglacial runoff, because we expect that some of the melt is exported by supraglacial rivers or stored (e.g. in melt ponds on the ice tongue surface; Figure 3.1b). However, the 2017 annual mean subglacial runoff transport estimated from RACMO (0.11 mSv) agrees within uncertainty with the observationally-derived estimate from Schaffer et al. (2020), and we expect the seasonal cycle of subglacial runoff to be very similar to that of total surface melt.

3.3 Results

3.3.1 Water masses in the 79NG cavity

The vertical structure of water masses at the time of ITM deployment in August 2016 is consistent with previous observations, with relatively cold fresh water overlying warmer saline AIW present at depth (Figure 3.2a-b). Temperature increases over the full water column depth, so our mooring record from 500 m likely does not capture the maximum temperatures present in the cavity. At 250 m and below, the temperature-salinity (T-S) properties in the initial profile fall approximately along a melt line relative to the deep AIW properties (Figure 3.2c). The melt line, or Gade slope, represents the expected temperature and salinity of glacially-modified water formed when the heat for ice melt is supplied from a single endmember water mass (in this case, AIW) (Gade, 1979). The T-S property distribution suggests that the cavity is filled mainly with a mixture of AIW and ice tongue basal melt. (We note that the mixing line slope between AIW and cold, fresh PW present on the continental shelf is similar to the melt line slope. We provide additional evidence to support the interpretation that this is glacially-modified water in Section 3.3.2.) Mixing with subglacial runoff, which is assumed to enter the ocean at the local freezing temperature with salinity 0 g kg^{-1}, is represented by the runoff line.

At 150 m, T-S properties initially fall between the melt line and the runoff line, indicating that there is runoff in the upper water column (Figure 3.2c). Waters in August 2016 are consistently warmer relative to the 1998 and 2009 observations over the observed water column (Figure 3.2a-b). (The melt and runoff lines are described further in Section 2.1.)

Comparison with the initial properties at the PF site indicates the presence of similar water masses inside the cavity and outside the calving front, with a maximum temperature of 1.35°C at the ITM (713 m) and 1.37°C at PF (314 m; Figure 3.2a). T-S properties at PF fall along the melt line below 245 m, and between the melt and runoff lines between that depth and the shallowest mooring instrument at 206 m, suggesting that the ocean properties recorded by the mooring initially contain glacially-modified waters, including subglacial runoff, from the cavity (Figure 3.2c). Distinguishing between glacially-modified waters and PW is particularly challenging on the shelf, but the overlap of properties at the PF site below 200 m with properties in the cavity on the T-S diagram suggests that there is not significant PW at these depths, in agreement with past observations (Wilson and Straneo, 2015).

Over the course of the ITM record, AIW temperature and salinity observed at 500 m increase from 1.12°C to 1.49°C and from 34.92 to 34.95 g kg^{-1}, respectively (Figure 3.3a-b). Smaller increases are observed at the shallower depths. Increasing temperature and salinity are first observed at 150 m and 250 m in late November 2016, and at 350 m and 500 m beginning in December 2016. Mean and variability in properties at each depth for the time periods indicated by the colored lines above Figure 3.3a-b are listed in Table 3.2.

The timeseries of PF temperature and salinity (Figure 3.4a-b) are broadly similar to the ITM timeseries. Variability in PF temperature and salinity are relatively small from August to late November 2016, except at 266 m, where temperature ranges from 0.65°C to 1.21°C. This is likely because it is initially located in a strong thermocline (Figure 3.2a), making temperatures near that depth particularly sensitive even to small isopycnal

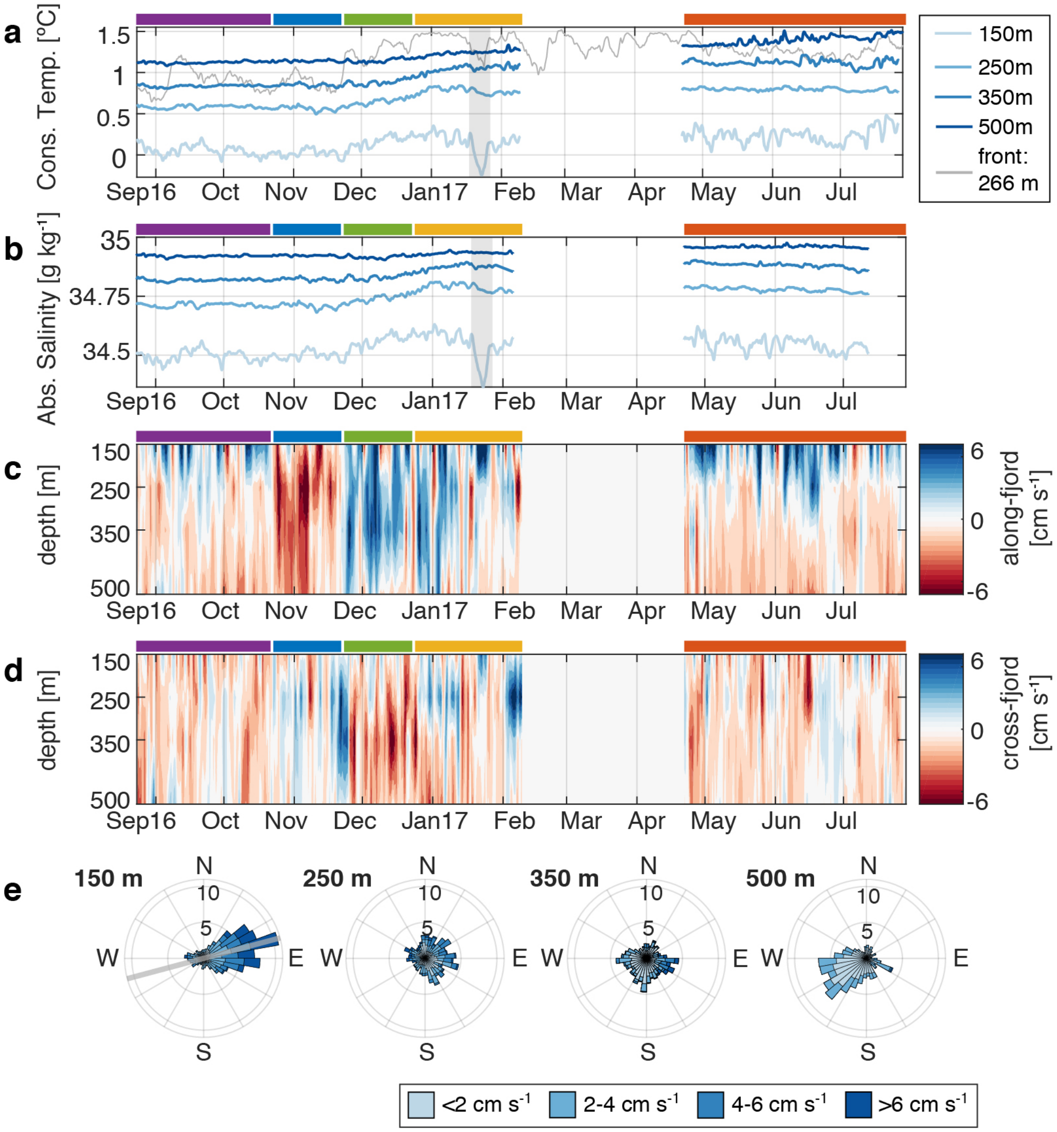

Figure 3.3. Low-pass filtered ITM data from the 79NG ice tongue cavity. (a) Timeseries of Conservative Temperature at the ITM (each depth, blues) and PF (266 m, grey). (b) Timeseries of Absolute Salinity at the ITM (each depth, blues). Shaded regions in (a-b) indicate the cold pulse discussed in Section 3.3.3. (c) Along-fjord velocity at the ITM (rotated onto 150m major axis of variability; see grey line in (e)). Positive velocities (blue) are directed toward the pinned front. (d) Cross-fjord velocity at the ITM (150m minor axis). This direction corresponds approximately to flow toward and away from Dijmphna Sund, with positive velocities (blue) toward Dijmphna Sund. Velocities in (c-d) are vertically interpolated with the current meter depths indicated by tick marks on the y-axis. Colored lines above (a-d) indicate the duration of each time period shown in Figure 3.5. (e) Velocity roses (not rotated) showing time-percentage of current directions at each depth. Shading indicates current speed. The light grey line on the 150m rose indicates the major axis of variability, i.e. inferred along-fjord direction.

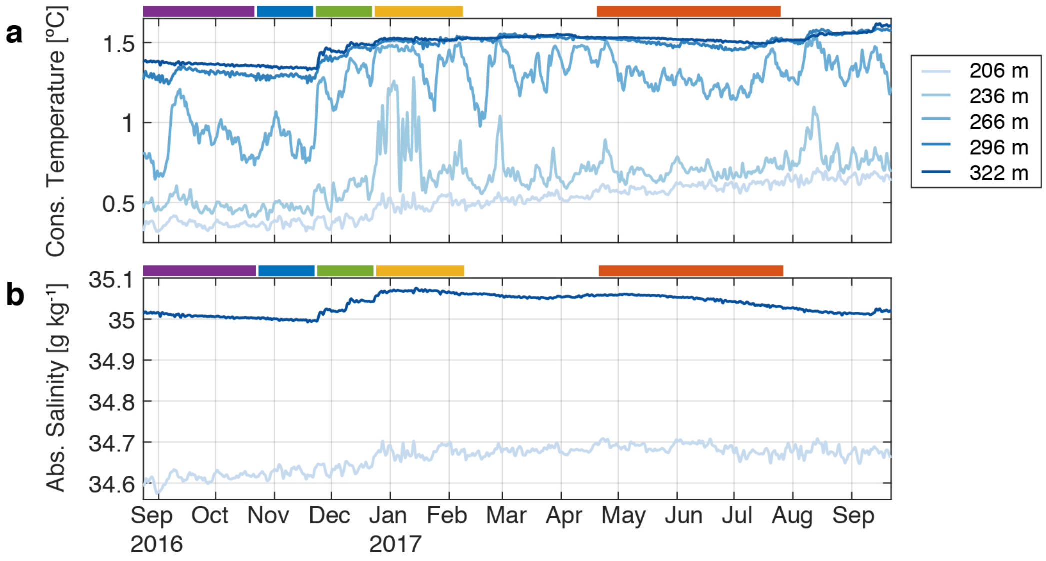

Figure 3.4. Low-pass filtered timeseries of (a) Conservative Temperature and (b) Absolute Salinity at PF (each depth, blues). The colored lines correspond to those in Figure 3.3a-d for comparison to the ITM timeseries.

displacements. At 322 m, which likely reflects AIW properties, temperature increases from 1.38°C in August 2016 to 1.52°C in July 2017, warming further to 1.61°C through September 2017 (Figure 3.4a). Connections between the ocean property variability at the ITM and PF locations and their interactions with the circulation are discussed in depth in Section 3.3.3.

3.3.2 Cavity circulation and exchange with continental shelf

Time-mean and standard deviation of current speeds observed at the ITM ranged from 4.2 ± 2.5 cm s^{-1} at 150 m to 2.3 ± 1.3 cm s^{-1} at 500 m. Tidal currents were estimated using T_Tide harmonic analysis (Pawlowicz et al., 2002). Tides appear to be primarily barotropic. The largest reconstructed tidal velocity was the M2 semidiurnal lunar tide, with magnitude 1.4 ± 0.1 cm s^{-1} at all depths. No other semidiurnal or diurnal tidal constituents were associated with velocities greater than 0.5 cm s^{-1}. Tidal currents account for as little as 7.4% of velocity variance at 150 m and up to 26.5% of variance

Table 3.2. Variability in Conservative Temperature (CT) & Absolute Salinity (AS) observed by ice-tethered mooring in 79 North ice tongue rift, August 2016 - July 2017.

Depth	Time period[a]	CT Mean[b] [°C]	CT Trend[c] [°C month^{-1}]	AS Mean [g kg^{-1}]	AS Trend [g kg^{-1} month^{-1}]
150 m	Full record	0.15 ± 0.12	0.02 ± 0.01	34.53 ± 0.04	—
	Aug-Oct	0.05 ± 0.06	—	34.50 ± 0.02	—
	Oct-Nov	0.03 ± 0.04	—	34.50 ± 0.02	—
	Nov-Dec	0.13 ± 0.09	—	34.55 ± 0.04	—
	Dec-Feb	0.16 ± 0.12	—	34.55 ± 0.06	—
	Apr-Jul	0.22 ± 0.07	—	34.55 ± 0.03	—
250 m	Full record	0.70 ± 0.10	0.02 ± 0.01	34.75 ± 0.03	—
	Aug-Oct	0.58 ± 0.02	—	34.71 ± 0.01	—
	Oct-Nov	0.56 ± 0.03	—	34.71 ± 0.01	—
	Nov-Dec	0.63 ± 0.04	0.22 ± 0.08	34.74 ± 0.01	0.20 ± 0.08
	Dec-Feb	0.77 ± 0.04	—	34.79 ± 0.02	—
	Apr-Jul	0.80 ± 0.02	—	34.78 ± 0.01	-0.01 ± 0.00
350 m	Full record	0.98 ± 0.13	0.04 ± 0.01	34.85 ± 0.03	0.01 ± 0.00
	Aug-Oct	0.84 ± 0.01	—	34.82 ± 0.00	—
	Oct-Nov	0.85 ± 0.02	—	34.82 ± 0.01	—
	Nov-Dec	0.87 ± 0.03	—	34.83 ± 0.01	—
	Dec-Feb	1.04 ± 0.05	0.07 ± 0.05	34.87 ± 0.01	0.07 ± 0.05
	Apr-Jul	1.12 ± 0.03	—	34.88 ± 0.01	—
500 m	Full record	1.25 ± 0.12	0.03 ± 0.00	34.94 ± 0.02	—
	Aug-Oct	1.12 ± 0.01	—	34.92 ± 0.00	—
	Oct-Nov	1.14 ± 0.01	—	34.92 ± 0.00	—
	Nov-Dec	1.14 ± 0.02	—	34.92 ± 0.01	—
	Dec-Feb	1.23 ± 0.04	0.06 ± 0.03	34.93 ± 0.01	0.07 ± 0.02
	Apr-Jul	1.38 ± 0.05	0.04 ± 0.02	34.96 ± 0.00	0.04 ± 0.02

[a] Time periods refer to date ranges indicated in Figure 3a-b.

[b] Range given is one standard deviation.

[c] Trends listed if significant at the 95% confidence level.

at 500 m. Velocities were low-pass filtered (see Section 3.2) for analysis of the subtidal circulation.

At 150 m, the major axis of current variability is oriented toward 15°N, and explains 68.8% of the total velocity variance at that depth (Figure 3.3e). This direction corresponds to along-fjord velocities in the main branch of the fjord, i.e. toward the pinned front to the east (Figure 3.1a; solid white arrow). Velocities at all depths are rotated onto this axis for analysis of the along- and cross-fjord circulation (Figure 3.3c-d).

Time-mean along-fjord velocities are consistent with a weak overturning circulation, with mean outflow of 2.1 ± 0.3 cm s^{-1} at 150 m ($p<0.001$) and inflow of 0.4 ± 0.2 cm s^{-1} at 500 m ($p=0.02$) (Figure 3.5a; see 3A for calculation of standard error of the mean). This mean flow is qualitatively consistent with the circulation pattern inferred from hydrography, indicating inflowing AIW from the continental shelf at depth and shallow export of glacially modified water (e.g. Wilson and Straneo (2015)). However, the main fjord width ranges from 20 km at the grounding line to 30 km at the mouth, which is 5-10 times wider than the internal deformation radius of 3-4 km (computed from the August 2016 buoyancy frequency profile; Chelton et al. (1998)), and the main inflow is localized within a 2 km wide channel near the center of the pinned front (Figure 3.1a; Schaffer et al. (2020)). Thus it is likely that significant variations in current amplitude and direction exist across the fjord. Furthermore, bathymetry, which is poorly known beneath the ice tongue (Mayer et al., 2000), likely plays a role in steering the flow. The current meters measure only at discrete depths, and the deepest instrument is above the densest AIW and approximately 200 m above the seafloor (720 m; Figure 3.2a-b), so it is likely that our observations do not capture the strongest inflow.

Two distinct modes of circulation are observed in the along-fjord velocities. During the first two months of the record, the time-mean circulation closely reflects the mean overturning pattern of the full record (Figure 3.5b). A second, more barotropic mode is observed from late October to late December 2016 with inflow at all depths in late

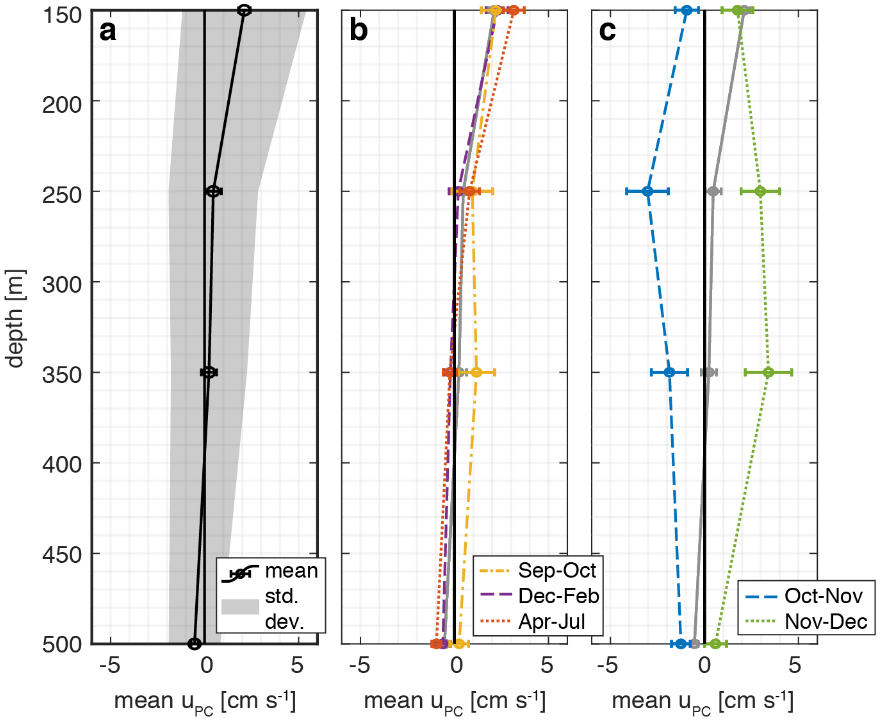

Figure 3.5. Time-mean along-fjord velocity at each ITM depth for (a) the full timeseries and (b-c) the time periods indicated by the colored bars in Figure 3.3. Positive (negative) velocities correspond to inferred outflow (inflow) direction. Error bars indicate the standard error of the mean (see 3A). The shaded range indicates the standard deviation. Time periods in (b-c) were selected to highlight transitions between the circulation modes discussed in Section 3.3.2 and range in length from 1 to 3.5 months. The full record mean and standard error is plotted in grey (solid line) on each panel for comparison.

fall (late October through late November) and outflow from the cavity in early winter (late November through late December, Figure 3.5c). During these times, the strongest observed velocities are at the mid-depth instruments, 250 m and 350 m. In mid winter (late December through February), there is outflow at 150 m and 350 m, with means not significantly different from zero at the other depths (Figure 3.5b). Following the gap in the record in late winter and early spring, the final 3.5 months of the timeseries show a slightly enhanced overturning with inflow at 500 m, and outflow at both shallower instruments (Figure 3.5b).

Variability in current direction is large at 250 m and 350 m (Figure 3.3e), and mean along- and cross-fjord velocities over the full timeseries are not significantly different from zero at either depth (Figure 3.5a). The mid-depth currents have intervals (days to weeks) of significant flow in all directions, including predominantly southward (negative cross-fjord) flow during August (250 m and 350 m) and September (350 m) and northward (positive cross-fjord) flow during mid November (both), mid December, and mid-late January (250 m) (Figure 3.3d). These time periods alternate with periods of flow in the along-fjord direction, suggesting that there may be intermittent exchange with Dijmphna Sund at these depths.

Assuming that the along-fjord velocity component is representative of the exchange flow through the eastern pinned front with inflow at 500 m and outflow at 150 m, we estimate a timescale for cavity renewal. Based on the mean velocity profile (Figure 3.5a), we assume that there is a middle layer of no net flow extending at least from 250 m to 350 m depth. We also impose a balance between inflow and outflow such that there is no net transport. The possible inflow and outflow layer thicknesses are thus constrained by this balance, in addition to the physical boundaries of the ice base, “stagnant” middle layer, and seafloor. We approximate that the outflow observed at 150 m represents the average over an upper layer with thickness between 50 and 75 m, and the inflow observed at 500 m represents the average over a layer with thickness 200 to 275 m. Under these simplified assumptions and given these ranges of layer thickness, the estimated cavity residence time calculated from the mean overturning velocities is between 255 and 380 days. Repeating the calculation for the time-mean velocities from April to July, when the overturning is slightly strengthened (Figure 3.5b), reduces the estimated exchange timescale to between 175 and 265 days. These estimates, based on the first direct observations of cavity currents, are consistent with a previously published estimate of 110 to 320 days based on a cavity heat budget assuming a steady state balance between heat advection and melting (Wilson and Straneo, 2015). A more recent estimate based on volume transport estimates from moored current meters at the cavity gateways gave an average residence time of 162 days, below the range calculated here (Schaffer et al., 2020). This suggests that the ITM observations may not reflect the full overturning strength, either due to the location or the low vertical resolution of the current meters.

3.3.3 Characteristics and timing of 2016-2017 ocean property variability

Warming of waters at the ITM is observed at all depths over the course of the record (Figure 3.3a; Table 3.2). The asynchronicity of the warming at different depths indicates multiple mechanisms and timescales of ocean property variability. We present evidence of large-scale events that impact properties on the continental shelf and inside the cavity concurrently. Our analysis suggests that shallow properties at the ITM respond quickly to changes on the shelf via propagation of internal waves, while the properties of inflowing AIW observed primarily at 500 m vary more slowly. Finally, the outflowing glacially modified water adjusts to the change in inflow properties with some lag, and is also influenced seasonally by subglacial runoff (see Section 3.3.4).

In late November 2016, the 266 m temperature at PF warms abruptly by about 0.4°C within two days (see Section 3.3.1; Figure 3.3a). The onset of warming within the cavity is then observed at the ITM at 150 m and 250 m, with a lag of about one day. This coincides temporally with a shift in circulation, where the along-fjord currents reverse from predominantly inflow to predominantly outflow (Figure 3.3c). Warming of at least 0.15°C is observed at 150 m, 250 m, and 350 m by the end of December 2016 (Figure 3.3a). This late fall warming signal is not observed at 500 m, suggesting that it is confined above the sill depth of approximately 480 m (Schaffer et al., 2020). In T-S space, observed properties during this period of warming vary approximately parallel to the melt line at 150 m and 250 m (Figure 3.6a-b; green arrows). At 350 m, the variation in T-S properties is initially close to the melt slope but becomes steeper later in December 2016 (Figure 3.6c; green arrow). The melt slope is similar to the slope of the initial T-S properties observed at the ITM (see Section 3.3.1). Based on the August 2016 stratification, we speculate that this warming and salinification correspond to upward isopyncal displacement of about 50 m at the three shallower instruments (Figure 3.2a-b).

The lag relationship between this warming signal at the two moorings suggests that it propagated into the cavity from the continental shelf. The mode one internal wave phase speed calculated using the August 2016 profile of buoyancy frequency N^2 (Chelton et al., 1998) at the ITM site is on the order of 50 cm s^{-1}, resulting in an approximate travel time of 19 hours between the mooring at the ice front and the ITM. (N^2 ranges from 0.5–2$\times$10^{-5} s^{-2} between 150 and 350 m.) The current velocities at the ITM at the onset of this warming are order 1 cm s^{-1}, yielding an advective timescale of days to weeks between the ice front and the ITM; furthermore the along-fjord flow during this period is directed out of the cavity (Figure 3.5c). The T-S characteristics of the warming signal, the brief lag between its arrival at the two moorings, and the simultaneous outflowing currents suggest a vertical displacement of isopycnals on the continental shelf that likely propagated into the cavity as a wave, rather than advection of a different water mass. This indicates an effective mechanism by which above-sill ocean properties within the cavity may respond to changes on the continental shelf on timescales of hours to days. Because the warming persists at both the ITM near the northern edge of the cavity and the PF

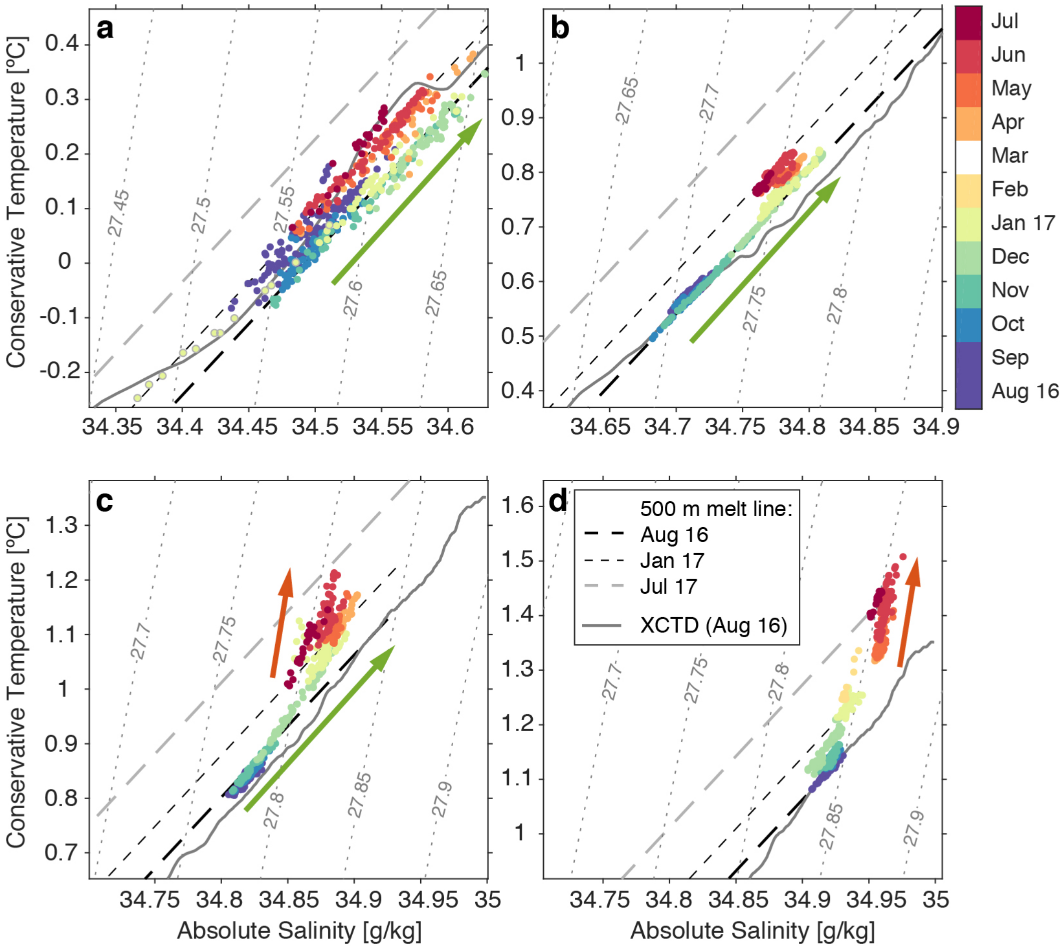

Figure 3.6. Time-varying (2 points per day) temperature vs. salinity plots for (a) 150m, (b) 250m, (c) 350m, (d) 500m at the ITM. The initial XCTD profile from August 2016 is plotted as a solid grey line. The dashed lines indicate the Gade slope relative to the 500m water mass properties in August 2016 (thick black), January 2017 (thin black), and July 2017 (grey). Green arrows (parallel to the melt line) in (a-c) indicate trajectory of warming during November-December 2016. Red arrows (parallel to isopycnals) in (c-d) indicate trajectory of AIW warming during January-July 2017. Grey circled points in (a) correspond to the grey shaded time period of January 2017 in Figure 3.3a-b.

site near the southern edge of the ice front, it likely affects the cavity properties over much of its width in the vicinity of the front where the ice draft is relatively shallow.

Higher frequency temperature and salinity variability observed at the ITM, on timescales of days to weeks, is greatest at 150 m (see Section 3.3.1; Figure 3.3a-b). Similar to the warming signal described above, this variability is characterized primarily by fluctuations parallel to the melt line in T-S space (Figure 3.6a), suggesting that it reflects vertical motion of isopycnals. A notable exception to this pattern occurs over eight days in late January 2017, when the coldest and freshest conditions of the entire record are observed at 150 m (Figure 3.3a-b; shaded). The strongest observed flow occurs at the same time, with a mean current velocity greater than 10 cm s^{-1} toward the northeast (Figure 3.3c-d). In T-S space, this cooling and freshening signal falls above the meltwater mixing line (Figure 3.6a; grey-circled points). As the properties depart the mixing line, they instead fall close to the August 2016 T-S profile, with the minimum temperature (-0.24°C) and salinity (34.37 g kg^{-1}) (Figure 3.3a-b) corresponding to properties observed at approximately 125 m depth (Figure 3.2a-b). Cooling at 266 m depth at PF, which likely indicates deepening of the pycnocline, is observed beginning a few days before the onset of the ITM cooling event (Figure 3.3a). This suggests that the transient cooling and freshening observed at 150 m at the ITM in January 2017 is linked to a larger-scale event that also affects the continental shelf. Potential mechanisms are discussed further in Section 3.4.1.

In contrast to the fall 2016 warming and high-frequency variability, the warming observed at 500 m beginning in late December 2016 and continuing through summer 2017 occurs primarily along the 27.86 isopycnal (Figure 3.6d; red arrow), indicating advection of a warmer water mass at the ITM location. During spring 2017, the T-S properties at 350 m similarly deviate from the melt line and become more similar to the properties at 500 m (Figure 3.6c), and the mean 350 m current direction is into the cavity during this period (Figure 3.5b), suggesting thickening of the inflowing AIW layer at the same time as it is warming and freshening. The 150 m and 250 m properties continue to warm through the end of the record, but high frequency variations in properties are still primarily parallel to the melt slope, which is consistent with the interpretation that these outflowing waters are glacially modified AIW. (Figure 3.6a-b). This warming and freshening of the AIW properties is not observed at PF until July 2017 (Figure 3.4), indicating that while ocean properties at the PF location may be linked strongly to above-sill cavity properties, it is isolated from the major AIW inflow pathway.

The AIW observed at the ITM location at 500 m warmed by 0.4°C between late December 2016 and June 2017 (Figure 3.3a). In July 2018, observed temperatures at 500 m and 150 m were close to their 2016-2017 maxima, while waters at 250 m and 350 m had warmed beyond their July 2017 maxima by 0.18°C and 0.05°C, respectively (Figure 3.2a). While the 150 m temperature was highly variable, with a range overlapping all previous CTD measurements, for the duration of the mooring record the 350 m and 500 m temperatures were consistently higher than in any observations prior to 2016. Furthermore, the magnitude of subannual AIW temperature variability observed at 500 m is smaller than previously observed interannual variability, indicating that AIW in the 79NG cavity has warmed since 1998.

The change in AIW inflow properties provides another possible observational constraint on cavity renewal timescale. At the end of the ITM record (mid-July 2017), T-S properties at 250 m fall along a melt line relative to the 500 m properties in mid-January 2017 (Figure 3.6b). This is consistent with our interpretation that the inflowing AIW observed at the ITM is carried toward the 79NG grounding line, is modified through basal melt of the ice tongue, and is exported at shallower depths. Furthermore, the timing suggests an approximately six-month, or 180-day lag between the arrival of an inflowing parcel of AIW at the ITM location and its subsequent export through the melt-driven circulation. This estimate falls within the lower end of residence timescales estimated from mean currents observed between April and July 2017 (see Section 3.3.2), agreeing well with the estimate in Schaffer et al. (2020). (Properties observed at 150 m are not mentioned here because they are likely more strongly influenced by runoff modification during this time period; see Section 3.3.4.)

3.3.4 Impacts of seasonally variable runoff

We can find evidence of mixing with subglacial runoff on T-S plots by identifying waters that are anomalously fresh compared to a melt slope, as described in Section 3.3.1. To consider the temporal variability in subglacial runoff concentration, we define an "effective salinity" as the salinity where a melt slope intersects the freezing line in T-S space. Changes in the effective salinity of glacially-modified waters therefore reflect property changes that cannot be accounted for solely through changing the proportion of basal melt, such as the addition of surface runoff, though it is also affected by variability in the AIW endmember properties.

We show the difference in effective salinity between 150 m and 250 m (ΔS_{eff}) at the ITM in Figure 3.7c (red). Assuming that waters at 250 m are not modified by mixing with subglacial runoff, which they are not in August 2016 (Figure 3.2b), and that waters at 150 m and 250 m respond to changes in AIW properties at the same rate, we expect the addition of runoff at 150 m to manifest as a positive value of ΔS_{eff}. In late August 2016, when we deduce the presence of runoff at 150 m from the temperature and salinity profiles at the ITM location, ΔS_{eff} is at a maximum value of 0.024. ΔS_{eff} remains greater than 0 in September 2016 and is again positive in July 2017 ($p<0.001$). This timing is consistent with the timing of summer ice sheet surface melt in the 79NG catchment area derived from RACMO (Figure 3.7c, blue; Noël et al. (2018); Slater et al. (2019)). We thus interpret ΔS_{eff} as a proxy for runoff concentration at 150 m the ITM.

Surface melt volume explains 80% of variability in ΔS_{eff} with a one-month lag (correlation $R^2 = 0.80$, $p=0.002$). Such a lag in the response of observed runoff concentration to surface melt is reasonable due to the time needed for meltwater to travel through the

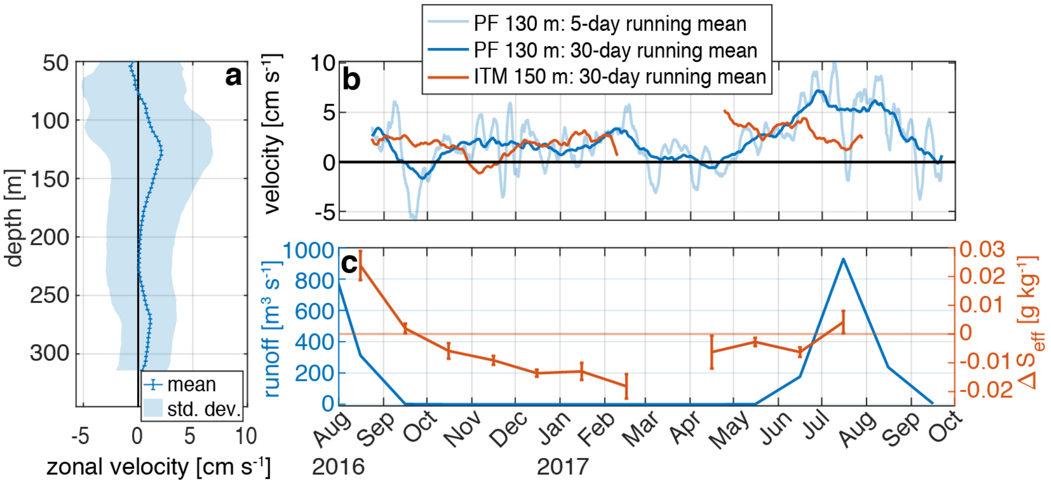

Figure 3.7. (a) Depth profile of time mean zonal velocity at the PF site. Error bars indicate the standard error of the mean; the shaded area indicates the standard deviation. (b) Timeseries of 130 m zonal velocity at the front mooring, 30-day running mean (dark blue) and 5-day running mean (light blue), and 150 m along-fjord velocity at the ITM, 30-day running mean (red). (c) Monthly average of subglacial runoff volume flux from RACMO (blue). Monthly average of difference in effective salinity between 150 m and 250 m ΔS_{eff} at ITM (red). If positive, indicates that waters at 150 m are fresher relative to 250 m than would occur purely through increasing basal melt concentration. Error bars indicate standard error of the mean (see 3A).

glacial hydrologic system to the grounding line and the additional advection time from the grounding line to the ITM. At the April-July mean 150 m current speed of 3.1 cm s^{-1}, a water parcel would be advected from the grounding line to the ITM location in 22 days. An analogous property signal is difficult to identify in the timeseries from the PF mooring due to the low vertical resolution of salinity sensors, but runoff was inferred to be present at the PF site above 245 m in the August 2016 observations (Figure 3.2c).

At the PF site outside the ice front, the mean zonal current velocity at 130 m, inferred to reflect outflow from the cavity, is above 5 cm s^{-1} throughout June-August 2017, significantly higher than the September 2016-May 2017 average of 1.1 cm s^{-1} (Figure 3.7b). This acceleration could be associated with an increased export of glacially-modified waters from the cavity. In contrast, there is no significant seasonal change in export velocity at the ITM through the end of the record. Localization of an outflowing plume of buoyant glacially-modified water toward the southern side of the 79NG cavity is consistent with the expected effect of the Coriolis force, even in the presence of basal channels (e.g. Millgate et al., 2013). These results suggest that melt runoff is present in shallow waters throughout the cavity during the summer months and likely drives seasonal circulation changes by increasing the volume flux from the cavity, with the main export concentrated near the southern edge of the cavity.

3.3.5 Basal melt variability

Remote sensing, in situ radar, and hydrographic analyses have found that ice shelf basal melt rates are highly variable in space (e.g. Wilson et al., 2017; Langley et al., 2014; Stewart et al., 2019), and additionally suggest significant temporal variability on daily to interannual timescales (e.g. Mayer et al., 2018; Washam et al., 2019; Schaffer et al., 2020; Adusumilli et al., 2018; Stevens et al., 2020). We use the ITM observations and an established model of basal ice melt (e.g. Jenkins et al., 2010) to generate independent estimates of melt rate variability through two different approaches. First, we use the full record to calculate a timeseries of local basal melt at the ITM site. We then use a plume model (e.g Jenkins, 2011; Slater et al., 2017; Mayer et al., 2018) to estimate the subannual change in basal melt in the vicinity of the grounding line associated with the observed warming of deep AIW. (The melt rate and buoyant plume parameterizations are described in Section 2.3.)

We employ the three-equation formulation of Jenkins et al. (2010) (Equations 2.2a-c) to calculate the local basal melt rate, using the unfiltered timeseries of temperature, salinity, and current speed (i.e. the square root of summed squares of the along- and cross-fjord velocities) from the ITM at 150 m depth, which is closest to the depth of the ice base (Figure 3.8a). The melt rate calculation additionally relies on the Thermal Stanton number St_T, a nondimensional parameter that depends on a heat transfer coefficient and the drag coefficient at the ice shelf base, both of which are uncertain. We use a range of values for St_T from 4.5×10^{-4} to 1.3×10^{-3}, derived from observations under an Antarctic ice shelf (Stanton et al., 2013; Davis et al., 2018), to estimate uncertainties for the computed melt rates, represented by the grey shading in Figure 3.8b.

We estimate a time-mean melt rate of 8.3 – 23.1 m yr^{-1}, which is consistent with the Wilson et al. (2017) estimate in the vicinity of the 79NG rift (6.5 ± 2.8 m yr^{-1}). We discuss temporal variability of the timeseries calculated with $St_T^* = 8.5 \times 10^{-4}$ (Figure 3.8b; black line), but the relative values are independent of the choice of St_T, assuming its value is constant in time. The time-mean melt rate for St_T^* is 15.7 m yr^{-1} with standard deviation 9.3 m yr^{-1} (60%), revealing considerable temporal variability. The variability of the timeseries of basal melt closely resembles the variability in current speed, which is expected, because the variability in speed is much greater than the variability in thermal forcing on timescales of days to weeks (Figure 3.8a-b). However, the January-July 2017 mean (17.9 ± 1.0 m yr^{-1}) is 33 ± 20% higher than the August-November 2016 mean (13.6 ± 1.3 m yr^{-1}) (Figure 3.8b; see Appendix 3A for calculation of the standard error of the mean). We find that this significant increase in melt rate ($p = 0.001$) cannot be explained by changes in current speed and attribute it to sustained ocean warming.

This approach relies on some key assumptions. We assume that currents at the ITM location are not affected by drag from the ice base, and crucially, that despite being below a rift, these observations are representative of conditions at the ice tongue base nearby. This can be justified to an extent by the fact that the rift is relatively narrow (see Section 3.2), but it is very likely that the salinity adjacent to the ice base is lower than what is observed at the ITM due to the accumulation of buoyant meltwater. As a result, this method is likely to overestimate melt rates, and the reported magnitudes should be interpreted with particular caution. Nevertheless, we note that the resulting estimate of mean melt rate agrees within uncertainty with the independent result of Wilson et al. (2017), and focus our interpretation on the additional information about relative temporal variability provided by this approach.

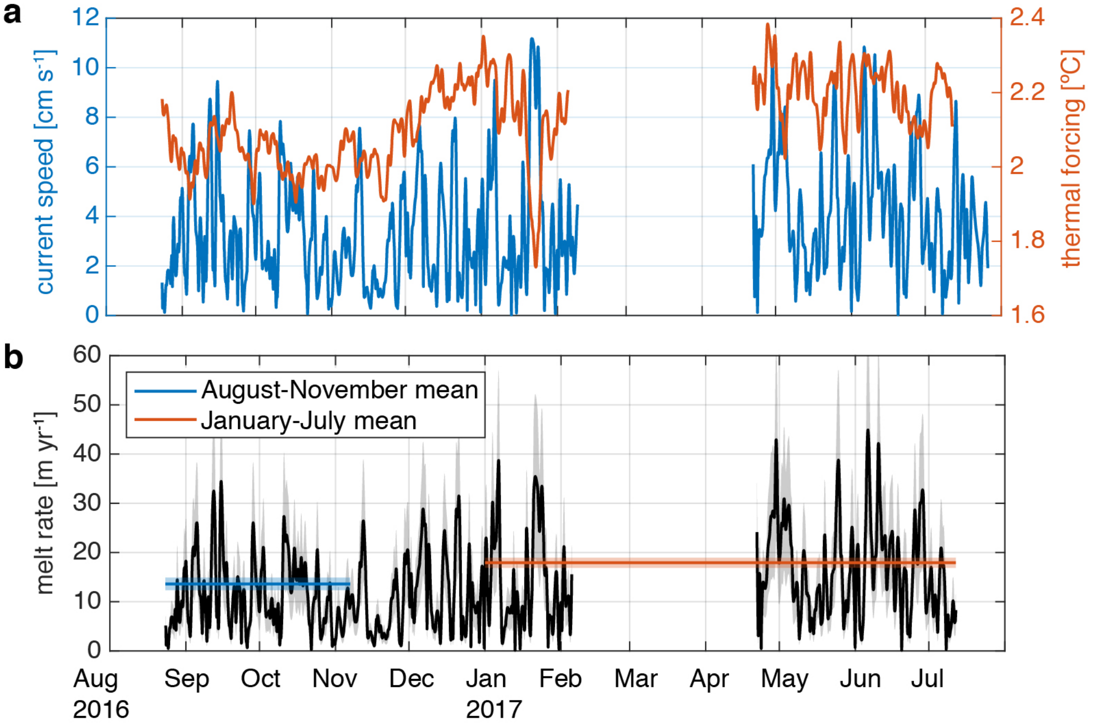

Figure 3.8. (a) Timeseries of horizontal current speed at 150m (blue) and thermal forcing $T - T_f$ (red). (b) Timeseries of computed basal melt rate (black). The black line is calculated using $St_T^* = 8.5 \times 10^{-4}$; grey shading indicates the range of melt rates resulting from varying St_T between 4.5×10^{-4} and 1.3×10^{-3}. The August-November (blue) and January-July (red) time means using St_T^* are plotted over the corresponding time periods, with shaded bars indicating the standard error of each mean value (see 3A).

At 79NG, the largest overall melt rates occur in the vicinity of the grounding line, where the ice base is in contact with the warmest water and the freezing point is depressed due to higher pressure (Wilson et al., 2017). We use the 1-dimensional, nonrotational line plume model given by Slater et al. (2017) (Equations 2.3a-d) to estimate the impact of the observed warming on basal melt over the region of the ice tongue up to 12 km downstream of the grounding line, where the ice tongue base slope is steepest. The ice tongue base in this region is between 250 m and 600 m deep (Wilson et al., 2017). We force the plume model with monthly mean T-S profiles observed at the ITM, under the assumption that ocean properties observed at the ITM are representative of waters reaching the grounding zone at equivalent depths. We exclude subglacial runoff input at the grounding line to isolate the effect of ocean warming, but note that it is expected to seasonally enhance basal melt. Unconstrained model parameters in addition to St_T, including the entrainment coefficient, affect the absolute magnitudes of melt simulated by the plume model; thus, we report only the relative change in melt rates, which is robust to variation of these parameters. Using October 2016 as a baseline, we estimate that 2016-2017 ocean warming drives a 14 ± 2% increase in basal melt rate, which, if sustained, could drive further thinning of the ice tongue grounding zone.

3.4 Discussion

The ITM record represents the first observations of temporal variability in the properties of waters and currents in the 79NG cavity on hourly to subannual timescales. The mean overturning circulation observed inside the 79NG cavity, together with the ocean properties, are consistent with the glacial melt-driven estuarine circulation inferred by Wilson and Straneo (2015), and comparison with the record from Schaffer et al. (2020) suggests that circulation and properties at the ITM location are linked to variability of the hydraulically controlled inflow. Our results suggest that several processes likely interact to drive the complex and variable ocean circulation in the cavity that determines 79NG ice tongue basal melt. In the following, we discuss potential mechanisms of the observed variability and their implications for the ice tongue.

3.4.1 Continental shelf-driven variability

The abrupt warming of shallow waters in November 2016 is observed first at the mooring outside the front, suggesting a mechanism driven by processes on the continental shelf. A recent study of mooring records from the shelf shows large-scale warming and thickening of the AIW layer during the same time period (Schaffer et al., 2020), indicating that both the shallow and deep warming signals observed at the ITM were likely driven by this external variability. Schaffer et al. (2020) show that AIW inflow into the 79NG ice tongue cavity is concentrated below 350 m depth, and is hydraulically controlled by a shallow sill outside the pinned front. Beginning in November 2016, thickening of the AIW layer upstream of the sill by 50 m drove enhanced AIW transport into the cavity. This finding supports our interpretation that the initial warming of the shallow waters was driven by the propagation of the isopycnal shoaling signal from the shelf as the layer thickened. The subsequent warming of the AIW at 500 m with a lag of approximately one month is thus understood to be the advection of the warmer AIW from the pinned front to the ITM location.

A warm anomaly in Atlantic waters observed on the continental slope in the mid-2000s may offer an analogue to the AIW warming observed in the 79NG cavity between January and July 2017 (Beszczynska-Möller et al., 2012). Between hydrographic surveys in summer 2005 and 2006, the recirculating Atlantic water (RAW) layer in the EGC warmed by 0.25°C and freshened by about 0.02 psu. Similarly, AIW observed at 322 m at PF from July through September 2017 was observed to warm by about 0.1°C and freshen by as much as 0.02 g kg^{-1}, resulting in a decrease in density of 0.02 kg m^{-3} (Figure 3.2c). de Steur et al. (2014) found that the mid-2000s warming caused a similar density anomaly, which was linked to thickening of the RAW layer on the continental slope. The anomalous warming and thickening of the RAW were both reversed in the following years (through 2011), though the long-term warming trend appeared to persist (Beszczynska-Möller et al., 2012; de Steur et al., 2014). This suggests the possibility of a reversal of the relatively rapid 0.4°C warming observed by the ITM at 500 m during 2017 and a return to the more gradual warming suggested by the earlier observations.

There is noticeable variability in the currents and ocean properties observed at the ITM on timescales of days to weeks, with larger variance at shallower depths (Figure 3.3a-d), though this is not associated with a significant spectral peak. Münchow et al. (2020) find that topographic Rossby waves generated by offshore Ekman pumping propagate along Norske Trough with periods of 6-20 days. This could drive oscillations in the AIW layer thickness at the sill outside the pinned front, which may result in isopycnal oscillations in the cavity as suggested above, as well as modulating the inflow strength and causing variability in currents observed at the ITM (Schaffer et al., 2020).

In particular, internal waves on the continental shelf offer a possible explanation for the strong shallow outflow observed at the ITM during the January 2017 cooling and freshening event discussed in Section 3.3.3. Cooling observed at PF (Figure 3.3a) and results from Schaffer et al. (2020) indicate that this event is preceded by lowering of the pycnocline on the shelf by about 50 m. Their results show enhanced outflow through the pinned front, with the peak roughly coinciding with the initiation of the anomaly observed at the ITM, suggesting that this event could be part of a larger scale rearrangement of circulation in response to shelf forcing. However, the dominant processes driving current variability in the cavity remain unclear, and there are numerous possible explanations for this signal. For example, Washam et al. (2019) observe qualitatively similar events beneath Petermann Gletscher, i.e. cold, fresh pulses with increased current speeds, and attribute these to intermittent releases of subglacial runoff from the grounding line. Such an outflow from beneath the ice tongue, if sufficient in magnitude and localized on the southern side of the cavity due to Coriolis (see Section 3.3.4), could be responsible for the depression of the pycnocline outside the pinned front before the corresponding signal was observed at the ITM. The influence of subglacial runoff at 79NG is discussed further in the next section.

3.4.2 Glacier and cavity variability

We find evidence that seasonal subglacial discharge of ice sheet surface runoff affects cavity circulation and temperature-salinity structure both within the cavity and outside the ice front (see Section 3.3.4). We expect that subglacial runoff at the grounding line enhances basal melting of the ice tongue according to both theory (e.g. Jenkins (2011)) and observations, including recent mooring records from Petermann Gletscher in northern Greenland (Washam et al., 2019). Schaffer et al. (2020) find that the glacier freshwater flux (i.e. subglacial runoff together with basal melt) contributes 1.4% to the time-averaged cavity overturning strength. Their theoretical prediction of overturning strength based on density gradients across the sill outside the pinned front agrees with their observational transport estimate throughout most of the year, but underestimates the overturning during May, June, and July. This is the period over which export at the PF site increases toward its summer maximum (Figure 3.7b). Thus, we infer that the freshwater flux constitutes a larger fraction of the overturning strength during the summer months, when subglacial runoff is present, relative to the annual mean.

Schaffer et al. (2020) find that 45% of outflow is directed through Dijmphna Sund, with the rest of the export through the pinned front, primarily through two gateways to the north of the PF mooring. While the prevailing flow direction at the ITM site at 150 m is inferred to be toward the pinned front (Figure 3.1a), currents are sometimes directed toward Dijmphna Sund, notably at 150 m during the cold pulse in January 2017, as well as intermittently throughout the year at the mid-depths as discussed in Section 3.3.2. This suggests that the proportion of outflow through the various gateways could vary on timescales of days to weeks. Additionally, there is likely seasonal variability due to the subglacial runoff forcing, with the gateway closest to the PF site potentially accounting for a larger proportion of the export during summer.

The October 2016 shift in circulation from the overturning mode to the barotropic inflow mode (Figure 3.5c) is not preceded by any change in properties or currents observed at the PF site, suggesting that it is driven by a mechanism internal to the glacier-cavity system. The inflowing currents at all depths must be compensated by outflow at another location (assuming current direction does not reverse below 500 m or at another depth not captured by the current meters), possibly indicating a transition from the vertically-sheared mean exchange flow to a primarily horizontally-sheared exchange. Cross-fjord variation in exchange flow with horizontal shear is likely a persistent feature in the 79NG cavity due to its large width relative to the deformation radius, but it could be enhanced by factors such as a change in stratification or frictional influence, as observed in some estuarine systems (Valle-Levinson, 2008; Lerczak et al., 2006). The potential role of stratification in setting the exchange flow structure offers an additional mechanism by which runoff seasonality could drive shifts in circulation. However, this framework does not offer a straightforward explanation for later changes in the velocity profile observed at the ITM.

3.4.3 Ice tongue stability

Our estimates of residence time are broadly in agreement with other studies suggesting that renewal of ocean water in the 79NG cavity occurs within one year, and likely faster, with lower bounds of approximately four to six months (Wilson and Straneo, 2015; Schaffer et al., 2020). If the renewal timescale is sufficiently fast, ice tongue melt is predicted to increase proportionally to the square of a sustained temperature change (Holland et al., 2008b; Holland, 2017). The timescale of deep AIW warming inside the 79NG cavity observed in the ITM record, beginning in December 2016 and apparently sustained through July 2018, is likely longer than the residence time of the cavity, and could thus be expected to accelerate thinning in the vicinity of the grounding line, which is presumably ongoing, to accelerate (Mouginot et al., 2015). Furthermore, the warming in November 2016 suggests an efficient mechanism for the shallow waters inside the cavity to adjust to changes on the shelf within weeks, causing a 33 ± 20% increase in estimated mean melt rate locally (Figure 3.8b). This could cause thinning in the vicinity of the ice front, where the ice draft is above the sill depth. The thinner ice is more vulnerable to rifting, which could ultimately result in significant calving, as observed at Petermann Gletscher (Münchow et al., 2014), though historical observations and modeling studies indicate that the bathymetric pinning points at the mouth of the 79NG cavity have a strong stabilizing influence on the ice tongue (Mouginot et al., 2015; Choi et al., 2017).

An improved mechanistic understanding of subannual variability will improve our understanding of the recent past and long-term fate of 79NG ice tongue. The ice tongue appears to have begun to thin in the early 2000s (Mouginot et al., 2015), coinciding roughly with summer breakups of previously quasipermanent landfast sea ice on the continental shelf (Sneed and Hamilton, 2016). Warming air temperatures drove increased surface melt of the ice sheet at around the same time (Khan et al., 2014; Mouginot et al., 2019; MacFerrin et al., 2019; Noël et al., 2018), likely causing subglacial runoff to increase (Slater et al., 2019). AIW has also warmed during that period (Figure 3.2a; Mayer et al. (2018)). Each of these changes has seasonal or sub-annual analogues that can provide insight into changes in the 79NG cavity in the early 2000s, the ocean's role in the ice tongue thinning, and how these are likely to change in the future.

Changes in ice tongue thickness affect the ice tongue's buttressing of NEGIS, which holds a 1.1 m sea level equivalent (Morlighem et al., 2014). New studies indicate that the ocean around northeast Greenland is likely to experience the most dramatic warming of any Greenland region through 2100 (Slater et al., 2019), and suggest that ocean warming may have driven major retreat of the 79NG grounding line relative to its present position during the Last Glacial Period (specifically 41–26 ka; Tabone et al. (2019)). An extended observational timeseries over multiple seasonal cycles would significantly improve our ability to distinguish between the various drivers of variability discussed here. The interpretation of these records would be further aided by additional measurements in other regions of the ice tongue and improved mapping of the bathymetry in and around the 79NG cavity.

3.5 Conclusion

We present the first moored record of ocean circulation and property variability in the 79NG cavity. The deep cavity is filled with warm AIW year-round, and the upper water column is primarily filled with colder, fresher glacially-modified water, including runoff-modified water during the summer and early fall. We find that sub-annual variability in AIW temperature inside the cavity is smaller than interannual variability, and conclude that waters in the 79NG cavity have warmed since 1998.

We observe a mean along-fjord overturning circulation, with inflow of warm AIW at depth and export of glacially modified water near the ice tongue base. Shallow currents are highly variable on 3-10 day timescales, and the influence of tidal currents is minor. A secondary mode of along-fjord circulation is characterized by strong in- and outflow at the mid-depths lasting weeks to months during late fall and early winter 2016. Currents are intermittently directed toward Dijmphna Sund to the north, especially in the mid-depths.

Warming and thickening of the AIW layer observed on the continental shelf in late fall 2016 causes warming observed at the shallow- and mid-depths at the ITM within one day, suggesting a wave-like mechanism for rapid propagation of ocean property variability into the cavity. Advection of warmer AIW at the ITM site is observed first at 500 m in late December 2016, resulting in warming of 0.4°C through mid-July 2017. Thickening of the AIW within the cavity is observed during spring 2017. Subglacial runoff discharged at the grounding line is inferred to drive variability in ocean properties inside the cavity in fall 2016 and summer 2017, as well as circulation variability observed at the PF mooring in summer 2017.

Our results suggest that ocean properties in the 79NG cavity are closely linked to variability on the continental shelf, with changes in stratification and water mass properties propagating into the cavity on timescales of days to months, and a renewal timescale of under one year. Therefore, we expect basal melt of the 79NG ice tongue to be sensitive to ocean variability driven by large-scale and continental shelf processes (Schaffer et al., 2020; Münchow et al., 2020). This is consistent with the inferred link between observed ice tongue thinning and ocean warming (Mayer et al., 2018), suggesting that ocean property variability is crucial to interannual variability and long-term thinning of the 79NG ice tongue.

3A Appendix: Calculation of the standard error of the mean for an autocorrelated time series

The standard error of the mean $\bar{\sigma}$ is calculated as

$$\bar{\sigma} = \frac{\sigma}{\sqrt{N_{\text{eff}}}}, \tag{3.1}$$

where σ is the standard deviation and N_{eff} is the number of degrees of freedom of the sample. For an autocorrelated time series, N_{eff}, also known as the equivalent sample size, is fewer than the total number of observations N. Following von Storch and Zwiers (1999), we calculate a decorrelation timescale τ_D for each of the observed time series as

$$\tau_D = \max\left(1 + 2\sum_{k=1}^{n-1}(1 - \frac{k}{n})\rho(k), n\right), \tag{3.2}$$

where $n = 2, ..., N$ and k is the lag of the autocorrelation function $\rho(k)$. The equivalent sample size used in equation 3.1 is thus calculated as

$$N_{\text{eff}} = \frac{N}{\tau_D}. \tag{3.3}$$

Acknowledgments

Chapter 3, in full, is a reprint of the material as it appears in Journal of Geophysical Research: Oceans, 2020. DOI:10.1029/2020JC016091. Margaret R. Lindeman, Fiammetta Straneo, Nat J. Wilson, John M. Toole, Richard A. Krishfield, Nicholas L. Beaird, Torsten Kanzow, and Janin Schaffer. The dissertation author was the primary investigator and author of this paper.

Chapter 4

Observational constraints on iceberg melt processes in Sermilik Fjord, southeast Greenland

4.1 Introduction

Iceberg calving from marine-terminating glaciers constitutes a significant fraction of Greenland Ice Sheet discharge, with the majority of iceberg mass thought to melt within fjords (Moon et al., 2018; Moyer et al., 2019; Rezvanbehbahani et al., 2020). Theory and models have shown that iceberg melt is a major component of glacial fjord heat and freshwater budgets and contributes to the buoyancy-driven circulation (Enderlin et al., 2016; Jackson and Straneo, 2016; Davison et al., 2020). Furthermore, iceberg melt may modify the properties of ocean waters reaching the glacier terminus, potentially affecting glacier dynamics (Davison et al., 2022). These processes have likely grown in importance as GrIS ice discharge has accelerated (King et al., 2020).

As computational capabilities increase and icebergs are beginning to be included in fjord-scale ocean models (Davison et al., 2020), observational constraints are needed to evaluate the simulated representation of the resulting meltwater distribution. However, there are few direct observations of iceberg melt. Our knowledge of iceberg meltwater distribution and mixing in glacial fjords comes primarily from models and laboratory simulations due to the difficulty of making ocean measurements close to icebergs (FitzMaurice et al., 2017, 2018; Moon et al., 2018; Meroni et al., 2019; Hester et al., 2021). In open ocean studies, meltwater can often be attributed to an individual iceberg in observations from over 400 m away because there are no other proximal sources of melt (Stephenson et al., 2011; Yankovsky and Yashayaev, 2014), which is not typically the case in a glacial fjord with a high concentration of icebergs.

Here we present observations of subsurface meltwater plume intrusions close to a large iceberg in Sermilik Fjord. Adopting the approach of Jackson et al. (2020), we compute the melt fraction and plume height for the observed intrusions and compare them to characteristics simulated by a melt plume model. We find that the simulation does not capture the observed properties even with modifications to the model coefficients, raising the possibility that the existing parameterization is ill-suited to modeling iceberg melt in this environment.

4.2 Background

4.2.1 Marine-terminating glaciers in Greenland fjords

Since the early 2000s, mass loss from the Greenland Ice Sheet (GrIS) has accelerated, increasing the associated freshwater fluxes to the ocean via glacial fjords (e.g. Mouginot et al., 2019; King et al., 2020). These fluxes take multiple forms, including discharge, which comprises iceberg calving and ocean melting of glacier termini; and runoff of surface melt (e.g. Bamber et al., 2018). Each of these processes has different effects on fjord stratification and circulation, which can have feedbacks on melt rate and determines the properties of glacially-modified waters exported to the open ocean (e.g. Straneo and Cenedese, 2015).

Studies of Sermilik Fjord in southeast Greenland have used heat and freshwater budgets (Jackson and Straneo, 2016) and tracer observations (Beaird et al., 2018) to partition submarine melt and runoff. However, these methods cannot distinguish between subsurface melting of the terminus versus icebergs, which are likely influenced by environmental conditions in distinct ways. Recent remote sensing (Enderlin and Hamilton, 2014; Enderlin et al., 2016) and modeling (Moon et al., 2018) studies suggest that iceberg melt is the largest component of the Sermilik freshwater budget. Furthermore, Davison et al. (2020) find that adding iceberg melt to simulations of Sermilik Fjord strengthens export velocities further from the terminus, where the terminus melt- and runoff-driven circulation is strongest, and also increases the depth of glacially-modified water export. Thus distinguishing the distribution and impacts of iceberg melt from submarine melt of the glacier terminus could be relevant to understanding glacial fjord dynamics.

Historically, models of ocean response to glacier melt have assumed that all meltwater input, including iceberg melt, occurs in the surface layer. In the case of iceberg melt, this picture neglects the role of shear, which may efficiently advect and mix meltwater into the ambient ocean at depth, and stratification, which limits the buoyancy of melt plumes in more quiescent environments such that they are likely to reach neutral buoyancy below the ocean surface (FitzMaurice et al., 2016; Magorrian and Wells, 2016; Jackson et al., 2020). Subsurface intrusions of meltwater upwelling plumes have been identified in observations 0.4-1.8 km away of a large tabular iceberg (length scale 10s of km) in the Weddell Sea (Stephenson et al., 2011). In contrast, the largest icebergs in Sermilik Fjord have a length scale of under 1 km (Sulak et al., 2017), and melt in a water column that is strongly influenced by submarine melt of the glacier terminus and other icebergs, posing a challenge to identifying a specific iceberg melt signature in observations.

4.2.2 Icebergs in Sermilik Fjord

Icebergs calve from the terminus of Helheim Glacier at the head of Sermilik Fjord, where they are initially incorporated into a dense ice melange that extends about 20 km down the fjord (Figure 4.1a). On average, the melange moves at about 20 m d^{-1}, with

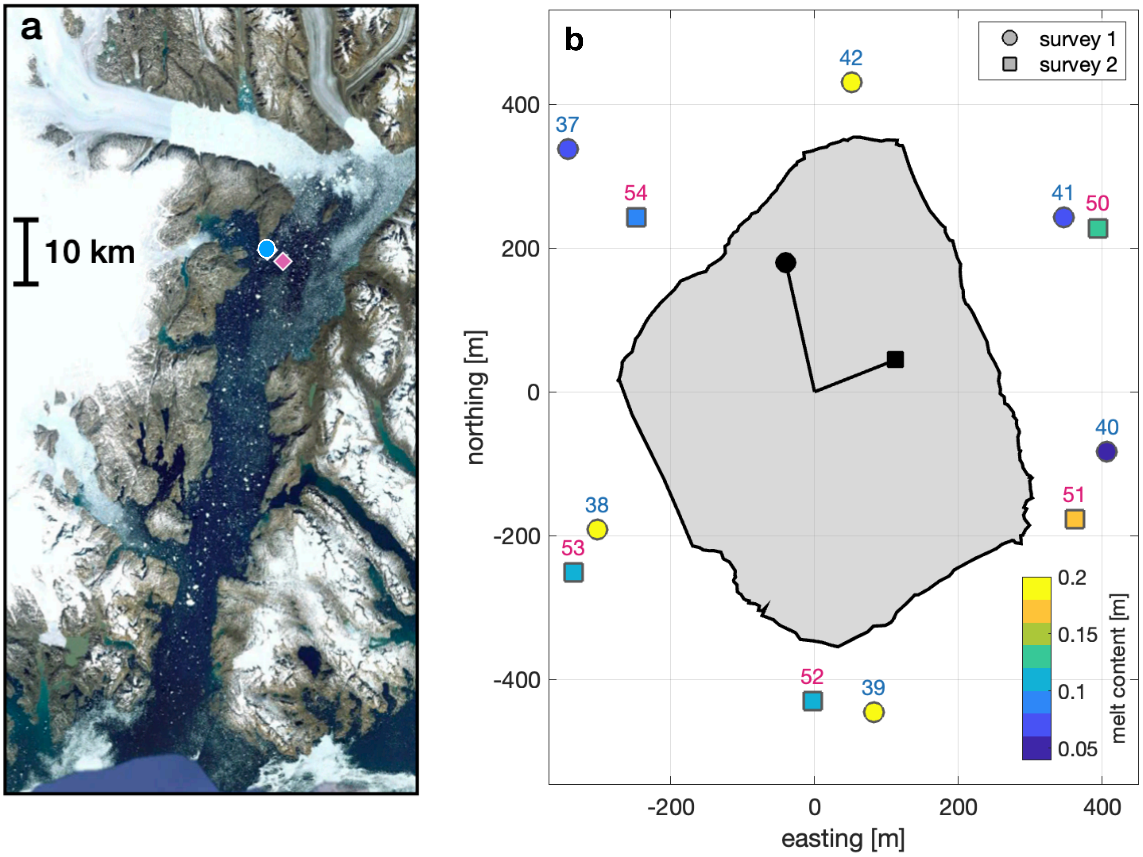

Figure 4.1. (a) Map of Sermilik Fjord showing locations of iceberg surveys 1 (blue) and 2 (pink). (b) Plan view of iceberg surface footprint and relative positions of each CTD profile location from surveys 1 (circles, casts 37-42) and 2 (squares, casts 50-54). The color indicates the integrated melt content for each profile. Vectors of the mean iceberg drift velocity during each survey are plotted over the iceberg footprint, scaled such that 100 m represents 1 cm s^{-1}. Cast numbers correspond to the list in Table 4.1.

intermittent increases in speed, likely controlled by glacier dynamics, and substantial melt occurs within this region (Sutherland et al., 2014; Enderlin and Hamilton, 2014). Beyond the melange, iceberg drift is primarily controlled by fjord circulation, and iceberg velocity is well-approximated by the mean current over the submerged iceberg draft (FitzMaurice et al., 2016). Observed residence times in the melange and fjord are highly variable, in both regions ranging from about one month to three months or longer (Sutherland et al., 2014). About 50-90% of iceberg melt is estimated to occur within the fjord (Moon et al., 2018; Moyer et al., 2019), with variation in residence time likely contributing to the spread in the estimates. Thus a combination of ocean and glacier dynamics (as well as intermittent strong wind events; Oltmanns et al., 2014) likely modulate the partitioning of melt-driven heat and freshwater fluxes between the fjord and shelf through mechanisms distinct from the drivers of terminus melt variability.

During the summer, the mean structure and circulation in Sermilik Fjord can be described as an estuarine system, with inflowing dense Atlantic Water (AW) from the shelf below 200 m and export of cooler, fresher glacially-modified waters above the pycnocline (Figure 4.3; Jackson and Straneo, 2016). This buoyancy-driven circulation is primarily sustained by input of fresh surface melt runoff that is discharged at the base of the glacier terminus, with some contribution from submarine melt of the terminus, as well as iceberg melt, which constitutes a spatially-distributed freshwater input along the length of the fjord (Straneo et al., 2011; Beaird et al., 2018; Davison et al., 2020).

The runoff-driven upwelling of relatively warm, salty AW delivers heat and macronutrients to the upper water column, enhancing submarine melt and primary production (Straneo and Cenedese, 2015; Cape et al., 2019). Some studies suggest that iceberg melt-driven upwelling could be an additional driver of vertical transport of nutrients (Smith et al., 2013; Meire et al., 2017), and in certain settings iceberg melt plumes could also upwell relatively warm water (Stephenson et al., 2011; Davison et al., 2022), although the anomaly between upwelled intrusion characteristics and the ambient properties is determined by the background temperature and salinity gradients.

In Sermilik and similar glacial fjords, during the summer the slope of $\frac{\partial T}{\partial S}$ is typically lower than the slope of the melt mixing line (Gade, 1979) due to the addition of runoff (see Section 2.1; Straneo et al., 2011; Straneo and Cenedese, 2015). As a result submarine melt appears as a cold along-isopycnal anomaly (Figure 4.4b). This can be contrasted to the average $\frac{\partial T}{\partial S}$ slope on the shelf (Figure 4.4a), which is steeper than the melt line. Stephenson et al. (2011) show that iceberg melt in the Weddell Sea can manifest as a warm anomaly in observations, and the model results of Davison et al. (2022) show that in a fjord with a steeper ambient T-S gradient there is a potential for iceberg upwelling to warm the upper ocean proximal to the glacier terminus. This could be the case in Sermilik Fjord during the winter, when conditions in the fjord are more similar to those on the shelf (Jackson et al., 2014).

Typically, submarine ice melt rates may be well-approximated as proportional to the ocean thermal driving (i.e. temperature above freezing) and shear (in the case of icebergs, the difference between the drift velocity and any ocean current). As mentioned above, FitzMaurice et al. (2016) show that iceberg melt in Sermilik Fjord can form either "detached" plumes, which are advected away due to shear relative to the background current, or "attached" plumes, which upwell along the iceberg face. Detached plumes are generally associated with higher melt rates than attached plumes, where the relevant shear is set by the plume velocity. However, the concentration of melt in attached plumes is primarily responsible for iceberg-driven upwelling, and we focus on this attached plume regime in this study.

4.2.3 Melt models and parameterizations

In the absence of significant background velocity, the onset of melting generates freshwater, which rises along the face of the iceberg, both melting the ice and entraining ambient water. In a stratified water column, these upwelling plumes typically reach neutral buoyancy below the ocean surface, which is theorized to result in stacked melt-driven convective cells (Huppert and Turner, 1980; Magorrian and Wells, 2016). This process is commonly modeled by coupling a submarine melt parameterization (Holland and Jenkins, 1999) to a buoyant plume model (Morton et al., 1956; Jenkins, 2011; Cowton et al., 2015). Analogous to the attached plume context described above, melting where the shear is primarily generated by melt plume velocity is also referred to as "ambient" melt, in contrast to melt controlled primarily by shear due to an external freshwater input (i.e. subglacial runoff plume) or strong background current.

Fjord-scale models that include icebergs cannot resolve this process, which would be prohibitively computationally intensive. Davison et al. (2020) account for the potential of "missing" plume-driven shear by imposing a minimum background velocity in their melt rate calculation, similar to the approach applied to a glacier terminus by Cowton et al. (2015). However, this does not account for the possibility of significant vertical transport by upwelling plumes.

Even when the full theory is applied, melt parameterizations are imperfect. Schild et al. (2021) estimated melt rates from observations of iceberg volume change and reconstructed submarine surface area, which yielded a much lower melt rate than the standard model. On the other hand, two recent observational studies of LeConte Glacier in Alaska found that melt parameterizations underestimate terminus melt and proposed substantial increases to the model coefficients as a remedy (Sutherland et al., 2019; Jackson et al., 2020). Additionally, studies such as FitzMaurice and Stern (2018) focus explicitly on very large icebergs (length scale greater than the deformation radius) typical of calving from Antarctic ice shelves, yielding parameterizations that are not likely to be applicable to smaller icebergs calved from Greenland's tidewater glaciers.

Furthermore, the assumption that melt rate is proportional to shear, which underlies most melt parameterizations, is broadly applicable in a range of environmental conditions but does not hold universally (Wells and Worster, 2008; McConnochie and Kerr, 2017).

The inner ice-ocean boundary layer effectively insulates the ice from the surrounding water, and high shear thins this layer, allowing for efficient fluxes of ocean heat and salt to the ice. However, theory shows that when shear is very low, a convective instability becomes the dominant control on boundary layer thickness, such that melt rate is independent of velocity (Wells and Worster, 2008). For a vertical ice face in this regime, the boundary layer is expected to be thinnest at low thermal driving. In a series of studies summarized in McConnochie and Kerr (2017), the authors show discrepancies between experimental and modeled melt rates in a range of laboratory conditions, which they suggest could indicate a transition between boundary layer regimes. This transition is even more difficult to identify in field observations.

In this study, we describe the spatial and vertical distribution of meltwater intrusions from a large iceberg in Sermilik Fjord, and characterize their meltwater content and associated upwelling plume height to provide observational constraints on some of these processes. By comparing the observational analysis to melt plume model simulations, we identify an inconsistency with the simulated relationship between velocity and melt content. We consider these results in the context of the Jackson et al. (2020) study of melt intrusion observations at LeConte Glacier and the insights of Magorrian and Wells (2016) into the underlying dynamics of the melt plume model, and propose a possible approach to identifying and addressing discrepancies between the melt plume model physics and ocean observations.

4.3 Methods

4.3.1 Iceberg surveys

We conducted oceanographic surveys of iceberg “Lars” from the M/V Adolf Jensen on August 8 and 10, 2018. Over this period the iceberg was located in the northern part of Sermilik Fjord at 66.15-66.17°N, east of a small bay (Figure 4.1a). These surveys included a total of 11 CTD profiles of temperature, salinity, and dissolved oxygen concentration measured 80-220 m away from the surface edge of the iceberg (Table 4.1; Figure 4.1b). Its surface footprint was 700 m by 640 m (estimated from drone imagery; Figure 4.1b), which puts it in the upper 0.001% of icebergs in Sermilik Fjord by surface area (Sulak et al., 2017). The keel depth was estimated to be 320 m based on a multibeam sonar survey, though the maximum depth is likely greater if there is any undercutting of the iceberg. We compare the survey profiles to an estimated "ambient" profile based on 13 reference profiles measured in the northern part of the fjord between August 8 and 11. All temperature and salinity values are reported as Conservative Temperature and Absolute Salinity, respectively (McDougall and Barker, 2011).

Table 4.1. List of casts for each survey. The distance given is between the CTD cast location and the edge of the iceberg surface footprint at the start of the cast.

Date	Time	Cast No.	Distance [m]
8 Aug 2018	12:57	37	237
	13:27	38	193
	13:54	39	108
	14:25	40	122
	15:07	41	159
	15:42	42	80
10 Aug 2018	10:36	50	199
	11:08	51	72
	11:43	52	76
	12:20	53	157
	13:08	54	102

4.3.2 Analysis of observed melt intrusions

The method used in this study to analyze iceberg melt intrusions was established by Jackson et al. (2020), who apply it to glacier terminus melt intrusions observed in a relatively warm ($\sim 6-8$°C) Alaskan fjord, LeConte Bay. Here it is very lightly adapted for application to iceberg melt in a lower thermal driving environment (Figure 4.3a). Their approach is summarized here and we refer the interested reader to their supplemental

Figure 4.2. Photographs of iceberg “Lars.” Top: Aerial view (credit: Kristin Schild). Bottom: Side view during survey 2. The white line indicates the width of a Jetyak used during the surveys ($\sim$ 1 m).

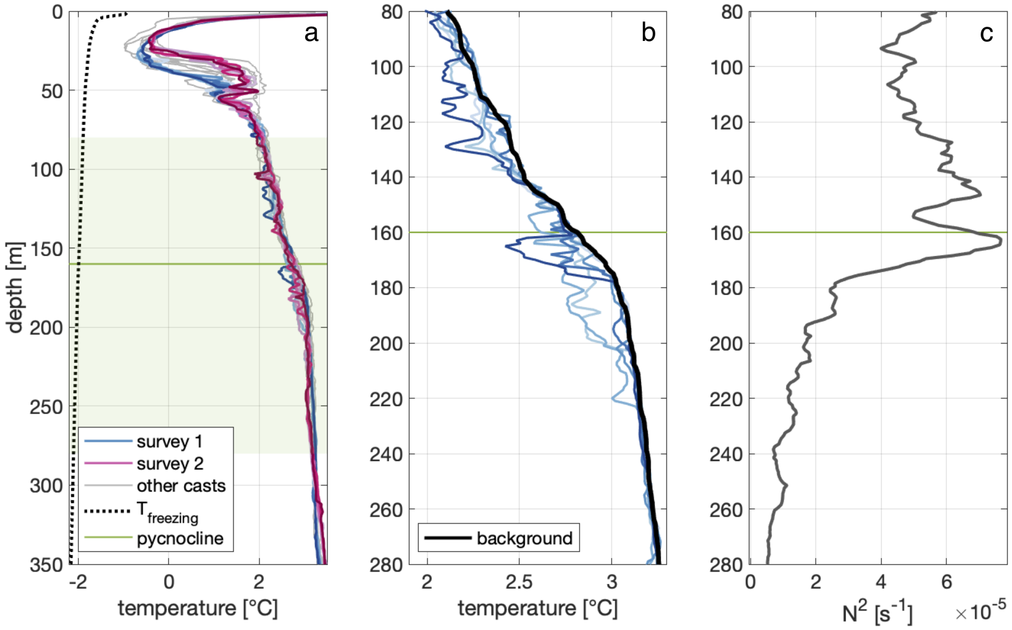

Figure 4.3. (a) Conservative Temperature profiles for both iceberg surveys (survey 1 in blue, survey 2 in pink; different shades are used for each cast to allow for comparison to Figures 4.4-4.6). Profiles from other locations measured in between the two surveys, used to estimate the ambient temperature profile, are plotted in grey. The salinity- and depth-dependent freezing temperature is plotted as a black dotted line. The top of the pycnocline at 160 m, which is used to separate shallow and deep intrusions, is indicated in green on all subplots. The shading indicates the vertical scale of plots (b-c). (b) Temperature profiles from survey 1 plotted with the estimated ambient temperature profile (black). (c) Profile of ambient buoyancy frequency N^2.

methods for a more in-depth discussion.

Because the anomalies of interest in this setting are on the same order of magnitude as other types of variability among profiles, and we are interested in cold anomalies, we construct a conservative estimate of the ambient temperature profile by taking the minimum value among the reference profiles along each isopycnal. If that value is higher than all of the survey temperatures at that density, we instead take the maximum temperature from the survey as the background value. The resulting profile is then low-pass filtered in depth space to generate the estimated ambient temperature for the anomaly calculations (Figure 4.3b). We do this separately for each of the two surveys.

We define intrusions as cold anomalies of at least −0.02°C over a minimum vertical thickness of 3 m, with a peak temperature anomaly of at least −0.04°C. We limit this analysis to the depth range 80-220 m, where $\frac{\partial \theta}{\partial S}$ can be approximated as linear (Figure 4.4).

Assuming that the observed intrusions are the product of the iceberg melting into the ambient water column, we can calculate the average properties of the entrained ambient waters and the meltwater concentration for a point p. We define the melt mixing line that passes through the properties at p (S_p, θ_p) and the effective meltwater properties ($S_m = 0$ kg m$^{-3}, \theta_m = -87$°C, which accounts for cooling due to latent heat uptake; see Section 2.1) and calculate where it intersects the ambient profile (S_a, θ_a). The melt fraction X_m at p is then calculated as

$$X_m = \frac{\theta_a - \theta_p}{\theta_a - \theta_m}, \tag{4.1}$$

which corresponds to distance along the melt line. Two examples of the application of this approach to intrusions in CTD cast 42 are shown in Figure 4.4b. Approximating that entrainment of ambient waters is constant over the vertical extent of the melt plume, the vertical offset between the observed peak and the average ambient, d, represents half of the plume height, $D \approx 2d$.

We calculate composites for the full set of observed intrusions and for intrusions above and below the pycnocline, by rescaling the intrusion depths as

$$z_{scaled} = (z - z_{\Delta T_{max}})\frac{\bar{h}}{h}, \tag{4.2}$$

where $z_{\Delta T_{max}}$ is the depth of the peak anomaly, h is the intrusion thickness (vertical distance between the top and bottom of the observed anomaly as defined above), and $\bar{h}$ is the mean thickness of all intrusions, and then averaging the properties of the rescaled intrusions.

4.3.3 Melt plume model

Line plume simulations

Following Jackson et al. (2020), we use melt plume simulations in the interpretation of our observations. The melt plume model combines buoyant plume theory (BPT) and the three-equation melt parameterization, and is commonly used to simulate entrainment and terminus melt driven by fresh melt runoff that is discharged at the grounding lines of marine terminating glaciers (e.g. Jenkins, 2011; Cowton et al., 2015; Slater et al., 2016), but we expect that the same dynamics apply to ambient melting absent an initial buoyancy input (e.g. Wells and Worster, 2008; Magorrian and Wells, 2016).

For a vertical line plume geometry, the conservation equations for fluxes of volume, momentum, heat, and salt, respectively, are:

$$\frac{d}{dz}(bw) = \alpha w + \dot{m}, \tag{4.3a}$$

$$\frac{d}{dz}(bw^2) = bg'_p - C_D w^2, \tag{4.3b}$$

$$\frac{d}{dz}(bwT) = \alpha w T_a + \dot{m} T_b - C_D^{1/2} w \Gamma_T (T - T_b), \text{ and} \tag{4.3c}$$

$$\frac{d}{dz}(bwS) = \alpha w S_a + \dot{m} S_b - C_D^{1/2} w \Gamma_S (S - S_b), \tag{4.3d}$$

where the plume variables are vertical velocity w, thickness b, temperature T, and salinity S; α is the entrainment coefficient; $\dot{m}$ is melt rate; g'_p is reduced gravity of the plume; C_D is the drag coefficient; ambient temperature and salinity are T_a and S_a, respectively; ice-ocean interface temperature and salinity are T_b and S_b; and Γ_T and Γ_S are the turbulent transfer coefficients of heat and salt. (This set of equations is the same as Equations 2.3a-d, with the slope factor omitted and the replacement of along-slope distance l and velocity u by z and w.)

The boundary layer properties and melt rate are defined by coupling to the three-equation melt formulation (Holland and Jenkins, 1999), which dictates that heat and salt are conserved, and that the temperature at the ice-ocean boundary remains at the pressure- and salinity-dependent freezing point:

$$\dot{m}[c_i(T_b - T_i) + L] = c_w C_D^{1/2} \Gamma_T w (T - T_b), \tag{4.4a}$$

$$\dot{m} S_b = C_D^{1/2} \Gamma_S w (S - S_b), \text{ and} \tag{4.4b}$$

$$T_b = \lambda_1 S_b + \lambda_2 + \lambda_3 (h - z), \tag{4.4c}$$

where c_i and c_w are the heat capacities of ice and water; T_i is the ice temperature; and λ_n are empirical coefficients in the liquidus equation. (This set of equations is the same as Equations 2.2a-c.) While the values of λ_n are well established, the other empirical coefficients, C_D, Γ_T, Γ_S, and α, remain poorly constrained. In our simulations we use the full set of equations 4.3 and 4.4, but in the text we refer to a linearized version of Equation 4.4a,

$$\dot{m} = \frac{c_w C_D^{1/2} \Gamma_T}{L} w T_D, \tag{4.5}$$

substituting the definition of thermal driving $T_D = T_a - T_m$, where T_m is the local freezing temperature, and $T_b = T_m$ by construction (Equation 4.4c), and approximating $T \sim T_a$.

Recent studies of LeConte Glacier suggest that the commonly-used coefficient values may substantially underestimate submarine melt rates (Sutherland et al., 2019; Jackson et al., 2020). Jackson et al. (2020) suggest an adjusted set of coefficient values that better fit their observations. We compare results of simulations using each set of parameter values, which are listed in Table 4.2.

Model scaling estimates

Magorrian and Wells (2016) derive a reduced melt plume model, which predicts that the upwelling scale of melt plumes is proportional to the inverse of the ambient buoyancy frequency (see their Section 4.3 and Eq. 37). Using their Equations 2, 17, 30, and 37, and the definition of X_{neut} in their Section 4.3, we arrive at the following estimate of plume height D:

$$D_{MW16} = K_n \Delta\rho \frac{M}{E} \left| \frac{\partial \rho_a}{\partial z} \right|^{-1}, \tag{4.6}$$

where $K_n = 2.46$ is an empirical constant arising from the dynamics of the scaled model, $\Delta\rho$ is the density difference between meltwater and the ambient, M and E are dimensionless factors relating the melt and entrainment rates to velocity, and $\frac{\partial \rho_a}{\partial z}$ is the ambient vertical density gradient. M and E are defined such that melt rate $\dot{m} = Mw$ and entrainment rate $\dot{e} = Ew$. Thus E is a constant analogous to α in Equation 4.3a, while the value of M is dependent on thermal driving T_D the drag and transfer coefficients C_D and $\Gamma_{T,S}$ (Equation 4.5).

For ambient melting, which does not have an initial freshwater input, we expect the melt concentration in the plume X_m to be equivalent to $\frac{M}{M+E}$. For $M \ll E$ we approximate that $\frac{M}{E} = X_m$. Substituting the definitions of buoyancy frequency $N^2 = \frac{g}{\rho_0}\frac{\partial \rho}{\partial z}$ and reduced gravity $g' = \frac{g\Delta\rho}{\rho_0}$, we rewrite Equation 4.6 as

$$D_{MW16} = K_n \frac{g'}{N^2} X_m, \tag{4.7}$$

which predicts the plume height D in terms of familiar quantities that can be readily calculated from our observations.

4.4 Results

4.4.1 Observations of cold, fresh anomalies

The ambient temperature and salinity profiles observed during the iceberg surveys are typical of the summer fjord structure, with warm salty Atlantic Water (AW) at depth overlain by cooler fresher glacially modified waters (GMW) and a relatively warm fresh surface layer in the upper 30 m (Figures 4.3a and 4.4). There is a permanent pycnocline at about 160-180 m depth, which is visible as a peak in stratification in Figure 4.3c. The AW layer below the pycnocline has low stratification relative to the GMW above.

In all 11 CTD profiles from the two iceberg surveys, cold fresh anomalies of up to -0.4° and 0.05 g/kg are observed along isopycnals, especially between 50 m and 220 m (Figure 4.3a-b). We refer to these anomalies as melt intrusions, which we justify further in Section 4.4.2. The intrusion characteristics reported in this and the following section are summarized in Table 4.2.

Based on the criteria in Section 4.3.2, we identify a total of 66 intrusions among the 11 profiles, with 39 below the 160 m pycnocline ("deep") and 27 above the pycnocline ("shallow"). The mean intrusion thickness h (i.e. the vertical extent of the observed anomaly) is 11 ± 1 m, and is not significantly different below (12 ± 1 m) and above (10 ± 1 m) the pycnocline. The mean peak temperature anomaly is -0.14 ± 0.01°C, with deep intrusions averaging -0.17 ± 0.02°C and shallow intrusions averaging -0.12 ± 0.01°C (Figure 4.5b).

4.4.2 Plume height and melt concentration for observed intrusions

In T-S space, these anomalies are consistent with expected properties of iceberg melt originating deeper in the water column, supporting the notion that these anomalies

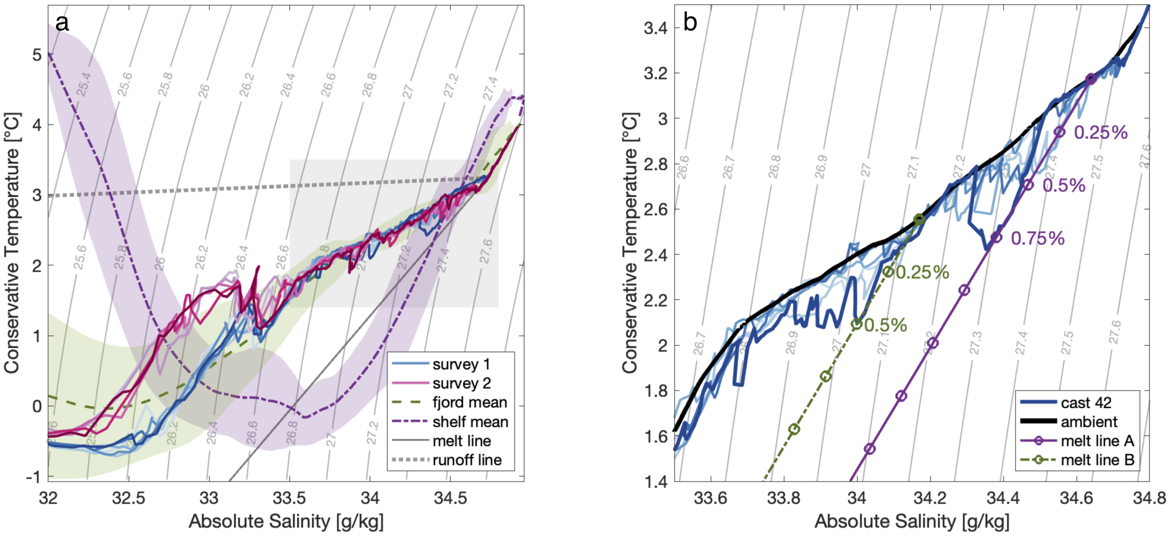

Figure 4.4. (a) Temperature-salinity plot for iceberg surveys 1 (blue lines) and 2 (pink lines). Also shown are mean T-S profiles for the fjord (green dashed line) and shelf (purple dot-dash line), with shading indicating the standard deviation. A melt line (solid grey line) and runoff line (dotted grey line) are plotted for the fjord profiles. Grey shading indicates region shown in (b). (b) Zoom in on T-S plots for survey 1 (blue lines), highlighting cast 42 (thick dark blue line). The ambient T-S profile is plotted as a solid black line. Two melt lines are plotted with circles indicating the corresponding melt concentration in increments of 0.25% as an example of the melt fraction calculation method (Section 4.3.2). In both plots density contours (σ_0) are plotted in grey, with interval 0.2 kg m^{-3} in (a) and 0.1 kg m^{-3} in (b). The density range shown in (b) corresponds to approximately 60-400 m depth for these profiles.

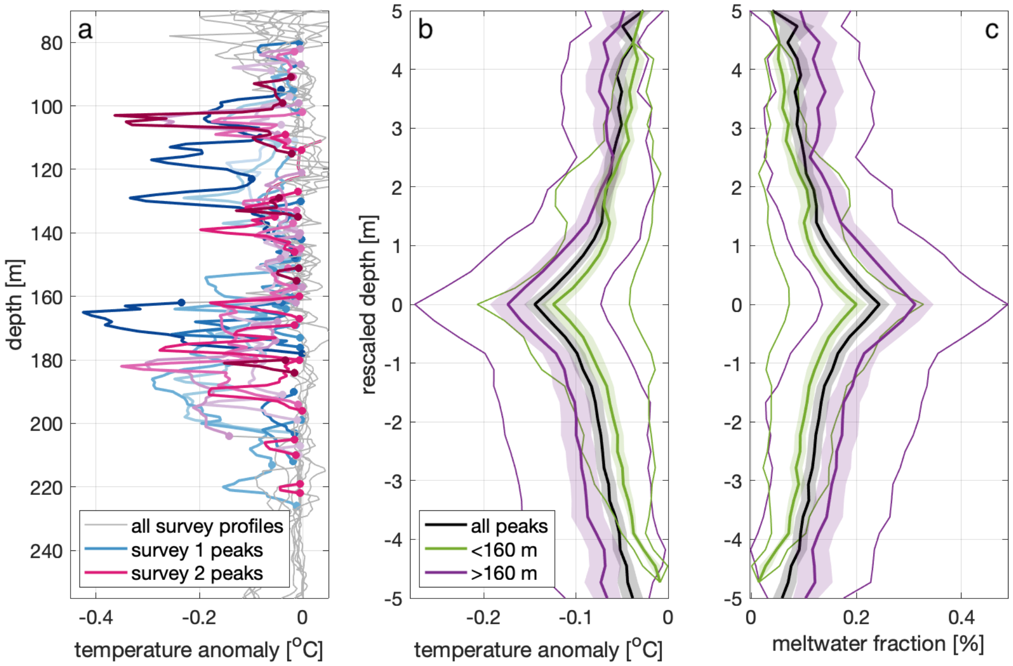

Figure 4.5. (a) Profiles of temperature anomaly relative to the ambient for both iceberg surveys (thin grey lines). Identified intrusions plotted for surveys 1 (blue lines) and 2 (pink lines). (b) Composites of temperature anomaly and (c) composites of meltwater fraction for all identified peaks (black line), shallow peaks (above 160 m, green line), and deep peaks (below 160 m, purple line). Shading indicates the standard error of the mean and thin lines show one standard deviation from the mean for each quantity. Depths are rescaled relative to the mean intrusion thickness as described in Section 4.3.2.

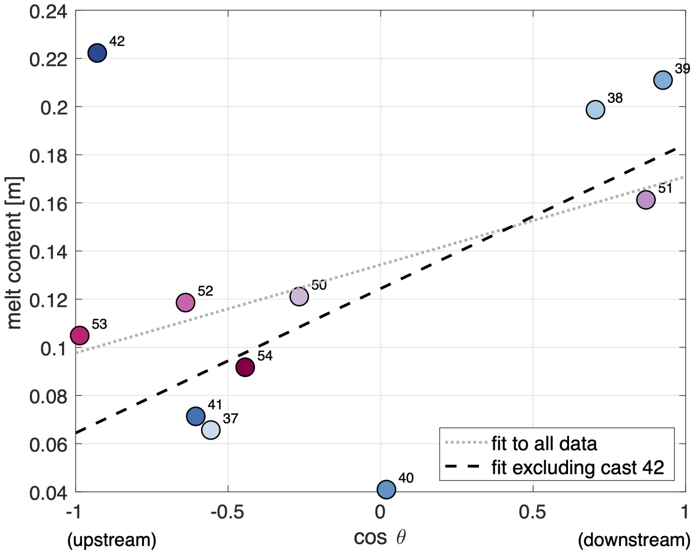

Figure 4.6. Integrated melt content for each profile in iceberg surveys 1 (blue circles) and 2 (pink circles) vs. cos θ ("wakeness"), where θ is the angle between the profile location and iceberg drift direction at the time of the profile, and cos $\theta = 1$ corresponds to a cast taken directly downstream of the inferred iceberg wake. Points are labeled by cast number. Best fit lines are shown for all profiles (dotted line), and excluding cast 42 (dashed line).

are iceberg melt plume intrusions (Figure 4.4). Under this assumption, we calculate the meltwater content of the intrusions and vertical extents of the corresponding melt plumes by the method described in Section 4.3.2 (Jackson et al., 2020). These results are also summarized in Table 4.2.

The mean meltwater concentration X_m of all intrusions is 0.24 ± 0.02%, while deep intrusions are on average 0.31 ± 0.04% meltwater and shallow intrusions average 0.20 ± 0.02% (Figure 4.5c). The average plume height D (i.e. plume upwelling distance before intruding at neutral buoyancy) for all intrusions is 30 ± 4 m. The deep intrusions had upwelled an average of 53 ± 2 m and shallow intrusions an average of 14 ± 2 m. In summary, intrusions below the pycnocline on average contained more meltwater and had risen over a greater vertical distance than intrusions above the pycnocline.

In addition to the vertical distribution of melt, we consider the spatial pattern in order to more confidently attribute the observed melt to the surveyed iceberg. By integrating the intrusion meltwater fraction over the observed depth range for each profile, we find a mean meltwater content (per unit area) of 0.13 m with a standard deviation of 0.06 m (Figure 4.1b). Melt content was not significantly correlated with distance from the iceberg edge ($R^2 = 0.27, p = 0.09$; Table 4.1). This suggests that the survey CTD casts were generally sufficiently close to the iceberg to capture its melt signal, if indeed the observed meltwater is from this iceberg.

Assuming there is some meltwater wake associated with the iceberg drift, we define a "wakeness" factor cos θ where θ is the angle between the profile location and the mean iceberg drift direction during that CTD cast, such that profiles directly behind the iceberg (downstream of the wake) have a value of 1 and profiles directly ahead of the iceberg (upstream of the wake) have a value of -1. 54% of the melt content variability can be explained by this metric, with the exception of one profile that was measured as the drift was reversing ($p = 0.02$; Figure 4.6; see Appendix 4A for more details about the iceberg drift during the survey period). This relationship provides further evidence that the observed meltwater intrusions originated from the surveyed iceberg.

4.4.3 Melt plume model simulations with observed profiles

We use the ambient T-S profile constructed from observations as input to a line plume model using standard parameter values and the adjusted parameter values proposed by Jackson et al. (2020), which we refer to as J20 parameters. Both sets of values are listed in Table 4.2. The simulations were run over a depth range of 80-280 m, between the upper bound and the deepest source depth in the observational analysis, to facilitate comparison between the observations and model results.

Above the pycnocline, the plume height (i.e. upwelling distance) in the standard simulation was 4 ± 1 m, significantly lower than the observed average of 14 ± 2 m (Figure 4.7b, purple). Using the J20 parameters increases the shallow plume height to 13 ± 2 m (Figure 4.7b, green). Below the pycnocline, the standard coefficient values resulted in a

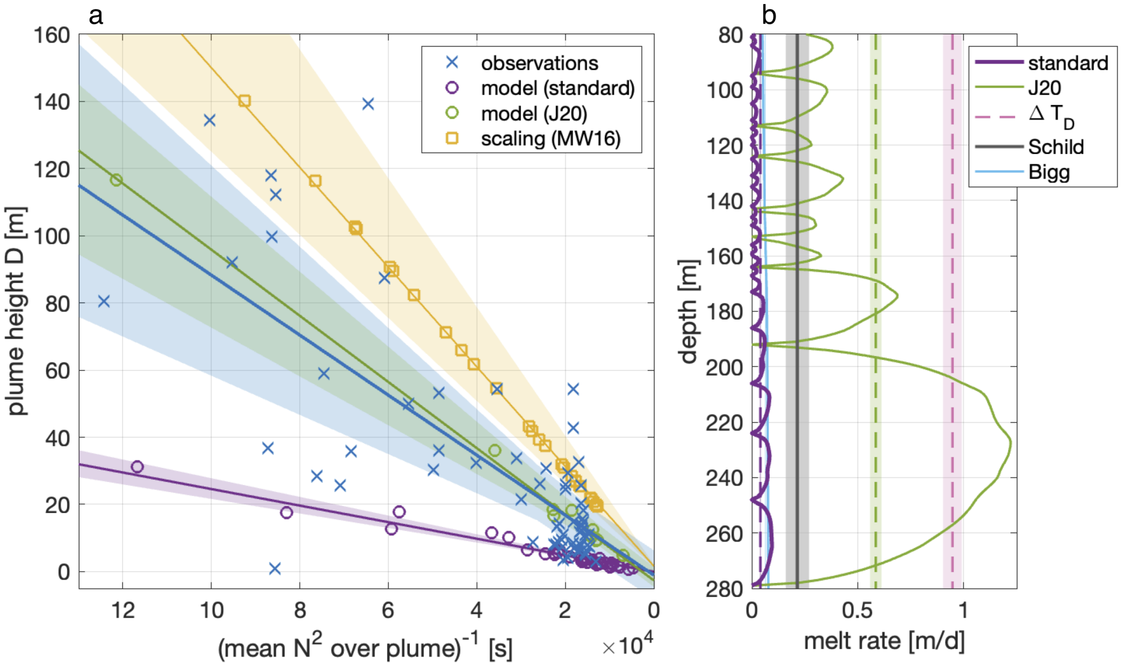

Figure 4.7. (a) Plume height D vs the inverse of buoyancy frequency N^{-2} averaged over each cell, plotted from the survey observations (blue crosses), standard plume model (purple circles), adjusted J20 plume model (green circles), and scaling (Magorrian and Wells, 2016, yellow squares). The x-axis is reversed so that lower stratification values fall to the left. Solid lines are linear fits to the data with shading indicating the bootstrap 95% confidence interval (except for on the scaling estimate, where the shading reflects the range of observed values of X_m). (b) Profiles of melt rate vs depth for plume model simulations with standard parameters (purple) and J20 parameters (green). Dashed lines are the depth-averaged melt rate for each of those simulations and for the simulation with adjusted thermal driving (pink). The melt rate parameterization from Bigg et al. (1997, light blue) and a 2017 observational estimate from Schild et al. (2021, grey) are plotted for comparison.

plume height of 15 ± 4, while the J20 simulation yielded 53 ± 29. The latter error estimate is large because the model simulates only two plumes below the pycnocline.

Magorrian and Wells (2016, MW16) predict that plume height is proportional to the inverse of the buoyancy frequency (Equation 4.7). We find that there is a significant correlation between the observed D and mean N^{-2} over the plume for our observed intrusions ($y = 8.9 \times 10^{-4}x - 1.1, R^2 = 0.56, p < 10^{-5}$; Figure 4.7a, blue). We find the same relationship in the plume model using the J20 parameter values ($y = 9.9 \times 10^{-4}x - 2.6, R^2 = 0.99, p < 10^{-5}$), which agrees with the observed fit within uncertainty (Figure 4.7a, green). The standard plume model (purple) reproduces this dependence but with a significantly smaller effect ($y = 2.5 \times 10^{-4}x - 0.1, R^2 = 0.98, p < 10^{-5}$).

However, while the plume model with the J20 parameters recreates D well for the Sermilik observations, the corresponding prediction of melt concentration is much lower than the value derived from observations (Table 4.2). We find that various additional adjustments to the coefficients can recreate observed X_m, but the corresponding estimates of D are far above observed values.

We also calculate D as predicted by Equation 4.7 using the X_m values derived from the observations (Table 4.2). The yellow squares in Figure 4.7a were calculated using the overall mean X_m, and the confidence intervals were calculated using the shallow and deep means. We find that the scaling significantly overestimates the plume height for observed melt concentrations.

To summarize, although the plume simulation using the adjusted J20 parameter values predicts the observed plume height D well, the modeled melt fraction X_m remains significantly lower than observed values for both the shallow and deep intrusions (Table 4.2). In contrast, Jackson et al. (2020) find that a number of possible adjustments to the coefficients produce values of both D and X_m that are consistent with the observations from LeConte.

4.4.4 Idealized simulations of plume height and melt concentration

We rearrange Equation 4.7 to express the relationship between D and X_m as represented in the melt plume model as

$$\frac{X_m}{D} = K_n \frac{N^2}{g'}. \tag{4.8}$$

The coefficient $K_n = 2.46$ is empirically calculated using the scaled form of the melt plume model and arises from its underlying physics, independent of C_D and $\Gamma_{T,S}$ (Magorrian and Wells, 2016). N^2 is simply the ambient stratification. The reduced gravity g' for the ambient relative to meltwater depends on the ambient density, locally approximated as $\rho_a(T_a, S_a) = \rho_m[1 + \beta_S(S_a - S_m) - \beta_T(T_a - T_m)]$, where β_S and β_T are empirical saline contraction and thermal expansion coefficients, respectively. Using $S_m = 0$ and thermal driving $T_D = T_a - T_m$ allows us to rewrite g' as

$$g' = g\big(\beta_S S_a - \beta_T T_D\big), \tag{4.9}$$

showing that g' decreases as T_D increases. Thus, in the melt plume parameterization, there is a fixed relationship between X_m and D that depends only on the ambient stratification and thermal driving, independent of the transfer, drag, and entrainment coefficient values.

We illustrate this relationship by running a suite of plume model simulations with idealized ambient temperature and salinity profiles (with constant thermal forcing and density gradient) to probe the dependence of X_m and D on T_D and N^2 in the range of values observed in Sermilik and LeConte. Results using the J20 model coefficients are shown in Figure 4.8, but we find that the relationship holds using the standard values (Figure 4B), as predicted by Equation 4.8.

As predicted by Equation 4.7, our experiment shows that stratification is the primary control on plume height in the model, though there is a weak dependence on thermal driving, i.e. for very low T_D, melting is too weak to initiate upwelling plumes (Figure 4.8a). The ratio of melt to entrainment is controlled by thermal driving, independent of N^2 (Figure 4.8b). This can also be shown by substituting $\dot{e} = \alpha w$ (from Equation 4.3a) into Equation 4.5, yielding

$$X_m = \frac{c_w C_D^{1/2} \Gamma_T}{\alpha L} T_D, \tag{4.10}$$

again using the approximation $\frac{M}{E} \approx X_m$. The resulting relationship between X_m and D has a weak dependence on thermal driving for small N^2 that increases with stratification (Figure 4.8c).

We plot observed values for N^2, T_D, and $\frac{X_m}{D}$ from the Sermilik iceberg surveys (deep and shallow composites; black outlined circles) and LeConte (white outlined circles) over the simulated values on each panel in Figure 4.8, though we note that their locations in the parameter space are approximate because the observed profiles have vertical variation in stratification and thermal driving. In the LeConte study, the J20 coefficient values were used in combination with a horizontal velocity of 20 cm s^{-1} to recreate the observations. Accordingly, both D and X_m are underestimated by the model relative to the LeConte observations (Figure 4.8a-b), but the ratio in Figure 4.8c agrees well. The idealized simulations closely match the Sermilik observations in for D, but predict a lower X_m and thus appear to underestimate the ratio.

4.4.5 Coupling of melt parameterization to the plume model

This result raises the question of why the plume model is unable to recreate the iceberg melt intrusions observed in Sermilik Fjord, in contrast to the LeConte observations. There are a number of differences among the two settings that may be significant here, including the different geometries: the idealized vertical wall setup used for the plume simulations in both studies is likely better suited to a tidewater glacier terminus than to

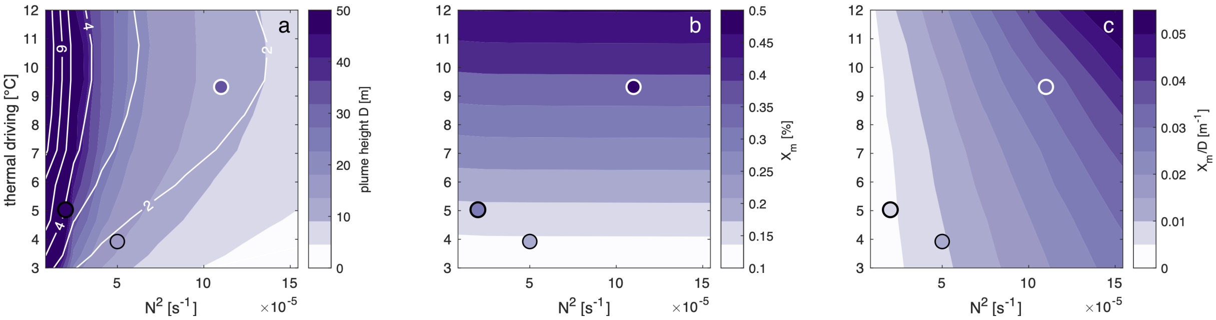

Figure 4.8. Results from plume model simulations over a range of values for stratification N^2 and thermal driving T_D: (a) Plume height D (filled contours) and vertical velocity w (white contour lines, in units of cm s^{-1}). (b) Meltwater concentration X_m. (c) The associated slope $\frac{X_m}{D}$. Estimated observational values from Sermilik iceberg surveys (deep and shallow composites; black outlined circles) and LeConte (white outlined circle). These plots show the results for the model with J20 parameter values; the same calculations with the standard parameters are shown in Appendix B (Figure 4B).

an iceberg. However, varying the slope is not an obvious solution as it introduces a factor of cos ϕ, where ϕ is the angle from the vertical, into the plume equations, which feeds back on the melt rate (see Chapter 2, Equations 2.2-2.3).

Figure 4.8 also highlights that LeConte Bay is warmer and more stratified than the observed region of Sermilik Fjord. We consider the significance of the ratio $\frac{X_m}{D}$ and how it is related to those properties in the model to gain further insight into the physics underlying the mismatch between the Sermilik observations and simulations.

An established weakness in the melt parameterization (Equations 4.4a-c) is its underlying assumption of a shear-controlled boundary layer structure, which is violated at some critical velocity w_c, below which melt rate is independent of velocity (discussed in detail in Section 4.5.1; Wells and Worster, 2008; McConnochie and Kerr, 2017). The plume model (Equations 4.3a-d) contains this assumption only through its coupling to the melt equations.

X_m is proportional to T_D and is defined to be explicitly independent of w (Equation 4.10). Through some manipulations of the Magorrian and Wells (2016) model, we show in Appendix 4C.1 that w is proportional to plume height D. Thus $\frac{X_m}{D}$ may be interpreted as an expression of how the model physics predict that melt rate and velocity should be related for a given thermal driving.

Though we do not have velocity observations from the iceberg surveys, we can estimate the vertical plume velocity from the simulations (Table 4.2). While N^2 is dominant in determining this value, Figure 4.8a shows that both w and D are reduced at low T_D relative to warmer simulations with the same N^2. Both sets of iceberg intrusions fall near the lower lefthand corner of the parameter space, where T_D may be a limiting factor on w and D.

Therefore, one possible explanation for the mismatch between observed and simulated $\frac{X_m}{D}$ is that the plume model using the adjusted coefficients from J20 is appropriately simulating D and thus w, but still underestimating the melt rate because w is below the critical threshold. If this is the case, a different melt parameterization better suited to the underlying physics is needed. For now, we consider the effects of various adjustments to the existing melt equations on the plume model to understand how the ratio $\frac{X_m}{D}$ is determined in the current model.

First, we show in Appendix 4C.2 that any increase to the coefficients in the melt rate Equation 4.4a also multiplies the first term in the plume momentum Equation 4.3b. Intuitively, this occurs because the additional meltwater input increases plume buoyancy, which feeds back on the melt rate through w, allowing the plume to gain more momentum and rise further before reaching neutral buoyancy. This straightforward relationship is the basis of $\frac{X_m}{D}$.

In contrast, we show in Appendix 4C.2 that for uniform thermal driving, multiplying T_D by a constant affects X_m and D differently due to nonlinear dependence of Equation 4.3b on T_D. This works because while adding freshwater to the plume decreases its density, as in the previous case, here the ambient density is also decreased by the increase in temperature. This has a moderating effect on the density difference and thus the change in plume buoyancy. However, for variable thermal driving, we show that multiplication of

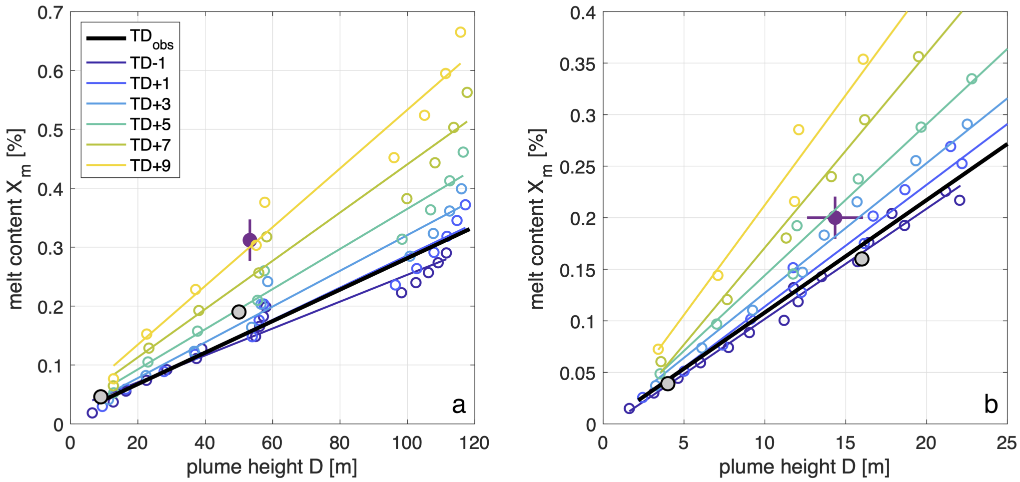

Figure 4.9. Melt fraction X_m vs plume height D for observed (a) deep and (b) shallow melt intrusions (purple circle) and simulated value using standard and J20 model parameters (grey circles). The thick black line shows the range of simulated values for the observed profile resulting from multiplying $\Gamma_{T,S}$ by a factor ranging from 0.5-8. Each colored line represents simulations with the thermal driving profile shifted by ΔT_D as indicated in the legend, with colored circles representing the mean result for each value of $\Gamma_{T,S}$.

T_D has a compensating effect on ambient stratification (Appendix 4C.3). Instead, adding a constant to T_D preserves the stratification while increasing X_m by shifting the mean.

Granting that artificially "warming" the ambient temperature profile to increase the modeled melt rate is not a physically satisfying solution, we propose that it may functionally amend a mismatched assumption in the melt parameterization about the relationship between melt rate and velocity in a low thermal driving, low velocity context such as the Sermilik iceberg surveys. In the following section, we apply this finding to force the model to reproduce the Sermilik observations in order to highlight some of the resulting uncertainties, but we emphasize that the underlying physics are certainly incorrect. If indeed the existing melt plume model is misrepresenting the iceberg melt plumes, more fundamental modifications are needed to resolve that issue.

4.4.6 Adjusted melt plume model simulations

To illustrate the effect of varying the plume model coefficients, we first run a set of simulations with the observed profiles for both the deep and shallow layers in Sermilik, using a range of coefficient values. The black lines in Figure 4.9a-b show the range of X_m vs. D resulting from multiplying $\Gamma_{T,S}$ by a factor ranging from 0.5-8. (We also tested the effect of varying C_D and confirmed that it did not change the slope of this line, as predicted in Section 4.4.5, so we vary only $\Gamma_{T,S}$ for simplicity.) In both cases, the observed mean X_m is significantly higher than predicted by the model at the observed plume height; this is analogous to the results from the J20 simulation (Table 4.2).

We then shift the thermal driving by adding a constant ΔT_D between -1 and 10°C to each temperature profile and run simulations for the same range of $\Gamma_{T,S}$. The resulting values are plotted as circles in Figure 4.9a-b, with a best fit line for each value of ΔT_D. Generally, the slope $\frac{X_m}{D}$ increases with ΔT_D in these cases, although there is variation around the best fit line. In Figure 4.9a, there is a gap between plume heights of 50 m and 90 m, which correspond to depths of 230 m and 190 m for plumes originating at 280 m. Figure 4.3c shows increases in stratification around both of those depths, suggesting that the vertical variability in density gradient is a likely reason for departures from the best-fit line.

For the deep intrusions, the best fit slope suggests that $\Delta T_{D,deep} = 8°\text{C}$ is required to recreate the observed values of X_m and D, while for the shallow intrusions $\Delta T_{D,shal} = 3°\text{C}$ is sufficient (Figure 4.9). The difference between the two estimates of ΔT_D is consistent with Figure 4.8c, which shows that the strength of the relationship between T_D and $\frac{X_m}{D}$ increases with stratification. Because the aforementioned variation in stratification near the mean value of the observed deep intrusions affects the slope of the best fit line, we use $\Delta T_{D,deep} = 6°\text{C}$. In both cases, adding the corresponding thermal driving offset and multiplying $\Gamma_{T,S}$ by 2.5 result in a good approximation to both observed X_m and D (Table

4.2).

In summary, for the thermal driving and stratification range in the Sermilik iceberg surveys, the melt plume model does not capture the observed relationship between melt concentration and plume height, which is determined by the ambient stratification and thermal driving, independent of the empirical coefficients in the parameterization (Equation 4.8). In contrast, our simulations and the results of Jackson et al. (2020) show that this relationship holds for LeConte Bay, which has higher thermal driving and stratification (Figure 4.8c). We show mathematically and numerically that the mean thermal driving of the ambient profile determines the simulated relationship between melt concentration and plume height. We demonstrate that adjusting the thermal driving input can force the plume model to recreate the Sermilik observations, but emphasize that this approach is unphysical, suggesting a need for a different melt parameterization.

4.4.7 Model estimates of iceberg melt rate and upwelling

The upwelling velocity w increases by about a factor of 3 between the standard and J20 parameters, but is not significantly different in the ΔT_D case for either the shallow or deep plumes, indicating that the relationship between D and w is independent of the melt parameterization, as predicted in Section 4.4.5. Even when the model coefficients were increased beyond the J20 values to recreate the observed melt content, the deep plumes were impeded by the pycnocline, reaching neutral buoyancy between 170-180 m (Table 4.2).

In contrast to W and D, the overall mean melt rate is an order of magnitude higher in the J20 simulation than with the standard parameters, and increases by a further 60% when the ΔT_D correction is applied (Figure 4.7b). We hesitate to over-interpret the exact values, given our hypothesis that the model physics are poorly matched to the setting of our observations, but the significant difference in simulated melt rate suggests that resolving this issue is likely to be consequential for modeling of melt rates in similar environments.

4.5 Discussion

4.5.1 Velocity, thermal driving, and the ice-ocean boundary layer

The commonly used three-equation melt plume parameterization is able to accurately represent the characteristics of melt intrusions observed in LeConte Bay, but not of this set of observations from Sermilik Fjord. In contrast to the setting of the iceberg surveys toward the head of Sermilik Fjord, LeConte Bay is relatively warm and energetic (Figure 4.8c; Jackson et al., 2020). Here we consider the relationship between currents, thermal driving, and the structure of the ice-ocean boundary layer, and the implications for the parameterized melt rate.

Within the turbulent upwelling plume, there is a laminar sublayer at the ice-ocean interface over which heat and salt are transferred to the ice primarily through molecular diffusion. The outer boundary layer is relatively well-mixed, such that the temperature and salinity at the outer edge of the sublayer can be well-approximated by plume variables T and S (Jenkins et al., 2010). The heat flux across the boundary layer is thus determined by Fick's law of scalar diffusion,

$$\frac{\partial T_b}{\partial t} = \kappa_T \frac{T_D}{\delta}, \tag{4.11}$$

with molecular heat diffusivity κ_T multiplying the temperature gradient across the sublayer thickness δ. As submarine ice melt is driven by fluxes of heat and salt from the ocean, increasing T_D or decreasing δ should increase the heat flux and thus the melt rate.

The sublayer thickness, in turn, may be controlled either by a shear instability or by a convective instability (McConnochie and Kerr, 2017). For a high velocity plume, the shear exerted on the sublayer is strong and δ is characterized by a Reynolds number,

$$Re_\delta = \frac{w\delta}{\nu}, \tag{4.12}$$

where ν is the kinematic viscosity and and w is velocity, in this case the velocity of the upwelling plume, i.e. $\delta \propto w^{-1}$. The commonly used three-equation melt parameterization (Equation 4.4) implicitly assumes that the laminar sublayer falls into this regime (Wells and Worster, 2008). The resulting dependence of melt rate on w is explicit in Equation 4.5. In the plume model, w is directly related to D (Section 4.4.5). D in turn is primarily determined by stratification, but also depends on thermal driving at low values of N^2 and T_D (Figure 4.8a).

However, the boundary layer in weak plumes with sufficiently low shear may fall into the convective instability regime, in which δ is instead characterized by a Rayleigh number,

$$Ra_\delta = g'\frac{\delta^3}{\kappa\nu}, \tag{4.13}$$

where κ is molecular diffusivity, i.e. $\delta \propto g'^{-1/3}$. g' is inversely related to T_D (Equation 4.9), so in this regime we would expect δ be directly related to T_D (with a relatively weak dependence due to the exponent). Because $\kappa_T \gg \kappa_S$, there will be two distinct sublayers in this regime, with δ_T and δ_S each dependent on its respective molecular diffusivity.

Theory and experimental results indicate that the transition from convection to shear control occurs when a compositional Rayleigh number Ra_c, with the length scale set by distance from the plume base, reaches a critical value of $10^{16} - 10^{21}$ (Wells and Worster, 2008; Kerr and McConnochie, 2015). McConnochie and Kerr (2017) estimate that the corresponding critical velocity w_c is likely to fall in the range of 2-6 cm s^{-1} in an experimental setting.

Given that LeConte has both relatively high thermal driving and ambient currents estimated at roughly 20 cm s^{-1} (Jackson et al., 2020), we expect it to fall into the shear-driven regime, which is consistent with the underlying assumptions of the plume model. In contrast, the largest iceberg melt plume velocities predicted by the model below the pycnocline are about 5 cm s^{-1} (Table 4.2), which could plausibly fall below the critical w_c needed to transition from the convection to the shear regime (McConnochie and Kerr, 2017). Thus we hypothesize that the disagreement between the iceberg plume observations and simulations could reflect a violation of the assumption of a shear-controlled boundary layer.

It is important to note that the value of δ must not necessarily be smaller in the convective regime than in the shear regime in contexts where it is applicable. Two recent studies of basal melt of Antarctic ice shelves suggest that in that setting, the shear-based parameterization is likely to overestimate the melt rate (Rosevear et al., 2021a,b), while here we argue that the melt rate in Sermilik Fjord may be underestimated by the parameterization. One important distinction is that Rosevear et al. (2021b) estimate typical ocean currents at the base of Amery Ice Shelf at around 10 cm s^{-1}, greater than the simulated plume velocities in Sermilik Fjord by a factor of 2-5 (Table 4.2). Those background current velocities are determined by factors that are independent of temperature (e.g. tides and larger-scale ice shelf cavity circulation). The two settings also differ in geometry and thermal driving: the basal slope at Amery is estimated at 81° from the vertical and the temperature is approximately 0.2°C above freezing, in contrast to our iceberg simulations where we assume a vertical ice face and observed T_D is between $4-5$°C.

Both sets of Sermilik iceberg plume observations fall in the region of Figure 4.8a where plume height and, relatedly, upwelling velocity decrease with T_D. In the shear regime, this relationship amplifies the effect of decreasing T_D on the temperature gradient across the sublayer, $\frac{\Delta T}{\delta}$, by (1) directly decreasing ΔT and (2) indirectly weakening w, which Re_δ predicts will thicken the boundary layer, increasing the denominator. In the convective regime, δ is smallest for low T_D, which should have a small moderating effect on the change in temperature gradient, reducing the dependence of heat flux, and thus melt rate, on T_D. Our approach of adjusting T_D (Section 4.4.6) in effect counteracts potential inflation of the denominator in $\frac{\Delta T}{\delta}$ by "correcting" the numerator proportionally.

Therefore, if the Sermilik observations are indeed from a convection-controlled boundary layer regime, it is possible that the melt parameterization implicitly overestimates δ and thus underestimates the melt rate. This is consistent with our finding that the plume model coupled to a shear-based melt parameterization underestimates the melt rate relative to the upwelling velocity, and with the form of the adjustment to T_D used to reproduce the observations.

4.5.2 Prevalence of attached iceberg melt plumes

The melt intrusions described here are analogous to the attached melt plumes observed by FitzMaurice et al. (2017) on ice blocks in a flume with a low background velocity. For attached plumes, they show that meltwater rises along the sides of the iceberg, spreading both upstream and downstream of the ice block in the surface layer. In higher ambient flow experiments, the meltwater separates from the face of the ice block and is distributed throughout the water column downstream of the ice block. We found evidence of melt intrusions in all of the profiles from both surveys, which are distributed around the iceberg (Figure 4.1), indicating that the intruding plumes spread radially around the iceberg rather than being swept downstream.

FitzMaurice et al. (2017) hypothesize that this behavior occurs when the vertical plume velocity w is greater than the relative horizontal velocity between the iceberg and ocean. In observations of ocean currents and drift velocities of 90 icebergs in Sermilik Fjord, they estimate that 40% of the icebergs fall into this attached plume category.

Jackson and Straneo (2016) find that the highest mean exchange flow speed below 200 m is about 4 cm s^{-1} (one standard deviation above the mean at 300 m; see their Figure

13a), and that during summer, the fluctuating residual velocity is of a similar magnitude. This suggests that the maximum sustained velocity below the pycnocline during summer is likely to be roughly 8 cm s^{-1} (i.e. when the fluctuating term is in the same direction as the mean and both are at a maximum) and that the majority of the time and over the majority of this layer the velocity is likely lower. Based on the J20 vertical velocity estimate, this suggests that iceberg melt plumes likely are typically attached over much of the AW layer, while above the pycnocline, where upwelling velocities are higher and fjord velocity is higher and more variable, they may more commonly be detached (FitzMaurice et al., 2017). Thus the mechanism for iceberg melt-driven upwelling described here is likely to be applicable to other deep icebergs with keel depths within the AW layer. If so, this process, which has not been directly included in fjord-scale modeling studies (Davison et al., 2020, 2022), could contribute significantly to AW circulation. However, it is worth noting that even simulated plumes with unrealistically high momentum did not penetrate past the pycnocline, suggesting that it may pose a significant barrier to transport of heat and nutrients from the AW layer into the upper water column.

4.5.3 Iceberg-driven overturning

Davison et al. (2020) find that including icebergs in simulations of Sermilik Fjord increases up-fjord currents below the pycnocline by over 30% relative to the runoff-driven circulation. The increase in AW velocity contributes to a 70% increase in subsurface heat flux toward the glacier under summer conditions, and is the dominant driver of circulation in simulations without runoff. Their model does not directly simulate melt-driven upwelling plumes, which would be much more computationally intensive.

We present observational evidence that stratification controls the vertical extent of melt-driven upwelling as predicted by theory and numerical simulations (Magorrian and Wells, 2016). Plume height is directly proportional to vertical velocity and thus to entrainment rate (Section 4.4.5; Equation 4.3a). Like Jackson et al. (2020), we find that the plume model with standard parameters underestimates plume height relative to our observations, while simulations with the J20 modifications to transfer and drag coefficients agree more closely with our observational estimates (Figure 4.7a). The vertical velocities in the J20 simulations, on average 4.9 ± 0.2 m s^{-1} below the pycnocline (Table 4.2), are also more consistent with past estimates of upwelling plume velocity. In a field study of a grounded iceberg in Newfoundland, Josberger and Neshyba (1980) observe an average upwelling velocity of 7 cm s^{-1} over the upper 15-20 m of the water column, which is warmer and more highly stratified on average than the AW layer in our Sermilik Fjord study.

4.5.4 Iceberg melt rates

As described in Section 4.4.7, the model melt rate estimates are very sensitive to the choice of parameters and to the thermal driving adjustment (Table 4.2). We compare the range of our simulated values to other published iceberg melt rate estimates (Figure 4.7b).

El-Tahan et al. (1987) and Bigg et al. (1997) established an empirical estimate of melt rate dependence on thermal forcing based on laboratory experiments. Their formulation,

$$\dot{m} = 7.62 \times 10^{-3} T_D + 1.29 \times 10^{-3} T_D^2, \tag{4.14}$$

where $\dot{m}$ is melt rate in m d^{-1} and T_f is thermal forcing (Moon et al., 2018), gives a mean melt rate of 0.07 ± 0.00 m d^{-1}, within a factor of 2 from the standard plume model estimate (Figure 4.7b).

Schild et al. (2021) use GPS observations of iceberg surface lowering to get mass loss estimates from two icebergs in Sermilik Fjord during summer 2017. They then use multibeam sonar imaging of the subsurface iceberg geometries to estimate the surface area for each iceberg. For their Iceberg A, which had similar geometry to Lars (keel depth

~ 380 m, surface length 730 m), they find melt rates between 0.16-0.27 m d^{-1}, between the standard plume model and J20 estimates (Figure 4.7b). We note that their melt rate is an average over the full iceberg keel, while our estimate is only between 80-280 m, so these values are not directly comparable. Probably more significant is that our simulations of buoyant plumes against a vertical ice wall do not account for the complexity of iceberg geometry, while their melt rate calculation depends heavily on their estimate of iceberg surface area and also neglects spatial variability. Thus it is difficult to compare these estimates directly, but their study indicates a need for caution in scaling up melt plume simulations to estimate iceberg heat and freshwater fluxes.

4.5.5 Moving forward

Our results offer additional evidence that there is a mismatch in ice-ocean boundary layer physics between our observations and the commonly used three-equation melt parameterization with significant consequences for simulated melt rates (McConnochie and Kerr, 2017; Rosevear et al., 2021a,b). We show that an adjustment to the input profiles can force the model to reproduce our observations, but this approach is unphysical, casting doubt on the results of those simulations. There are multiple potential explanations for the apparent mismatch between the Sermilik observations and the existing model, including the assumption of a shear-controlled boundary layer, as well as factors such as iceberg geometry. Here we have focused on the boundary layer parameterization, but each of these possibilities warrants more careful consideration.

The boundary layer hypothesis could be probed by using additional observations of meltwater intrusions to further explore the parameter space in Figure 4.8. As described in Section 4.4.5, the relationship between melt fraction and plume height, which Jackson et al. (2020) demonstrate may be calculated from CTD profiles containing melt plume intrusions, was shown by Magorrian and Wells (2016) to be fundamental to the underlying dynamics of the standard coupled melt-plume model. We find a discrepancy between the predicted and observed values of the corresponding ratio $\frac{X_m}{D}$ for two sets of observations (above- and below-pycnocline) with relatively low observed stratification and thermal driving and inferred weak ambient currents, suggesting that these could be indicators of a convective boundary layer regime, which is consistent with existing theories. Conversely, we find good agreement between the model predictions and observations at LeConte, suggesting that the existing theory is a good match in a warmer, more stratified, and more energetic environment. Further observations could be used to establish whether this pattern is consistent.

If so, a more encouraging result of this work is that it suggests a potential framework in which standard oceanographic observations may be used to evaluate the applicability of the melt parameterization. With more observations one could estimate the dependence of w_c on N^2 and T_D and use that parameter space to predict where the model physics are likely to be applicable.

A final important point is that while the assumption of a shear-controlled boundary layer is implicit in the melt parameterization, the specific concern raised by this study applies only to its coupling to the plume model. Scaling of the melt equation coefficients creates a feedback with the plume momentum equation; for the standalone melt parameterization there is functionally no difference between adjustments to the empirical coefficients vs. the thermal driving input. However, the caveat raised above stands, in that there could be other consequences of forcing the existing parameterization to recreate observations from a convection-controlled regime by applying a constant correction. For example, if there is significant temporal variability in ambient current or temperature, this could cause the boundary layer regime to switch. This seems likely in the case of icebergs in a fjord such as Sermilik, where they are subjected to variable ocean velocity shear in addition to other drift forcings such as wind (Figure 4A; Sutherland et al., 2014; FitzMaurice et al., 2016; Wagner et al., 2017).

4.6 Conclusions

We present observations of melt intrusions observed in temperature and salinity profiles collected 70-240 m from an iceberg in Sermilik Fjord. Our analysis shows that the intrusions are significantly different above and below the pycnocline. The deep intrusions are estimated to originate from melt plumes with an average height of 50 m and melt content of 0.3%, while the shallow intrusions correspond to 15 m high plumes containing 0.2% melt. We find that the commonly-used melt plume model cannot reproduce the observed characteristics of either set of plumes, in contrast to results from Jackson et al. (2020) who established this analysis method in a study of LeConte Glacier in a relatively warm fjord in Alaska. We suggest that one possible explanation for this discrepancy is the melt parameterization assumption of a shear-controlled boundary layer, which could lead to underestimation of melt rate in a low thermal forcing environment if that assumption were violated. Building on the analysis of Magorrian and Wells (2016) who show that the ratio of plume height to melt fraction predicted by the model has a fixed relationship to the ambient thermal driving and stratification, we show that an adjustment to the thermal forcing input can force the model to reproduce the Sermilik observations. These findings amplify established concerns about the applicability of the melt plume parameterization in settings with low thermal forcing, stratification, and ambient velocity, and suggest the possibility of using observationally-derived $\frac{X_m}{D}$ as a diagnostic. Conversely, this is an encouraging result for the application of the existing model in warm, energetic settings more similar to LeConte. Further work is needed to determine whether this pattern holds in other settings and to consider alternative explanations for the discrepancy, such as the complexity of iceberg geometry.

Table 4.2. Summary of observed and simulated iceberg melt intrusion and plume characteristics, compared to results from LeConte Glacier (Jackson et al., 2020) and other published values.

	X_m [%]	D [m]	X_m/D [$\times10^{-3}$]	$\dot{m}$ [m d^{-1}]	w [cm s^{-1}]
Observed intrusions:					
all (n=66)	0.24±0.02	30±4	8.1 [6.4 10][a]	—	—
shallow (n=27)	0.20±0.02	14±2	14 [11 18]	—	—
deep (n=39)	0.31±0.04	53±2	5.9 [4.9 6.9]	—	—
Plume model:					
standard coefficient values[b]				0.04±0.00[c]	1.0±0.0
shallow	0.05±0.00	4±1	9.8	0.02±0.00	0.5±0.0
deep	0.05±0.00	14±4	3.4	0.06±0.00	1.3±0.1
J20 coefficients $C_D \times 4, \Gamma_{T,S} \times 2$				0.59±0.03	3.7±0.2
shallow	0.16±0.00	13±2	12	0.26±0.01	1.9±0.1
deep	0.20±0.00	57±29	3.5	0.80±0.03	4.9±0.2
other parameter adjustments (deep only)					
$C_D \times 4, \Gamma_{T,S} \times 3$	0.29*	108*	2.7	—	—
$C_D \times 40$	0.31*	105*	3.0	—	—
$\Gamma_{T,S} \times 6$	0.29*	109*	2.7	—	—
ΔT_D *adjustment* with $\Gamma_{T,S} \times 2.5$				0.95±0.04	3.7±0.1
shallow ($\Delta T_D = 3$°C)	0.19±0.00	14±2	14	0.31±0.01	2.0±0.1
deep ($\Delta T_D = 6$°C)	0.30±0.00	58±31	5.2	1.2±0.1	4.8±0.2
LeConte Bay (Jackson et al., 2020)**:**					
observed	1.1 ± 0.1	29 ± 4	38 [30 48]	—	—
model (standard)	0.09	3.1	29	0.05	—
model (J20)[d]	1.1	27	41	5.7	—
Bigg et al. (1997) parameterization	—	—		0.07±0.00	—
Schild et al. (2021) field study	—	—		0.16-0.27	—

*Only one plume reached neutral buoyancy below the pycnocline.

[a] Upper and lower bounds based on standard error of X_m and D.

[b] Standard coefficient values used for the plume model simulations were $C_D = 2.5 \times 10^{-3}$, $\Gamma_T = 2.2 \times 10^{-2}$, and $\Gamma_S = 6.2 \times 10^{-4}$.

[c] Grey cells are the mean over the entire simulated depth range, 80-280 m.

[d] In addition to the coefficient adjustments, these simulations prescribed a horizontal background velocity of 20 cm s^{-1}. Adjusting only C_D gave $X_m = 1.1, D = 33$ m, $X_m/D = 33 \times 10^{-3}$ m^{-1}; adjusting only $\Gamma_{T,S}$ gave $X_m = 1.1, D = 36$ m, $X_m/D = 31 \times 10^{-3}$ m^{-1} (Jackson et al., 2020).

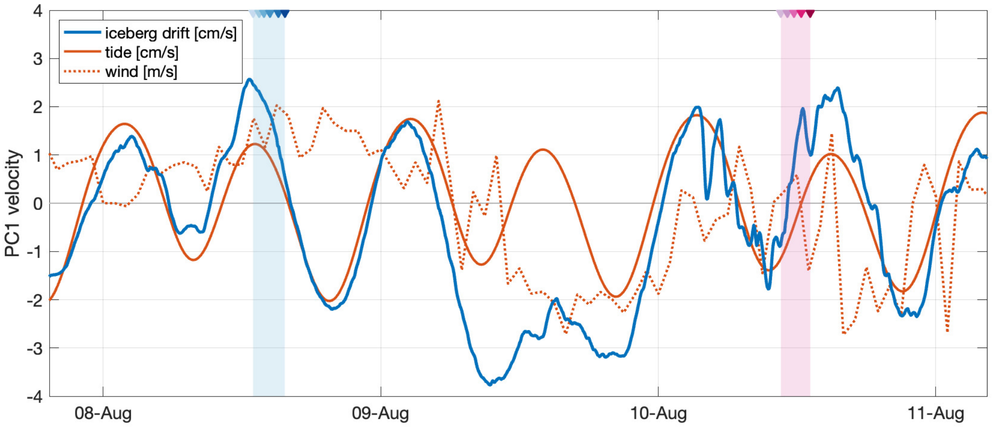

Figure 4A. Timeseries of along-fjord iceberg drift velocity (blue, in units of cm s^{-1}), estimated tidal velocity (red solid line, cm s^{-1}), and observed wind velocity in Tasiilaq (red dotted line, m s^{-1}); Cappelen et al., 2020). The shaded periods indicate the duration of survey 1 (blue) and survey 2 (pink) with triangles at the top indicating the start time of each profile.

4A Appendix A: Iceberg drift forcings

From a harmonic analysis of the iceberg drift velocity (Pawlowicz et al., 2002) we find that the along-fjord iceberg drift velocity during this time period is primarily controlled by tidal variation, consistent with the results of Sutherland et al. (2014) in a larger Sermilik iceberg tracking study. Between the two surveys, the iceberg drift appears to be more strongly controlled by wind (Figure 4A; Cappelen et al., 2020). This mismatch between the tidal velocity and drift velocity on August 9 suggests that the iceberg may have been suggested to stronger ambient shear during that period, while during our surveys on August 8 and 10, shear was likely low, facilitating the formation and persistence of the observed melt plume intrusions.

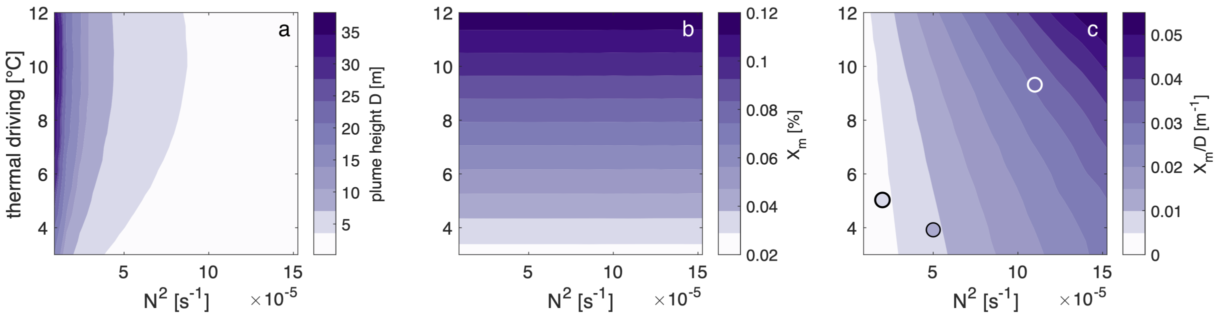

Figure 4B. Recreation of Figure 4.8 using standard coefficient values (Table 4.2). Results from plume model simulations over a range of stratification N^2 and thermal driving T_D values: (a) Plume height D (filled contours) and vertical velocity w (white contour lines, in units of cm s^{-1}). (b) Meltwater concentration X_m. (c) The associated slope $\frac{X_m}{D}$. Estimated observational values from Sermilik iceberg surveys (deep and shallow composites; black outlined circles) and LeConte (white outlined circle).

4B Appendix B: Idealized simulations with standard model parameters

Figure 4B is a recreation of Figure 4.8 using the standard coefficient values instead of the adjusted J20 values. We see that, while the magnitudes of D and X_m are lower than in the J20 simulations, the relationship $\frac{X_m}{D}$ is the same.

4C Appendix C: Manipulations of model equations referenced in Section 4.4.5

4C.1 Relationship between D and w

The plume density may be expressed in terms of the ambient density ρ_a, meltwater density ρ_m, and melt concentration X_m, as $\rho_p = X_m\rho_m + (1 - X_m)\rho_a$. Substituting this into the definition of reduced gravity of the plume, $g'_p = \frac{g}{\rho_0}\left[\rho_a - \rho_p\right]$, following some algebra we recover

$$g'_p = X_m g'_m, \tag{4C.1}$$

where g'_m is the reduced gravity of meltwater. We substitute Equation 4C.1 into the plume momentum Equation 4.3b, neglecting the drag term (Slater et al., 2016), and arrive at an alternative expression of the momentum flux,

$$\frac{d}{dz}(bw^2) = bX_m g'_m, \tag{4C.2}$$

where w is vertical velocity and b is plume width.

We rearrange the Magorrian and Wells (2016) scaling for plume height D (Equation 4.7) to show that $X_m g'_m = (K_n)^{-1} N^2 D$, and substitute this into Equation 4C.2 to obtain

$$\frac{d}{dz}(bw^2) = (K_n)^{-1} b N^2 D, \tag{4C.3}$$

where K_n is an empirical constant.

For constant stratification N^2, we expect the maximum plume velocity w_{max} to be reached at $z = \frac{1}{2}D$, and that b increases approximately linearly up to that point (Magorrian and Wells, 2016). Thus we assume the form $b(z) = A_1 z$ and integrate Equation 4C.3 from the base of the plume $z = 0$ to $z = \frac{1}{2}D$,

$$\begin{aligned}
\int_0^{\frac{1}{2}D} \frac{d}{dz}(bw^2)\, dz &= (K_n)^{-1} N^2 D \int_0^{\frac{1}{2}D} A_1 z\, dz, \\
A_1 \Big(\frac{1}{2}D\Big) w_{max}^2 &= (K_n)^{-1} N^2 D \frac{A_1}{2} \Big(\frac{1}{2}D\Big)^2, \\
w_{max}^2 &= (K_n)^{-1} A_2 N^2 D^2, \\
w_{max} &\propto ND, \qquad (4C.4)
\end{aligned}$$

showing that the maximum velocity w_{max} is proportional to the plume height D.

4C.2 Representation of melt parameterization in plume momentum equation

Starting from the rearranged plume momentum Equation 4C.2, we substitute the expression of X_m given by Equation 4.10 and the expression of g'_m given by Equation 4.9, and rewrite the momentum flux as

$$\frac{d}{dz}(bw^2) = bg\frac{c_w C_D^{1/2}\Gamma_T}{\alpha L}T_D\big(\beta_S S_a - \beta_T T_D\big), \tag{4C.5}$$

where g, c_w, and L are gravitational acceleration, specific heat of water, and latent heat of fusion; C_D and Γ_T are the drag coefficient and heat transfer coefficient; and β_S and β_T are the haline contraction and thermal expansion coefficients.

From this expression of Equation 4.3b, it is evident that scaling of the coefficients C_D and Γ_T in the melt parameterization Equation 4.4a has a proportional effect on plume momentum, and thus plume height D, according to Equation 4C.4. As such, the relationship $\frac{X_m}{D}$ is not sensitive to changes to those coefficients.

However, Equation 4C.5 also shows the nonlinear dependence of momentum on thermal driving T_D, such that multiplying T_D by a constant A yields

$$\frac{d}{dz}(bw^2) = bg\frac{c_w C_D^{1/2}\Gamma_T}{\alpha L}\big(AT_D\beta_S S_a - A^2\beta_T T_D^2\big),$$

i.e. for $A > 1$, the negative term increases in magnitude more than the positive term. This happens because increasing T_D causes more melt to be added to the plume, decreasing its density, but also decreases the ambient density, offsetting some of the change in buoyancy. This offset in momentum gain could shift the relationship between melt rate (i.e. X_m) and momentum (i.e. D). However, the effect of scaling T_D in the plume temperature Equation 4.3c must also be considered.

4C.3 Effect of adjustments to T_D on ambient stratification

Above we consider the addition of meltwater to the plume and the reduction of the ambient density, which have opposite effects on plume buoyancy. An additional impact of increasing T_D is that the ambient waters entrained by the plume are less dense, which has the potential to counteract the latter effect. To evaluate this, we return to the Magorrian and Wells (2016) scaling (Equation 4.6 & 4.7), which we rewrite as

$$D = \mathcal{C} T_D (\rho_a - \rho_m) \left| \frac{\partial \rho_a}{\partial z} \right|^{-1}, \tag{4C.6}$$

where the constants have been summarized as $\mathcal{C} = K_n \frac{c_w C_D^{1/2} \Gamma_T}{\alpha L}$, i.e. $X_m = \frac{\mathcal{C}}{K_n} T_D$. We also make the approximation here that $T_D \approx T_a$ for simplicity.

By expanding $\rho_a = \rho_0 \big[1 + \beta_S (S_a - S_0) - \beta_T (T_a - T_0) \big]$ and substituting its derivative with respect to z into Equation 4C.6, we see that

$$D = \mathcal{C} T_D \frac{\beta_S S_a - \beta_T T_D}{\beta_S \frac{\partial S_a}{\partial z} - \beta_T \frac{\partial T_a}{\partial z}}. \tag{4C.7}$$

Here the numerator is analogous to the plume momentum equation as expressed in Equation 4C.5, while the denominator accounts for the effect of temperature on the ambient stratification.

For $\frac{\partial T_a}{\partial z} = 0$, multiplying the temperature by a constant will affect the ambient density, but not the stratification, so multiplying T_D by A will have the nonlinear effect described above on the plume momentum.

For $\frac{\partial T_a}{\partial z} \neq 0$, the temperature term in the denominator also gains a factor of A, weakening this effect, such that there is little or no change in $\frac{X_m}{D}$. However, if instead T_D is replaced by $T_D + K$, this shifts the mean of T_a without changing $\frac{\partial T_a}{\partial z}$ so there is no effect on the stratification. As a result the nonlinear effect on momentum is retained.

Acknowledgments

Chapter 4 is currently in preparation to be submitted for publication. The dissertation author was the primary investigator and author of this material.

Chapter 5

Physical controls on mercury distribution in Sermilik Fjord

5.1 Introduction

As mass loss from the Greenland Ice Sheet (GrIS) has accelerated, the role of ice sheets in biogeochemical cycles has drawn increased attention. The ice sheet base is the site of enhanced physical and biogeochemical weathering and meltwater becomes enriched in minerals as it flows through the subglacial hydrological system (Chu, 2014). The resulting meltwater flux constitutes a significant source of some trace elements to the ocean, including micronutrients such as iron (Bhatia et al., 2013; Hawkings et al., 2020). At marine-terminating glaciers, subglacial runoff also fertilizes the surface ocean indirectly through upwelling of nutrient-rich deep ocean waters (Cape et al., 2019). Both the direct input of glacially-sourced minerals and the redistribution of ocean nutrients can affect ecosystem productivity, with implications for the global carbon cycle (Meire et al., 2017; Wadham et al., 2019). These processes are likely to be enhanced by ongoing warming and increased GrIS surface melt (Flowers, 2018).

A recent study by Hawkings et al. (2021) found high concentrations of mercury, a toxic trace metal, in surface waters downstream of land-terminating glaciers in southwestern Greenland. This raises the possibility that, in addition to nutrients, GrIS meltwater fluxes could also constitute a significant source of toxins to the ocean. Organic methylmercury bioaccumulates in marine ecosystems, and particularly elevated levels have been found in Arctic food webs, which are central to the diets of many indigenous communities (Dewailly et al., 2001; Lavoie et al., 2013; Stern et al., 2012; Dastoor et al., 2022), a problem that could be exacerbated by increasing melt if it is enriched in mercury. However, there are very few observations of mercury around Greenland, so it is unknown whether the large fluxes reported by Hawkings et al. (2021) are a widespread phenomenon. Furthermore, like other trace elements, including iron, the fate of mercury in the ocean is influenced by nonconservative processes, particularly in estuarine and coastal systems (Amos et al., 2014; Bruland and Lohan, 2003; Buck et al., 2015; Krause et al., 2021).

Using observations from an August 2021 field campaign in Sermilik Fjord, a well-studied glacial fjord in southeast Greenland, this study aims to address two primary questions raised by the Hawkings et al. (2021) results. First, are comparable Hg concentrations found at outlet glaciers in other regions of Greenland? Second, how do fjord dynamics associated with marine-terminating glaciers affect the resulting Hg distribution and export concentration?

5.2 Background

5.2.1 Sermilik Fjord circulation

Sermilik Fjord is a 90 km long, 5-10 km wide fjord that connects Helheim Glacier to the ocean (Straneo et al., 2016). In front of the glacier terminus, a dense ice melange comprised of large icebergs, bergy bits, and sea ice extends about 20 km down the fjord (Figure 5.1). During the non-summer months, variability on the shelf outside the fjord is the primary driver of circulation, but during the summer, glacier melt drives an estuarine circulation (e.g. Straneo et al., 2011; Jackson et al., 2014; Straneo and Cenedese, 2015) (Figure 5.2).

Deep Atlantic Water (AW), which is relatively warm and salty, and cold, fresh

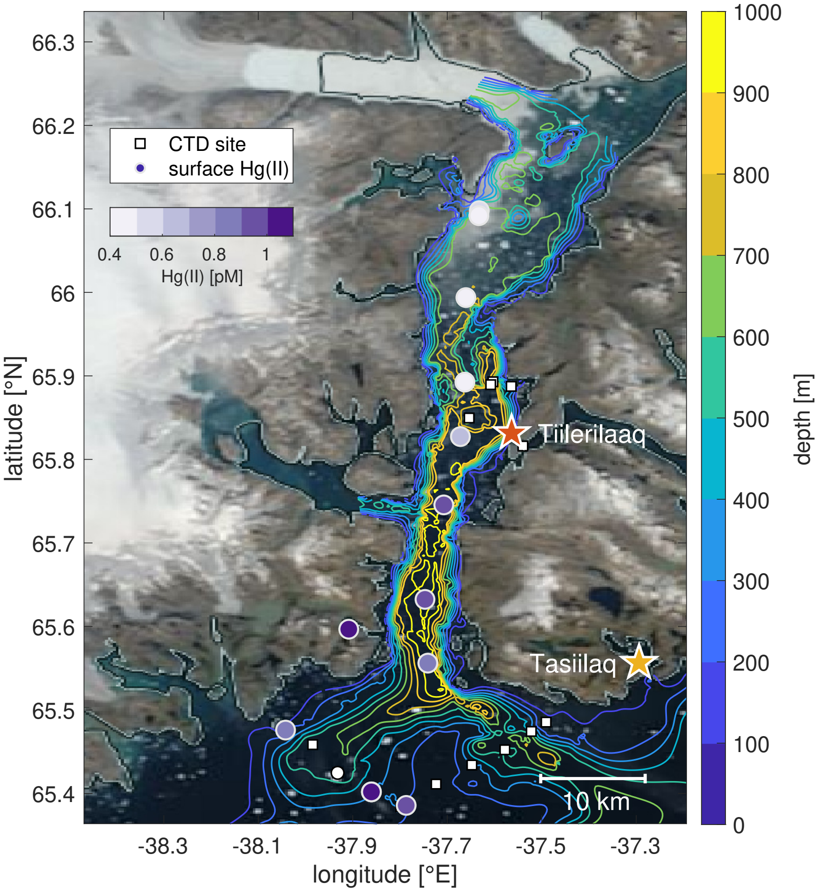

Figure 5.1. Map of Sermilik Fjord and adjacent continental shelf showing 2021 survey stations. The colored circles indicate the surface concentration of Hg(II) where surface samples were taken. No water samples were collected at the other CTD sites (white squares). Bathymetry is plotted as colored contours in the fjord and on the continental shelf. Toward the northwest the fjord surface is covered in ice melange, and the terminus of Helheim glacier is seen further west (above the legend). The major nearby settlements are Tiilerilaaq (formerly Tiniteqilaaq; red star) and Tasiilaq (yellow star). Background image from Landsat (13 Aug 2021).

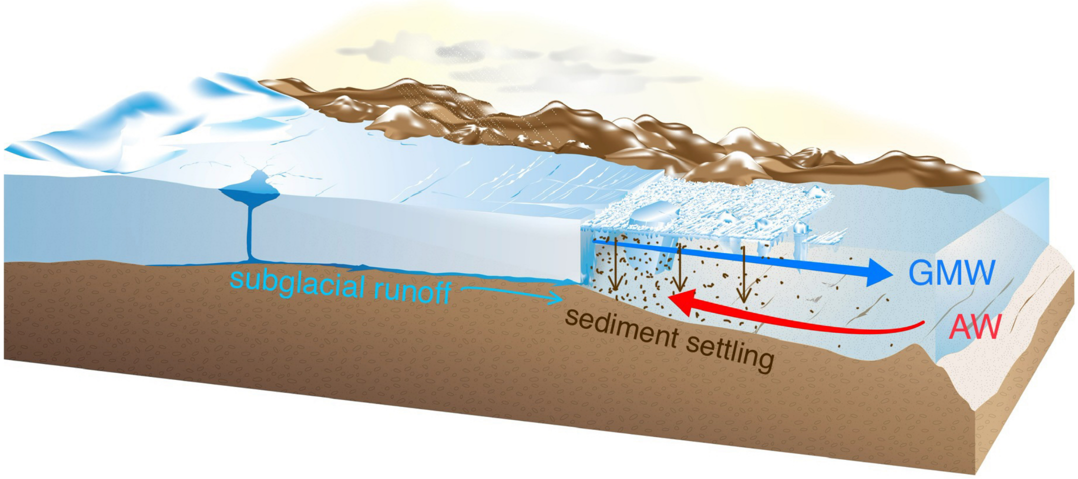

Figure 5.2. Schematic of a marine-terminating glacier with proglacial ice melange (modified from Straneo et al., 2013).

Polar Water (PW) are found on the shelf year-round. During summer, PW is overlain by fresher, warmer Warm Polar Water (WPW). In the fjord, these water masses are modified by glacial meltwater. Submarine meltwater (SMW) is produced by ocean melting of both the terminus and icebergs throughout the fjord. Subglacial runoff (SGR) is surface melt that is transported through channels at the ice base and flows into the ocean at the 600 m-deep glacier grounding line. The release of freshwater at depth creates a buoyant plume that rises along the ice face and entrains ambient AW through turbulent mixing. The resulting glacially-modified water (GMW) is generally warmer than shelf waters of the same density due to the significant AW content.

The SGR plume transports a large volume of sediment from the ice sheet bed (Chu, 2014). Much of the sediment in the plume settles close to the terminus, though some remains in suspension (Mugford and Dowdeswell, 2011; Sutherland et al., 2020). Additional glacial sediment is carried by icebergs and released into the fjord as they melt (iceberg rafted debris, IRD; Figure 5.3). Much of the iceberg melt occurs within the melange, but IRD is nonetheless the primary source of sediment deposited along the fjord (Andresen et al., 2012).

Using noble gas tracers, Beaird et al. (2018) show that AW comprises 88% of GMW in Sermilik Fjord. Accordingly, Cape et al. (2019) find that GMW in the fjord has similar macronutrient concentrations to deep AW on the shelf, whereas the overlying PW is depleted in nutrients. Ice melt is also low in macronutrients, indicating that the upwelled AW primarily determines the GMW properties.

In contrast, both SMW and SGR contain high concentrations of the micronutrient iron relative to the regional ocean, sourced both from within glacial ice and from subglacial sediments (Bhatia et al., 2013). This iron supply is ecologically significant in fjords and coastal waters in both Greenland and Antarctica (Kanna et al., 2020; Forsch et al., 2021).

While the noble gases used by Beaird et al. (2018) were selected because of their conservative behavior in the ocean on timescales relevant to fjord circulation, interpretation of biogeochemically-active tracer distributions requires knowledge of other relevant processes. Macronutrient concentrations are rapidly drawn down in the photic zone due to uptake by primary producers (Cape et al., 2019). Iron is also subject to biological drawdown, but its concentration in Greenland fjords is more strongly influenced by flocculation and sinking (Hopwood et al., 2016; Kanna et al., 2020).

5.2.2 Ocean mercury cycling

Mercury is a neurotoxicant that is found naturally in the ocean in the forms of inorganic divalent mercury (Hg(II)), organic methyl- and dimethyl mercury (MeHg), and elemental mercury (Hg(0); e.g. Selin, 2009; Bowman et al., 2020). Phytoplankton and other primary producers preferentially take up MeHg, which bioaccumulates in marine food webs, potentially reaching concentrations dangerous to human and ecosystem health at higher trophic levels (e.g. Pickhardt and Fisher, 2007; Chen et al., 2009; Schartup et al., 2018). Environmental mercury concentrations have increased globally over the past

Figure 5.3. Left: Aerial view of Sermilik Fjord ice melange about 10 km from the terminus, looking up-fjord toward Helheim Glacier in the background. Right: Photo of a sediment-laden iceberg (foreground left) near the location of the northernmost station in Figure 5.1. Increasing surface ice concentration is visible toward the island in the background, identifiable on the map at about 66.2°N, 37.6°W. (Both photos from August 12, 2021, immediately before the start of the cruise.)

150 years, with particularly damaging effects to Arctic ecosystems and communities (e.g. AMAP 2021).

Mercury enters the global ocean primarily through atmospheric deposition (Hg(0) and Hg(II)) and river inputs (also MeHg; e.g. Selin, 2009; Schartup et al., 2013; Amos et al., 2014). A recent study by (Hawkings et al., 2021) suggested that concentrations of both Hg(II) and MeHg in meltwater runoff from the Greenland Ice Sheet are substantially higher than observed in previous observations of Greenland proglacial rivers and other Arctic rivers (Søndergaard et al., 2012, 2015). The implications of this finding are especially concerning because SGR in glacial fjords supports productive marine ecosystems, and because the associated mercury fluxes could be expected to increase with accelerating ice surface sheet melt (Meire et al., 2017; Muntjewerf et al., 2020).

Fjord mercury concentrations may be affected by a number of processes in addition to those described in Section 5.2.1. The typical open-ocean profile of total mercury (generally dominated by Hg(II)) can be described as "scavenged-type," with concentrations decreasing with depth (i.e. distance from the surface source; Bruland and Lohan, 2003; Bowman et al., 2020). Akin to the "biological pump" that exports carbon and other tracers from the surface ocean, dissolved Hg binds to various types of particles, including particulate organic matter and lithogenic particles, and is removed from the water column through sinking and burial in sediments (Lamborg et al., 2016). This Hg sink is more efficient in coastal oceans and estuaries, where sedimentation rates are higher, though resuspension of estuarine sediments complicates this in some systems, particularly with respect to MeHg (Amos et al., 2014; Buck et al., 2015; Gosnell et al., 2016).

MeHg is formed through methylation of Hg(II), a poorly understood process that is linked to microbial activity in sediments, anoxic ocean waters, and sea ice (Hammerschmidt and Fitzgerald, 2006; Mason et al., 1993; Schartup et al., 2020). It is typically depleted at the surface due to photodegradation and evasion to the atmosphere (Selin, 2009; Bowman et al., 2020). In exception to this pattern, relatively high MeHg concentrations are found near the surface in the Arctic Ocean, in part because sea ice cover impedes those processes (Soerensen et al., 2016; Bowman et al., 2020; Schartup et al., 2020). Due to the many complex chemical and biological processes that determine ocean MeHg concentrations, this study focuses on Hg(II) distribution.

5.3 Methods

5.3.1 Sermilik Fjord cruise

Measurements in Sermilik Fjord were conducted from the M/V Adolf Jensen from August 12-18, 2021. Salinity, temperature, and dissolved oxygen profiles were collected using a Seabird 25plus CTD along the length of the fjord and across the fjord inflow and outflow (Figure 5.1). For most profiles, turbidity was also measured using an RBR Concerto CTD. Additionally, water samples were collected from rosette-mounted and line-mounted Niskin bottles for mercury (THg and MeHg) and δ^{18}O analysis. Dense ice melange prevented ship transit into the northern reaches of the fjord, preventing the collection of water samples there (Figure 5.3).

5.3.2 Mercury samples

Sampling methods

Inside the fjord, mercury samples were typically taken at 600, 300, 200, 100, 50, 20, 10, and 2 m depth using an 8-bottle rosette (Standard Model 110A, 8 L). Due to the lack of a conductive cable, sampling depths were pre-determined based on prior casts. Outside the fjord, on the shelf, the use of the rosette was not possible due to high seas. Instead, water samples were collected with two line-mounted Niskin bottles (Model 1010 Niskin Water Sampler, 2.5 L), which limited the number of samples on the shelf.

Surface water samples were also collected by hand at 3 terrestrial sites: one lake and one river near Tiilerilaaq (Figure 5.1, red star), and one river near Tasiilaq (Figure

5.1, yellow star). These water bodies are fed by glacier melt from smaller ice caps separate from the ice sheet (as well as precipitation).

Samples were collected in 0.25 L precleaned borosilicate glass bottles (I-Chem) for THg and MeHg analysis. After sample collection, both THg and MeHg samples were acidified to 0.4% ultrapure hydrochloric acid (Optima, Fisher Chemical), stored at 4°C and analyzed within 6 months of sampling.

The analysis of the mercury samples was performed by Amina Schartup and Hannah Adams at Scripps Institution of Oceanography.

Total mercury analysis

THg samples were prepared and analyzed following US EPA Method 1631 (US Environmental Protection Agency, 2002). All Hg species were oxidized to inorganic Hg(II) overnight with bromine monochloride, and then reduced to volatile elemental Hg (Hg0) with 20% wt:vol tin(II) chloride solution (J.T. Baker) in 10% hydrochloric acid (Optima, Fisher Chemical). Hg0 was purged onto a gold trap with Hg-free argon gas and thermally desorbed into a cold-vapor atomic fluorescence spectrometer (CV-AFS) for detection using a Tekran 2600 Automated Mercury Analyzer. Sample concentrations were determined by a calibration curve based on standards prepared from a certified 1000 ppm Hg(II) standard (SPEX CertiPrep). The method detection limit was 0.23 pM (n=13 blanks), and ongoing precision and recovery was 100.4 ± 8.2% (n=11).

Methyl mercury analysis

MeHg samples were prepared and analyzed by ascorbic acid-assisted direct ethylation following Munson et al. (2014) and US EPA Method 1630 (US Environmental Protection Agency, 1998). Briefly, samples were digested overnight with 1% trace metal grade sulfuric acid (Fisher). Samples were then adjusted to a pH of 4.8 using a 2 M acetate/glacial acetic acid buffer (J.T. Baker) in ultrapure water (Milli-Q, 18.2 MWcm-1) and 8 M potassium hydroxide (J.T. Baker) in ultrapure water (Milli-Q, 18.2 MWcm-1). 2.5% wt:vol ascorbic acid solution (J.T. Baker) in ultrapure water was added to the samples, then samples were ethylated with sodium tetraethylborate solution (1% NaTEB in 2% potassium hydroxide, Strem) to convert MeHg to volatile methylethylmercury (MeEtHg). Ethylation was allowed to proceed for 10 minutes before sample analysis. Samples were analyzed on a Tekran 2700 Automated Methylmercury Analyzer. Sample concentrations were determined by a calibration curve based on standards prepared from a certified 1000 ppm methylmercury(II) chloride standard (Alfa Aesar). The method detection limit was 0.0156 pM (n=10 blanks), and ongoing precision and recovery was 102.9 ± 2.7% (n=15).

GEOTRACES data

In addition to the Sermilik Fjord samples, we include Hg(II) concentrations from a 2014 GEOTRACES cruise in Figure 5.4 (Mawji et al., 2015). Stations 53 and 56 are located on the continental shelf east of Cape Farewell, approximately 700 km SSW of Sermilik Fjord.

5.3.3 Water mass analysis

As described in Section 5.2.1, we expect that the majority of waters in Sermilik Fjord are constituted from mixing of four endmembers: the two shelf water masses, AW and PW, and the two glacial inputs, SMW and SGR (Figure 5.4). Near the surface we expect the ocean properties to also be influenced by mixing with WPW and nonconservative surface processes (e.g. insolation, air-sea fluxes, primary production).

SGR is represented on the T-S plot as a water mass with zero salinity and temperature at the local freezing point ($\sim 0°$C), which mixes with the ambient ocean properties at the grounding line depth (Figure 5.4, dot-dash line). To represent SMW, the combined effects of latent heat uptake and meltwater input are represented by mixing with freshwater at an "effective temperature" of $\sim -87°$C (Figure 5.4, dashed line; Gade, 1979; Straneo and Cenedese, 2015). Both of these mixing lines are described further in Section 2.1.

In addition to interpretation of the T-S plot, we quantitatively decompose the fractions of the four major endmembers in our observations using a simple linear mixing model (Tomczak, 1981). The properties resulting from conservative mixing between n water masses can be represented as a linear system of equations,

$$\mathbf{A}\mathbf{x} - \mathbf{d} = \mathbf{r}, \tag{5.1}$$

where $\mathbf{A}$ is the $n \times n$ matrix of constraints ($n-1$ endmember tracer values, and mass conservation), $\mathbf{x}$ is the unknown $n \times 1$ vector of water mass fractions, $\mathbf{d}$ is the $n \times 1$ vector of observed tracer values, and $\mathbf{r}$ is the $n \times 1$ residual misfit. We calculate the least squares solution of $\mathbf{x}$ for each observation, requiring that all water mass fraction values must be greater than or equal to 0.

We use dissolved oxygen as an independent constraint for the decomposition, in addition to temperature and salinity. Dissolved oxygen has been used for similar analyses in the Amundsen Sea, where there are three major endmembers (two ocean water masses and SMW; Jenkins, 1999; Biddle et al., 2017, 2019). As in those studies, we exclude the near-surface ocean from the analysis, and approximate that subsurface dissolved oxygen is a conservative tracer over the depth range and time scale relevant to this study.

We estimate endmember properties for AW and PW from CTD profiles measured on the shelf (Section 5.3.1) and use the established characteristic temperature and salinity for each glacial input. For both SMW and SGR, we use a dissolved oxygen concentration that was estimated for ice melt in the Amundsen Sea (Martinerie et al., 1992; Hellmer et al., 1998; Biddle et al., 2017). The applicability of this value in Sermilik Fjord is further supported by an analysis of dissolved oxygen in the iceberg melt intrusions identified in Chapter 4, which is described in Appendix 5A. Though SGR is discharged into the fjord at the glacier grounding line, it originates on the ice sheet surface, where it exchanges gases with the atmosphere (Beaird et al., 2015, 2018). However, similar surface values of dissolved oxygen have been observed in cold Arctic lakes (12-16 mg L^{-1} at 0-2°C; Leppi et al., 2016), suggesting that potential equilibration with the atmosphere is unlikely to alter the dissolved oxygen concentration substantially, so we use the same estimate for SGR and SMW. The endmember tracer values used in our analysis are given in Table 5.1.

A more sophisticated form of this technique, Optimum Multiparameter analysis (OMP), was applied in Sermilik Fjord by Beaird et al. (2018), using noble gas concentrations. OMP requires measurements of additional tracers, resulting in an overdetermined system (as in the Amundsen Sea studies by Biddle et al., 2017, 2019). This allows tracers with well-constrained endmember values (e.g. temperature and salinity) to be weighted more heavily than uncertain values (e.g. dissolved oxygen, in the case of the glacial endmembers), whereas each tracer is weighted equally in our analysis. This is likely to be especially important in interpreting the glacial endmember concentrations, which are relatively small (∼0-5%; Beaird et al., 2018) and have the most uncertain tracer values. AW and PW concentrations are generally in the range of ∼10-100% in the upper 400 m of the water column. In this study, we report the analysis results for all endmembers but only include AW and PW in our application.

5.3 Results

5.3.1 Water masses

Shelf water mass properties and decomposition

On the shelf we identify AW ($\theta \sim 4°\text{C}, SA \sim 34.9$ g $\text{kg}^{-1}, \sigma_0 > 27.5$ kg m^{-3}), PW ($\theta \sim -1.5°\text{C}, SA \sim 33.3$ g $\text{kg}^{-1}, \sigma_0 \sim 26.5$ kg m^{-3}), and WPW ($\theta \sim 4°\text{C}, SA \sim$ 31 g $\text{kg}^{-1}, \sigma_0 \sim 24.5$ kg m^{-3}; Figure 5.4). The lowest dissolved oxygen concentrations are observed in AW (6.4 mg L^{-1}) while PW is higher in oxygen (8.2 mg L^{-1}; Figure 5.5a).

These properties are used as endmember values for AW and PW in the water mass

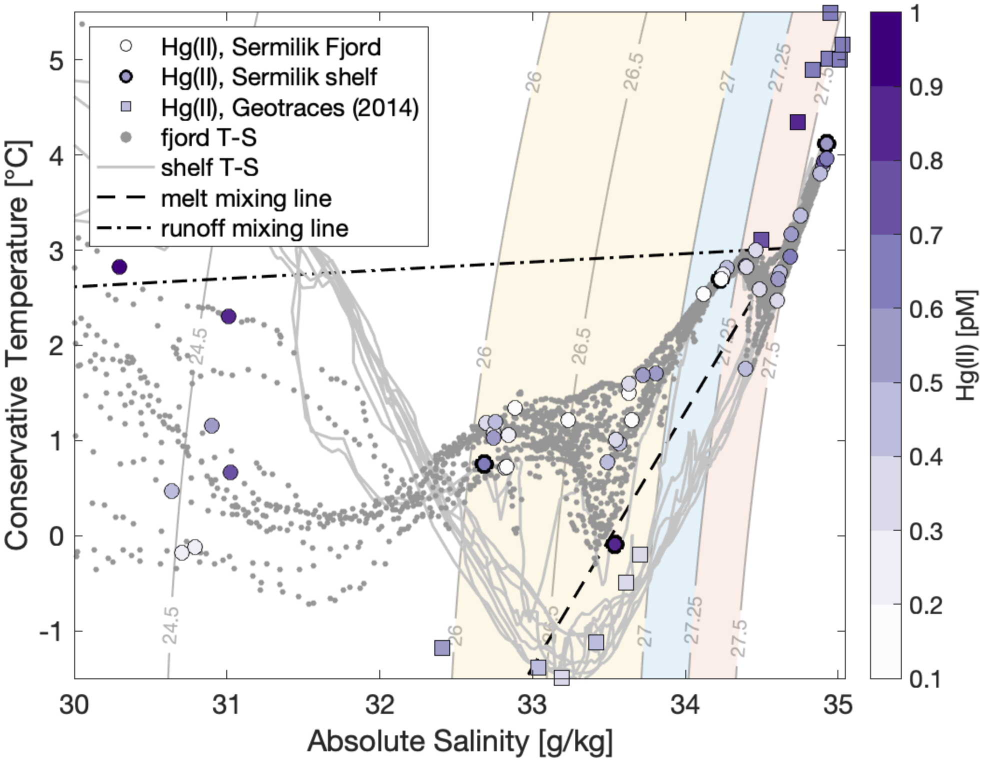

Figure 5.4. Temperature-salinity plot of Sermilik Fjord (grey dots) & shelf (grey lines) with Hg(II) concentration (colored circles; shelf samples have thick black outline). Hg(II) concentrations and corresponding water properties from the 2014 GEOTRACES survey (squares). Mixing lines are plotted for submarine ice melt (dashed line) and melt runoff (dot-dash line). The shaded density ranges denote fjord GMW layers defined in the text: upper (uGMW; yellow), core (cGMW; blue), and lower (lGMW; pink).

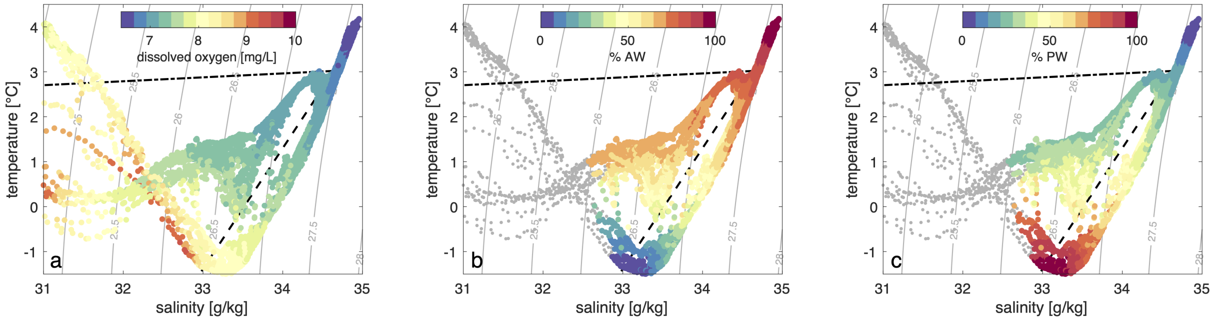

Figure 5.5. Temperature-salinity plots showing (a) dissolved oxygen concentration, and the estimated fraction of (b) AW and (c) PW for each observation. Water mass fractions are plotted below 50 m only.

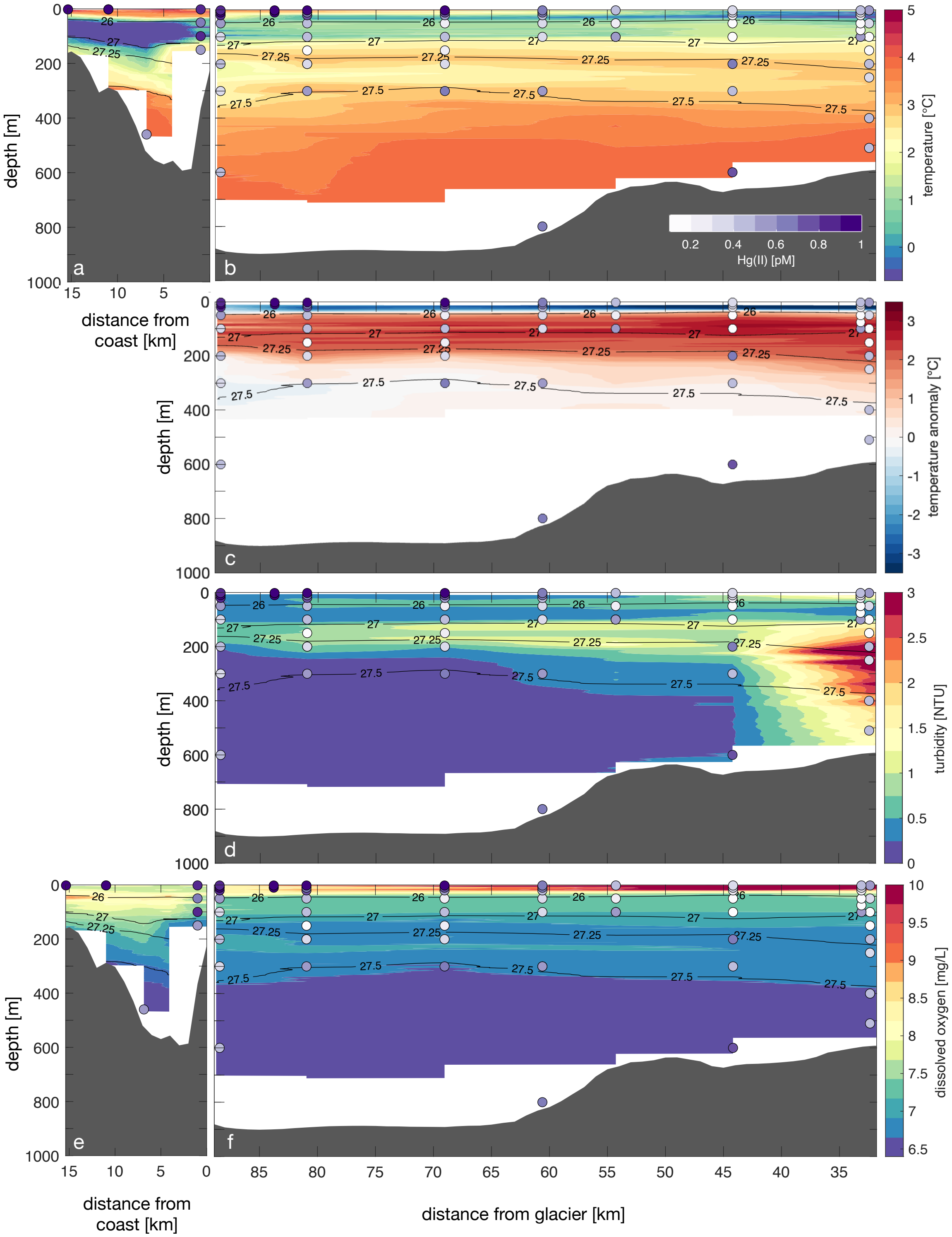

Figure 5.6. (a) Temperature section for west shelf transect. (b) Along-fjord temperature section. (c) Along-fjord isopycnal temperature anomaly relative to shelf. (d) Along-fjord turbidity. (e) West shelf dissolved oxygen. (d) Along-fjord dissolved oxygen. Hg(II) concentrations are plotted over each section according to colorbar in (b). The $\sigma_0 = 26$, 27, 27.25 and 27.5 kg m^{-3} isopycnals are overlaid on all sections (black contours). In fjord sections, the mouth is toward the left and the ice melange is toward the right.

Table 5.1. Endmember values for temperature, salinity, and dissolved oxygen concentration used in water mass mixing analysis.

Endmember	θ [°C]	SA [g kg^{-1}]	DO [mg L^{-1}]
AW	4.0	34.9	6.4
PW	-1.5	33.3	8.2
SGR	0	0	18
SMW	-87	0	18

decomposition, along with the SMW and SGR properties given in Table 5.1. Considering only points on the shelf, the decomposition finds that the AW core and PW core each contain 100% of the respective endmember, with a gradient in between, indicating that it is capturing the basic mixing between the two water masses (Figure 5.5b-c).

The western shelf temperature section shows a cold PW core between about 50 m and 100 m, with WPW above, and AW below 300 m in the deeper parts of the trough (Figure 5.6a). The dissolved oxygen section mirrors this structure, with the highest subsurface oxygen concentration coinciding with the coldest parts of the water column (Figure 5.6e). Both shelf sections have a gradient in the range of σ_0 =26-27 kg m^{-3} from cold, high oxygen PW to more fjord-like properties.

Glacial modification in the fjord

The deepest fjord waters ($\sigma_0 \geq 27.5$ kg m^{-3}) are indistinguishable from AW observed on the shelf (Figure 5.4). At lower densities, the fjord T-S properties are distinct from the shelf and fall between the melt and runoff mixing lines. Broadly speaking, these are glacially-modified waters, but we divide them into four density classes to aid in our analysis: lower GMW (lGMW), core GMW (cGMW), upper GMW (uGMW), and surface GMW (sGMW). These layers are described in detail here and their key characteristics are summarized in Table 5.2.

All of the fjord profiles depart from the shelf properties in the deepest of these layers, lGMW ($27.25 < \sigma_0 < 27.5$ kg m^{-3}), moving toward the runoff mixing line (Figure 5.4).

This results in a positive along-isopycnal temperature anomaly relative to the shelf. The variation in temperature anomaly along the 27.5 kg m^{-3} isopycnal indicates that there is an along-fjord gradient in the depth within the lGMW layer where this occurs (Figure 5.6c).

In the cGMW layer ($27 < \sigma_0 < 27.25$ kg m^{-3}), the fjord profiles are relatively uniform in T-S space, suggesting that this is the "core" of GMW export (Figure 5.4). This is reflected in the near-constant temperature anomaly along the fjord (Figure 5.6c).

Above this core layer, the spread in T-S properties increases, with evidence of mixing with PW in many of the profiles (Figures 5.4 and 5.5c). Indeed, the uGMW layer ($26 < \sigma_0 < 27$ kg m^{-3}) has a strong positive temperature anomaly toward the head of the fjord, decreasing toward the mouth, suggesting that there is mixing between uGMW and colder PW (Figure 5.6c). Evidence of interleaving in this density class can also be seen on the shelf, both in the T-S plot and in Figure 5.6a, which shows warmer waters in the upper 100 m in the profile nearest the fjord, adjacent to the cold PW core.

For $\sigma_0 < 25.5$ kg m^{-3}, fjord waters are generally colder than the shelf, likely due to cooling by iceberg melt (i.e. SMW; Figure 5.4). This surface layer (sGMW) has a strong negative temperature anomaly that decays toward the shelf (Figure 5.6c).

We expect a large flux of sediments from the SGR plume at the glacier terminus and IRD from icebergs melting in the melange, which is the likely explanation for the high turbidity over most of the water column near the melange edge (Figure 5.6d). Sediments settle at variable rates determined by particle density and radius. Strong currents are generally more turbulent than weaker flows and thus have higher vertical velocities, which can counteract settling, and they can also advect sediments further before they settle, both of which may contribute to higher suspended sediment loads in those layers. Moving down-fjord, the turbidity maximum consistently falls within the cGMW layer between 100-200 m, suggesting that this layer has the strongest current, which would keep more of the sediment that is released into the upper water column from the runoff plume and iceberg melt in suspension. The magnitude of the maximum decreases toward the mouth, consistent with gradual settling of glacier-sourced sediments along the length of the fjord. Directly above this, there is a turbidity minimum in the uGMW which is present along the length of the transect.

In the surface layer, there is a turbidity maximum toward the head of the fjord, which decays toward the shelf, like the temperature anomaly (Figure 5.6c-d). The same pattern is also seen in surface dissolved oxygen concentration, which is substantially higher near the melange than anywhere else, and decreases toward the mouth, but still remains higher than in the shelf surface layer (Figure 5.6e-f). (This signal is also present in oxygen saturation, i.e. it cannot be accounted for by the higher solubility of oxygen in cold water.) There are a few factors that likely contribute to these gradients. The temperature anomaly suggests that there is a high concentration of meltwater in this layer near the melange, which could contribute both sediment and oxygen to the water column (given that glacial endmembers are approximated to be higher in oxygen than ocean endmembers by roughly a factor of 2-3). This could also be a signal of high primary production, which we expect to be enhanced by melt-driven upwelling of AW.

The subsurface dissolved oxygen concentrations closely mirror the temperature section, with low oxygen associated with high temperature and vice versa, as expected based on the properties of AW and PW (Figure 5.6b, f). For example, the along-fjord temperature gradient in the lGMW between σ_0 =27.25-27.5 kg m^{-3} is associated with a gradient in dissolved oxygen. This relationship further supports the choice of dissolved oxygen as a subsurface tracer of AW and PW.

In summary, we divide the water column within the fjord into five layers based on their water mass composition as inferred from their T-S plot and other tracers. There is a deep layer of unmodified AW from the shelf and a middle layer of “core” GMW, each of which are effectively uniform along the length of the fjord, suggesting they are representative of the inflow and export properties, respectively. The core GMW is primarily a mixture of AW and SGR. Below and above the core GMW are lower and upper GMW layers with significant along-fjord gradients, suggesting mixing with the two shelf water masses, AW and PW, respectively. Finally, in the upper 50 m is a surface GMW layer that is very cold and fresh near the head of the fjord with a strong gradient toward the WPW on the shelf.

Table 5.2. Key characteristics of Sermilik Fjord water mass layers.

Fjord layer	σ [kg m^{-3}]	depth [m]	Hg(II)^{a} [pM]	MeHg [pM]
surface (n=9)	<23	≤2	0.71±0.25	0.05±0.02
sGMW (n=22)	<26	<50	0.64±0.25	0.07±0.02
uGMW (n=11)	26-27	50-130	0.34±0.15*	0.11±0.02
cGMW (n=4)	27-27.25	130-200	0.26±0.15*	0.11±0.02
lGMW (n=11)	27.25-27.5	200-350	0.47±0.09	0.13±0.01
AW (n=6)	>27.5	>350	0.57±0.15	0.13±0.02

^{a}Hg(II) and MeHg concentrations reported as mean ± standard deviation.
* = significantly different to AW concentration (95% confidence).

5.3.2 Mercury concentrations

Inorganic mercury (Hg(II))

The highest overall concentrations of Hg(II) were observed at the surface, with a maximum of 1.0 pM inside the fjord and 1.5 pM on the shelf (Figure 5.7a). The lowest surface concentrations are observed toward the head of the fjord, increasing toward the mouth and remaining high on the shelf (Figure 5.1). Within the fjord, surface Hg(II) concentration is positively correlated with distance from the glacier ($y = 0.010x + 0.100, R^2 = 0.74, p = 0.003$), and, relatedly, with surface salinity, which is highest near the mouth ($y = 0.068x - 0.905, R^2 = 0.52, p = 0.006$). We report these surface-only trends and include the mean values in Table 5.2 to facilitate comparison with other studies but focus the remainder of our analysis on the fjord layers identified in the previous section.

Samples in the fjord AW layer had a mean (± standard deviation) Hg(II) concentration of 0.57±0.15 pM (n=6). (Including the one sample within the AW layer on the shelf did not alter this value.) The concentration in the lGMW layer, which includes some unmodified shelf waters, was not significantly different (0.47±0.09 pM; p=0.09; n=11). However, the two mid-depth layers had significantly lower Hg(II) relative to AW. The cGMW mean was 0.26±0.15 pM (p=0.01; n=4) and the uGMW mean was 0.34±0.15 pM (p=0.004; n=11). The mean in the sGMW layer was 0.64±0.25 pM, not significantly different to AW (p=0.5; n=22). The resulting profile, with a subsurface minimum in cGMW and uGMW, is shown in Figure 5.8a.

Similar to the surface layer, Hg(II) in the sGMW layer (above 50 m, including surface samples) has a strong along-fjord gradient with highest values near the mouth ($y = 0.011x - 0.032, R^2 = 0.74, p = 10^{-7}$; Figure 5.8b). The uGMW layer has a weaker but still significant trend ($y = 0.005x + 0.087, R^2 = 0.33, p = 0.01$), while there is no along-fjord trend in the three lower layers.

Methylmercury (MeHg)

Surface waters had the lowest concentrations of MeHg, 0.02-0.07 pM in the fjord and 0.04-0.05 pM on the shelf (Figure 5.7b). MeHg concentration increases over the upper 100 m to 0.10-0.15 pM, with low variability deeper in the water column. Mean MeHg concentration for each fjord layer is reported in Table 5.2; there are no significant differences between layers as defined here. Surface MeHg is not significantly correlated with along-fjord distance or salinity, but MeHg above 100 m is weakly negatively correlated with along-fjord distance ($y = -0.0005x + 0.0621, R^2 = 0.18, p = 0.02$), in contrast to Hg(II). These results suggest that MeHg distribution is governed by different processes than Hg(II), likely including biological and chemical processes beyond the scope of this analysis, as described in Section 5.2.2.

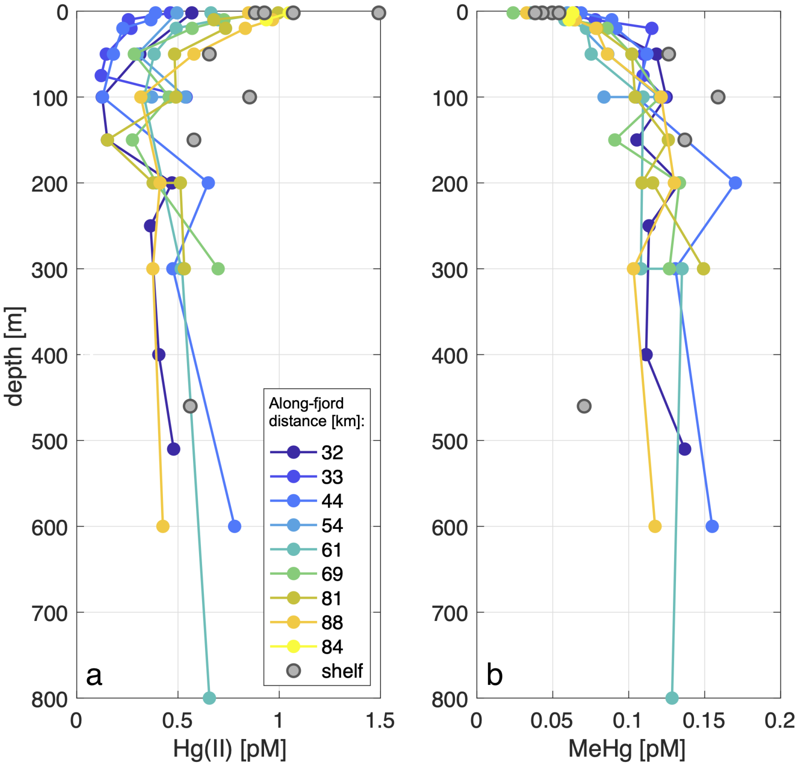

Figure 5.7. Depth profiles of (a) Hg(II) and (b) MeHg concentrations. Fjord profiles are colored by along-fjord distance from the glacier terminus, i.e. lower values closer to head of fjord. Shelf samples shown in grey.

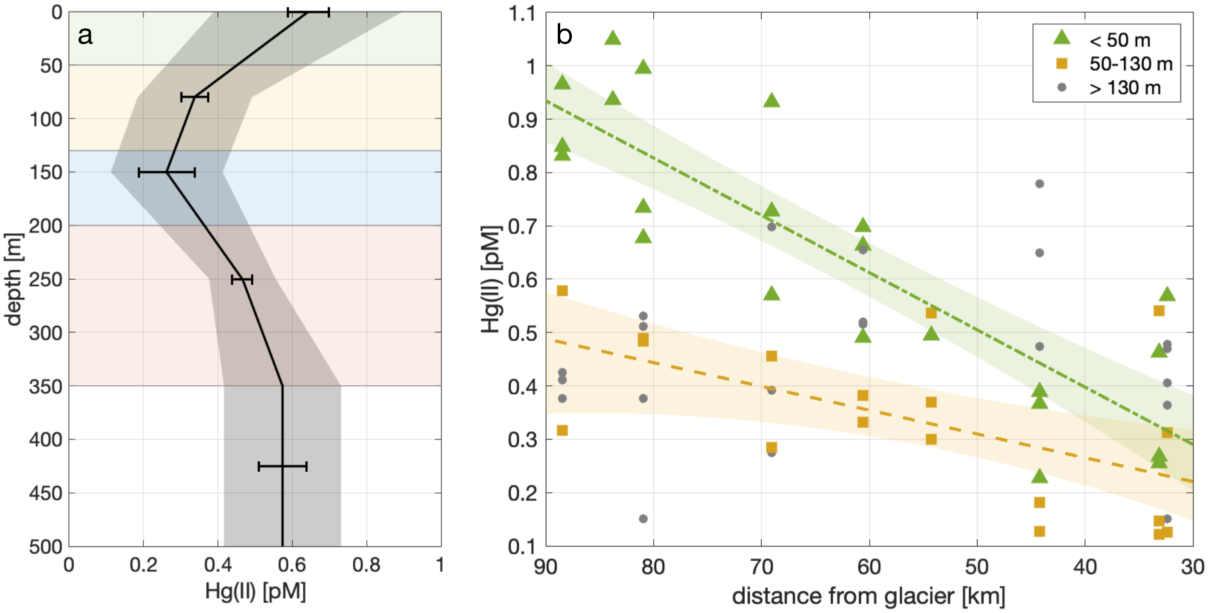

Figure 5.8. (a) Fjord-mean Hg(II) profile by water mass layer. Error bars show the standard error of the mean; shading is one standard deviation. The background shading denotes the approximate depth ranges of the fjord GMW layers defined in the text: surface (sGMW; green), upper (uGMW; yellow), core (cGMW; blue), and lower (lGMW; pink); and AW (unshaded). (b) Fjord Hg(II) vs along-fjord distance from terminus by water mass (green triangles [sGMW, <50 m], yellow squares [uGMW, 50-130 m], grey circles [> 130 m]). Trend lines are plotted for sGMW (dash-dot line) and uGMW (dashed line). Shaded error bars indicate the 95% confidence interval for each best-fit line.

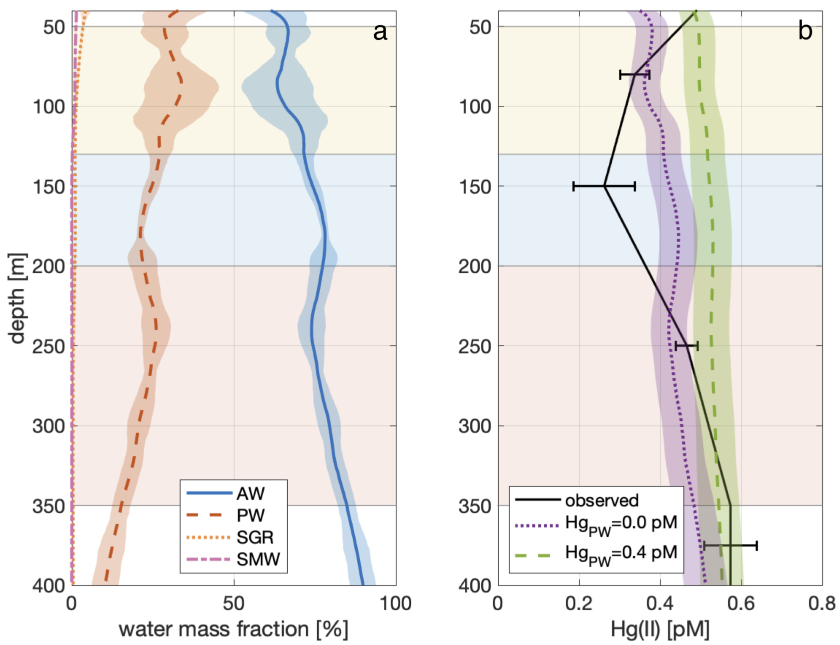

Figure 5.9. (a) Fjord-mean profiles of estimated water mass composition: AW (solid, blue), PW (dashed, red), SGR (dotted, orange), and SMW (dot-dash, pink). Shading on profiles is one standard deviation. (b) Observed fjord-mean profile of Hg(II) (solid, black). Predicted mean Hg(II) profiles calculated using the decomposition in (a) and two possible PW endmember values: 0 pM (purple, dotted) and 0.4 pM (green, dashed). Error bars on the observed profile are the standard error of the mean. Shading on the predicted profiles from standard error of AW concentration value. In both plots, the background shading denotes fjord GMW layers defined in the text: upper (uGMW; yellow), core (cGMW; blue), and lower (lGMW; pink).

River and lake samples

Surface samples were collected from one lake and two rivers. The Tiilerilaaq lake sample contained 1.9 pM Hg(II) and 0.10 pM MeHg, and the Tiilerilaaq river sample contained 3.1 pM Hg(II) and 0.10 pM MeHg (Figure 5.1, red star). The Tasiilaq river sample contained 0.71 pM Hg(II) and 0.04 pM MeHg (Figure 5.1, yellow star).

5.3.3 Mixing model prediction of Hg(II) distribution

To determine whether the observed Hg(II) distribution can be predicted by conservative mixing, we present an estimate of the fjord water mass composition, which we use to calculate a predicted Hg(II) profile for comparison to the observations. The fjord-average profiles of water mass composition from the mixing analysis are shown in Figure 5.9a. Qualitatively, the profiles are similar to the findings of the more complex OMP analysis by Beaird et al. (2018) in both vertical structure and magnitude (see their Figure S7; Section 5.3.3). We note that the standard deviations are largest in the depth range of 70-130 m, where we identify PW mixing with uGMW, and smallest in the cGMW range (130-180 m) where along-fjord gradients are small (see Section 5.3.1), suggesting that the decomposition is capturing some of the relevant variability that we observe in the fjord.

Because the SGR and SMW fractions are so small, we exclude them from the reconstruction. This implicitly assumes negligible Hg(II) concentrations in the glacial endmembers, which we argue is a reasonable approximation for this purpose assuming that Hg(II) concentrations in SGR and SMW are less than or equal to AW concentrations, as our results indicate.

To construct a predicted Hg(II) concentration profile, we use an AW concentration of 0.57 ± 0.06 pM (AW mean and standard error based on Table 5.2). The concentration in PW is unknown, so we consider two values for this endmember. As a lower bound, we use 0 pM. This is unlikely to be a realistic estimate given our result that Hg(II) concentrations in the uGMW layer are highest near the fjord mouth, where it mixes with PW (Figures 5.4). The trend line in Figure 5.8b suggests an Hg(II) concentration between 0.35 and 0.6 pM near the mouth. Results from a 2014 GEOTRACES survey indicate Hg(II) of about 0.4 pM in PW in that setting, where T-S properties and AW Hg(II) concentration were similar our observations (Figure 5.4; Mawji et al., 2015; Cossa et al., 2018). Based on these findings we use 0.4 pM as an alternative estimate for PW concentration, but our primary result is not sensitive to the choice of this value.

Under the assumption that AW is the only source of Hg(II) to the fjord, we find observed Hg(II) in the core GMW layer is still significantly lower than can be explained by mixing alone (Figure 5.9b, purple dotted line). The higher PW estimate yields a near-constant Hg(II) profile, which overestimates the observed Hg(II) in both the core and upper GMW layers (Figure 5.9b, green dashed line). We conclude that the Hg(II) content of GMW in Sermilik Fjord cannot be explained by conservative mixing.

5.4 Discussion

5.4.1 Glacial modification of ocean tracer distributions

Glacial meltwater inputs modify ocean properties and tracer concentrations both directly via mixing and latent heat uptake, and by redistributing other water masses. In Sermilik Fjord, the latter effect, specifically entrainment and upwelling of AW by the SGR plume, is dominant over most of the water column.

Subsurface ocean

Beaird et al. (2018) find that 88% of GMW in Sermilik Fjord is upwelled AW, with PW forming the second-largest constituent. Given their result that the combination of SGR and SMW constitute no more than 5% of the GMW on average, the potential for glacial inputs to directly decrease the concentration of a generic tracer by mixing is limited. For an Hg(II) concentration of 0.6 pM in AW, a 5% dilution would yield 0.57 pM, well within the standard error of the mean (Figure 5.8a). We show in Figure 5.9b that the observed decrease in Hg(II) concentration between the AW layer and cGMW layer is too large to be explained by dilution by the glacial endmembers, even accounting for the possibility of further dilution by PW.

Conversely, meltwater inputs may drive significant enrichment of a tracer if they contain substantially higher concentrations than the ocean water masses, as with the micronutrient iron (Kanna et al., 2020). Hawkings et al. (2021) report a mean Hg(II) concentration of 720 pM, with a range of 215-1730 pM, in three proglacial rivers in West Greenland. If their minimum value were representative of meltwater in Sermilik Fjord, at 5% of a GMW mixture, this would result in a concentration of roughly 11 pM. Based on observations from a downstream fjord, Hawkings et al. (2021) further speculate that some removal of Hg(II) by non-conservative processes occurs before the runoff enters the ocean, implying a meltwater Hg(II) concentration of closer to 60 pM (see following subsection), which yields a GMW concentration of at least 3 pM. These estimates are higher than any of the fjord or shelf samples and exceed the mean u- and cGMW estimates by an order of magnitude or more (Table 5.2; Figure 5.7a).

Surface ocean

All meltwater from land-terminating glaciers enters the ocean as surface runoff, eliminating the pathway for turbulent entrainment and upwelling of deep ocean waters that occurs in Sermilik Fjord (e.g. Meire et al., 2017). Consequently, the meltwater is typically concentrated in a very fresh near-surface layer, instead of being strongly diluted by ocean waters.

In two West Greenland fjords downstream of land-terminating glaciers, Hawkings et al. (2021) find surface Hg(II) concentrations of 12.5-30.6 pM and MeHg concentrations of 1.56-2.59 pM. Based on the salinity range of their observations, the maximum meltwater concentration of their samples is roughly 50%; making the same approximation, we estimate a maximum melt concentration for the Sermilik surface samples of roughly 30%, within a factor of 2. However, the surface concentrations of both Hg(II) and MeHg in Sermilik are lower by over one order of magnitude (Table 5.2; Figure 5.7a). Furthermore, surface Hg(II) concentration is lowest near the glacier (Figure 5.8b) and increases with salinity, while Hawkings et al. (2021) report the opposite trend. The inconsistencies between these results indicate that the differences in mercury distribution in Sermilik Fjord and downstream of the West Greenland glaciers studied by Hawkings et al. (2021) likely extend beyond the influence of marine- versus land-terminating glaciers on ocean mixing, suggesting very different mercury source concentrations.

5.4.2 Hg(II) depletion in GMW

If the observed Hg(II) depletion in GMW cannot be explained by mixing of the constituent water masses, as our results indicate, this implies that Hg(II) is being removed from the water column. As described in Section 5.2.2, burial of particle-bound Hg is the primary mechanism for this. Hg(II) can transition from the dissolved to the particulate phase through uptake by primary producers, the so-called "biological pump," but it also binds to other types of particles, including abiotic suspended sediment (Lamborg et al., 2016). Particulate Hg(II) is typically abundant in estuaries, leading to much more efficient burial than in the open ocean where the dissolved phase is dominant (Bowman et al., 2020; Amos et al., 2014; Choe et al., 2003).

In the 2021 survey, the northernmost survey site is separated from the glacier terminus by about 30 km, most of which is covered with ice melange (Figure 5.1). In addition to settling of sediment carried by the SGR plume, icebergs release sediment (ice-rafted debris; IRD) as they melt, resulting in high sedimentation rates toward the head of the fjord that decrease toward the mouth (Andresen et al., 2012). Our observations also show much higher turbidity at depth at the site closest to the melange edge that drops off dramatically over the 10 km separating it from the next profile (Figure 5.6d), consistent with the idea that the melange is characterized by high sediment concentrations throughout the water column.

We hypothesize that inflowing AW is the primary source of Hg(II) in Sermilik Fjord. We further speculate that Hg(II) concentrations in both AW and GMW are altered while transiting through the melange, where abundant subglacial sediment and IRD accelerate scavenging of Hg(II) from the water column. Notably, MeHg concentrations are constant below 50 m (Figure 5.7b; Table 5.2), indicating that the impact of this mechanism is limited to Hg(II). This finding suggests that the impact of marine-terminating glaciers on Hg(II) distribution likely varies due to fjord characteristics, particularly iceberg concentration.

5.5 Conclusions

We present results from an August 2021 survey of mercury distribution in Sermilik Fjord, southeast Greenland. In the fjord, we find that Hg(II) concentration ranges from 0.1 to 1.0 pM and MeHg ranges from 0.02 to 0.15 pM. Hg(II) is maximal at the surface with a minimum between 50 and 150 m depth, while MeHg increases from a surface minimum to near-constant profile below 100 m. The subsurface minimum in Hg(II) is associated with GMW and a simple mixing model suggests that the concentration is lower than can be explained by conservative mixing. Contrary to a recent study showing very high mercury concentrations in glacier runoff that were diluted by mixing with ocean waters in a West Greenland fjord (Hawkings et al., 2021), we find that Hg(II) concentration increases with distance from the terminus over the upper 130 m, suggesting that the Hg(II) depletion is likely linked to glacier-related processes. We hypothesize that inflowing AW is the primary source of Hg(II) to Sermilik Fjord and that Hg(II) may be removed from the water column by scavenging in the ice melange where there is increased sedimentation due to settling of particles suspended in the subglacial runoff plume and iceberg melt. As the fjord studied by Hawkings et al. (2021) is associated with a land-terminating glacier, there is no ice melange, offering one possible explanation for the discrepancy between the results from these two systems. Further work is needed to extend these findings to organic MeHg and to determine whether this mechanism is common among Greenland fjords.

5A Appendix: Dissolved oxygen in iceberg melt intrusions

The estimated dissolved oxygen concentration used for the two glacial endmembers in the water mass mixing analysis, 18 mg L^{-1}, originates from a study showing that oxygen concentrations in glacial ice depend on the conditions where the ice forms, which results in significant geographic variation (Martinerie et al., 1992; Biddle et al., 2017, 2019).

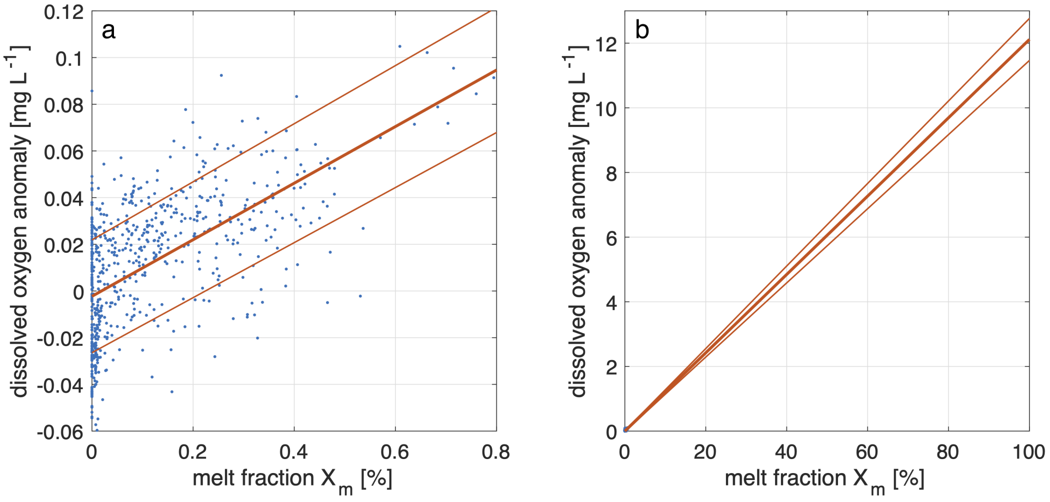

Figure 5A. (a) Calculated ice melt fraction vs dissolved oxygen anomaly below the 160 m pycnocline for both iceberg surveys in Chapter 4. (b) The same plot with the axes expanded to show $X_m = 100\%$.

To evaluate the appropriateness of this value from West Antarctica for application to a Greenland fjord, we plot the dissolved oxygen anomaly of the iceberg survey profiles from Chapter 4 against the derived melt fraction X_m (Figure 5Aa). We only use points from below the pycnocline (160 m), where the melt fractions are relatively high (Table 4.2). We use the resulting relationship, $y = 0.121x - 0.002$ ($R^2 = 0.34, p < 0.005$), to estimate the dissolved oxygen anomaly for $X_m = 100\%$ (Figure 5Ab). This yields an anomaly of 12.1±0.7 mg L^{-1}. Added to the background value of 6.9 mg L^{-1}, the estimated dissolved oxygen concentration of SMW based on the iceberg melt intrusions is about 19±1 mg L^{-1}, in agreement with the value used by Biddle et al. (2017, 2019).

Acknowledgments

Chapter 5 is currently in preparation to be submitted for publication. Margaret R. Lindeman, Fiammetta Straneo, Amina Schartup, Hannah Adams, and Monica Nelson. The dissertation author was the primary investigator and author of this material.

Bibliography

Adusumilli, S., H. A. Fricker, M. R. Siegfried, L. Padman, F. S. Paolo, and S. R. M. Ligtenberg, 2018: Variable Basal Melt Rates of Antarctic Peninsula Ice Shelves, 1994–2016. *Geophysical Research Letters*, **45**, 4086–4095, doi: 10.1002/2017GL076652.

Amos, H. M., D. J. Jacob, D. Kocman, H. M. Horowitz, Y. Zhang, S. Dutkiewicz, M. Horvat, E. S. Corbitt, D. P. Krabbenhoft, and E. M. Sunderland, 2014: Global biogeochemical implications of mercury discharges from rivers and sediment burial. *Environmental Science and Technology*, **48**, 9514–9522.

Andresen, C. S., F. Straneo, M. H. Ribergaard, A. A. Bjørk, T. J. Andersen, A. Kuijpers, N. Nørgaard-Pedersen, K. H. Kjær, F. Schjøth, K. Weckström, and A. P. Ahlstrøm, 2012: Rapid response of Helheim Glacier in Greenland to climate variability over the past century. *Nature Geoscience*, **5**, 37–41.

Arzeno, I. B., R. C. Beardsley, R. Limeburner, B. Owens, L. Padman, S. R. Springer, C. L. Stewart, and M. J. M. Williams, 2014: Ocean variability contributing to basal melt rate near the ice front of Ross Ice Shelf, Antarctica. *Journal of Geophysical Research: Oceans*, **119**, 4214–4233.

AWI, 2017: Polar Research and Supply Vessel POLARSTERN Operated by the Alfred-Wegener-Institute. *Journal of Large-scale Research Facilities*, **3**, A119.

Bamber, J. L., A. J. Tedstone, M. D. King, I. M. Howat, E. M. Enderlin, M. R. van den Broeke, and B. Noel, 2018: Land Ice Freshwater Budget of the Arctic and North Atlantic Oceans: 1. Data, Methods, and Results. *Journal of Geophysical Research: Oceans*, **123**, 1827–1837.

Beaird, N., F. Straneo, and W. Jenkins, 2015: Spreading of Greenland meltwaters in the ocean revealed by noble gases. *Geophysical Research Letters*, **42**, 7705–7713.

Beaird, N. L., F. Straneo, and W. Jenkins, 2018: Export of Strongly Diluted Greenland Meltwater From a Major Glacial Fjord. *Geophysical Research Letters*, **45**, 4163–4170.

Bell, R. E., W. Chu, J. Kingslake, I. Das, M. Tedesco, K. J. Tinto, C. J. Zappa, M. Frezzotti,

A. Boghosian, and W. S. Lee, 2017: Antarctic ice shelf potentially stabilized by export of meltwater in surface river. *Nature*, **544**, 344–348.

Beszczynska-Möller, A., E. Fahrbach, U. Schauer, and E. Hansen, 2012: Variability in Atlantic water temperature and transport at the entrance to the Arctic Ocean, 1997–2010. *ICES Journal of Marine Science*, **69**, 852–863.

Bhatia, M. P., E. B. Kujawinski, S. B. Das, C. F. Breier, P. B. Henderson, and M. A. Charette, 2013: Greenland meltwater as a significant and potentially bioavailable source of iron to the ocean. *Nature Geoscience*, **6**, 274–278.

Biddle, L. C., K. J. Heywood, J. Kaiser, and A. Jenkins, 2017: Glacial meltwater identification in the Amundsen Sea. *Journal of Physical Oceanography*, **47**, 933–954.

Biddle, L. C., B. Loose, and K. J. Heywood, 2019: Upper Ocean Distribution of Glacial Meltwater in the Amundsen Sea, Antarctica. *Journal of Geophysical Research: Oceans*, **124**, 6854–6870.

Bigg, G. R., M. R. Wadley, D. P. Stevens, and J. A. Johnson, 1997: Modelling the dynamics and thermodynamics of icebergs. *Cold Regions Science and Technology*, **26**, 113–135.

Bjørk, A. A., L. M. Kruse, and P. B. Michaelsen, 2015: Brief communication: Getting Greenland's glaciers right – a new data set of all official Greenlandic glacier names. *The Cryosphere*, **9**, 2215–2218.

Bourke, H., J. L. Newton, G. Paquette, and M. D. Tunnicliffe, 1987: Circulation and Water Masses of the East Greenland Shelf. *Journal of Geophysical Research: Oceans*, **92**, 6729–6740.

Bowman, K. L., C. H. Lamborg, and A. M. Agather, 2020: A global perspective on mercury cycling in the ocean. *Science of the Total Environment*, **710**.

Bruland, K. W. and M. C. Lohan, 2003: Controls of Trace Metals in Seawater. In Holland, H. D. and K. K. Turekian, eds., *Treatise on Geochemistry*, Elsevier, vol. 6, chap. 2, pp. 23–47.

Buck, C. S., C. R. Hammerschmidt, K. L. Bowman, G. A. Gill, and W. M. Landing, 2015: Flux of Total Mercury and Methylmercury to the Northern Gulf of Mexico from U.S. Estuaries. *Environmental Science and Technology*, **49**, 13992–13999.

Budéus, G. and W. Schneider, 1995: On the hydrography of the Northeast Water Polynya. *Journal of Geophysical Research: Oceans*, **100**, 4287–4299.

Cape, M. R., F. Straneo, N. Beaird, R. M. Bundy, and M. A. Charette, 2019: Nutrient release to oceans from buoyancy-driven upwelling at Greenland tidewater glaciers. *Nature Geoscience*, **12**, 34–39.

Cappelen, J., E. V. Laursen, C. Kern-Hansen, L. Boas, P. G. Wang, B. V. Joergensen, and L. S. Carstensen, 2020: Weather observations from Greenland 1958-2019 (DMI Report 20-08).

Chelton, D. B., R. A. DeSzoeke, M. G. Schlax, K. E. Naggar, and N. Siwertz, 1998: Geographical Variability of the First Baroclinic Rossby Radius of Deformation. *Journal of Physical Oceanography*, **28**, 433–460.

Chen, C. Y., M. Dionne, B. M. Mayes, D. M. Ward, S. Sturup, and B. P. Jackson, 2009: Mercury bioavailability and bioaccumulation in estuarine food webs in the Gulf of Maine. *Environmental Science and Technology*, **43**, 1804–1810.

Choe, K.-Y., G. A. Gill, and R. Lehman, 2003: Distribution of particulate, colloidal, and dissolved mercury in San Francisco Bay estuary. 1. Total mercury.

Choi, Y., M. Morlighem, E. Rignot, J. Mouginot, and M. Wood, 2017: Modeling the Response of Nioghalvfjerdsfjorden and Zachariae Isstrøm Glaciers, Greenland, to Ocean Forcing Over the Next Century. *Geophysical Research Letters*, **44**, 11,11–71,79, doi: 10.1002/2017GL075174.

Chu, V. W., 2014: Greenland ice sheet hydrology: A review. *Progress in Physical Geography: Earth and Environment*, **38**, 19–54.

Cossa, D., L. E. Heimbürger, F. F. Pérez, M. I. García-Ibáñez, J. E. Sonke, H. Planquette, P. Lherminier, J. Boutorh, M. Cheize, J. L. M. Barraqueta, R. Shelley, and G. Sarthou, 2018: Mercury distribution and transport in the North Atlantic Ocean along the GEOTRACES-GA01 transect. *Biogeosciences*, **15**, 2309–2323.

Cowton, T., D. Slater, A. Sole, D. Goldberg, and P. Nienow, 2015: Modeling the impact of glacial runoff on fjord circulation and submarine melt rate using a new subgrid-scale parameterization for glacial plumes. *Journal of Geophysical Research: Oceans*, **120**, 796–812.

Dastoor, A., H. Angot, J. Bieser, J. H. Christensen, T. A. Douglas, L. E. Heimbürger-Boavida, M. Jiskra, R. P. Mason, D. S. McLagan, D. Obrist, P. M. Outridge, M. V. Petrova, A. Ryjkov, K. A. S. Pierre, A. T. Schartup, A. L. Soerensen, K. Toyota, O. Travnikov, S. J. Wilson, and C. Zdanowicz, 2022: Arctic mercury cycling.

Davis, P. E. D., A. Jenkins, K. W. Nicholls, P. V. Brennan, E. P. Abrahamsen, K. J. Heywood, P. Dutrieux, K.-H. Cho, and T.-W. Kim, 2018: Variability in Basal Melting Beneath Pine Island Ice Shelf on Weekly to Monthly Timescales. *Journal of Geophysical*

Research: Oceans, **123**, 8655–8669.

Davison, B. J., T. Cowton, A. Sole, F. Cottier, and P. Nienow, 2022: Modelling the effect of submarine iceberg melting on glacier-adjacent water properties. *The Cryosphere*, **16**, 1181–1196.

Davison, B. J., T. R. Cowton, F. R. Cottier, and A. J. Sole, 2020: Iceberg melting substantially modifies oceanic heat flux towards a major Greenlandic tidewater glacier. *Nature Communications*, **11**, 5983.

de Steur, L., E. Hansen, C. Mauritzen, A. Beszczynska-Möller, and E. Fahrbach, 2014: Impact of recirculation on the East Greenland Current in Fram Strait: Results from moored current meter measurements between 1997 and 2009. *Deep-Sea Research Part I*, **92**, 26–40.

Dewailly, E., P. Ayotte, S. Bruneau, G. Lebel, P. Levallois, and J. P. Weber, 2001: Exposure of the inuit population of nunavik (Arctic Québec) to lead and mercury. *Archives of Environmental Health*, **56**, 350–357.

Dupont, T. K. and R. B. Alley, 2005: Assessment of the importance of ice-shelf buttressing to ice-sheet flow. *Geophysical Research Letters*, **32**, 1–4.

El-Tahan, M., S. Venkatesh, and H. El-Tahan, 1987: Validation and Quantitative Assessment of the Deterioration Mechanisms of Arctic Icebergs. *Journal of Offshore Mechanics and Arctic Engineering*, **109**, 102–108.

Enderlin, E. M. and G. S. Hamilton, 2014: Estimates of iceberg submarine melting from high-resolution digital elevation models: Application to Sermilik Fjord, East Greenland. *Journal of Glaciology*, **60**, 1111–1116.

Enderlin, E. M., G. S. Hamilton, F. Straneo, and D. A. Sutherland, 2016: Iceberg meltwater fluxes dominate the freshwater budget in Greenland's iceberg-congested glacial fjords. *Geophysical Research Letters*, **43**, 11,211–287,294.

FitzMaurice, A., C. Cenedese, and F. Straneo, 2017: Nonlinear response of iceberg side melting to ocean currents. *Geophysical Research Letters*, **44**, 5637–5644.

—, 2018: A Laboratory Study of Iceberg Side Melting in Vertically Sheared Flows. *Journal of Physical Oceanography*, **48**, 1367–1373.

FitzMaurice, A. and A. Stern, 2018: Parameterizing the basal melt of tabular icebergs. *Ocean Modelling*, **130**, 66–78.

FitzMaurice, A., F. Straneo, C. Cenedese, and M. Andres, 2016: Effect of a sheared flow on iceberg motion and melting. *Geophysical Research Letters*, **43**, 12,512–520,527.

Flowers, G. E., 2018: Hydrology and the future of the Greenland Ice Sheet. *Nature Communications*, **9**, 2729.

Forsch, K. O., L. Hahn-Woernle, R. M. Sherrell, V. J. Roccanova, K. Bu, D. Burdige, M. Vernet, and K. A. Barbeau, 2021: Seasonal dispersal of fjord meltwaters as an important source of iron and manganese to coastal Antarctic phytoplankton. *Biogeosciences*, **18**, 6349–6375.

Gade, H. G., 1979: Melting of Ice in Sea Water: A Primitive Model with Application to the Antarctic Ice Shelf and Icebergs. *Journal of Physical Oceanography*, **9**, 189–198.

Gosnell, K., P. Balcom, V. Ortiz, B. DiMento, A. Schartup, R. Greene, and R. Mason, 2016: Seasonal Cycling and Transport of Mercury and Methylmercury in the Turbidity Maximum of the Delaware Estuary. *Aquatic Geochemistry*, **22**, 313–336.

Hammerschmidt, C. R. and W. F. Fitzgerald, 2006: Methylmercury cycling in sediments on the continental shelf of southern New England. *Geochimica et Cosmochimica Acta*, **70**, 918–930.

Hattermann, T., P. E. Isachsen, W.-J. von Appen, J. Albretsen, and A. Sundfjord, 2016: Eddy-driven recirculation of Atlantic Water in Fram Strait. *Geophysical Research Letters*, **43**, 3406–3414, doi: 10.1002/2016GL068323.

Hattermann, T., O. A. Nst, J. M. Lilly, and L. H. Smedsrud, 2012: Two years of oceanic observations below the Fimbul Ice Shelf, Antarctica. *Geophysical Research Letters*, **39**, 1–6.

Hawkings, J. R., B. S. Linhoff, J. L. Wadham, M. Stibal, C. H. Lamborg, G. T. Carling, G. Lamarche-Gagnon, T. J. Kohler, R. Ward, K. R. Hendry, L. Falteisek, A. M. Kellerman, K. A. Cameron, J. E. Hatton, S. Tingey, A. D. Holt, P. Vinšová, S. Hofer, M. Bulínová, T. Větrovský, L. Meire, and R. G. Spencer, 2021: Large subglacial source of mercury from the southwestern margin of the Greenland Ice Sheet. *Nature Geoscience*, **14**, 496–502.

Hawkings, J. R., M. L. Skidmore, J. L. Wadham, J. C. Priscu, P. L. Morton, J. E. Hatton, C. B. Gardner, T. J. Kohler, M. Stibal, E. A. Bagshaw, A. Steigmeyer, J. Barker, J. E. Dore, W. B. Lyons, M. Tranter, R. G. M. Spencer, and the SALSA Science Team, 2020: Enhanced trace element mobilization by Earths ice sheets. *Proceedings of the National Academy of Sciences*, **117**, 31648–31659.

Hellmer, H. H., S. S. Jacobs, and A. Jenkins, 1998: Oceanic Erosion of a Floating Antarctic Glacier in the Amundsen Sea.

Hester, E. W., C. D. McConnochie, C. Cenedese, L.-A. Couston, and G. Vasil, 2021: Aspect ratio affects iceberg melting. *Physical Review Fluids*, **6**, 23802.

Hill, E. A., J. R. Carr, C. R. Stokes, and G. H. Gudmundsson, 2018: Dynamic changes in outlet glaciers in northern Greenland from 1948 to 2015. *The Cryosphere*, **12**, 3243–3263.

Holland, D. M. and A. Jenkins, 1999: Modeling Thermodynamic Ice–Ocean Interactions at the Base of an Ice Shelf. *Journal of Physical Oceanography*, **29**, 1787–1800, doi: 10.1175/1520-0485(1999)0292.0.CO;2.

Holland, D. M., R. H. Thomas, B. de Young, M. H. Ribergaard, and B. Lyberth, 2008a: Acceleration of Jakobshavn Isbræ triggered by warm subsurface ocean waters. *Nature Geoscience*, **1**, 659–664.

Holland, P. R., 2017: The Transient Response of Ice Shelf Melting to Ocean Change. *Journal of Physical Oceanography*, **47**, 2101–2114.

Holland, P. R., A. Jenkins, and D. M. Holland, 2008b: The Response of Ice Shelf Basal Melting to Variations in Ocean Temperature. *Journal of Climate*, **21**, 2558–2572, doi: 10.1175/2007JCLI1909.1.

Hopwood, M. J., D. P. Connelly, K. E. Arendt, T. Juul-Pedersen, M. C. Stinchcombe, L. Meire, M. Esposito, and R. Krishna, 2016: Seasonal changes in Fe along a glaciated Greenlandic fjord. *Frontiers in Earth Science*, **4**.

Huppert, H. E. and J. S. Turner, 1980: Ice blocks melting into a salinity gradient. *Journal of Fluid Mechanics*, **100**, 367–384.

Håvik, L., R. S. Pickart, K. Våge, D. Torres, A. M. Thurnherr, A. Beszczynska-Möller, W. Walczowski, and W. J. von Appen, 2017: Evolution of the East Greenland Current from Fram Strait to Denmark Strait: Synoptic measurements from summer 2012. *Journal of Geophysical Research: Oceans*, **122**, 1974–1994.

Jackson, R. H., J. D. Nash, C. Kienholz, D. A. Sutherland, J. M. Amundson, R. J. Motyka, D. Winters, E. Skyllingstad, and E. C. Pettit, 2020: Meltwater Intrusions Reveal Mechanisms for Rapid Submarine Melt at a Tidewater Glacier. *Geophysical Research Letters*, **47**, e2019GL085335, doi: 10.1029/2019GL085335.

Jackson, R. H. and F. Straneo, 2016: Heat, salt, and freshwater budgets for a glacial fjord in Greenland. *Journal of Physical Oceanography*, **46**, 2735–2768.

Jackson, R. H., F. Straneo, and D. A. Sutherland, 2014: Externally forced fluctuations in ocean temperature at Greenland glaciers in non-summer months. *Nature Geoscience*, **7**, 503–508.

Jenkins, A., 1999: The impact of melting ice on ocean waters. *Journal of Physical Oceanography*, **29**, 2370 – 2381.

—, 2011: Convection-Driven Melting near the Grounding Lines of Ice Shelves and Tidewater Glaciers. *Journal of Physical Oceanography*, **41**, 2279–2294.

Jenkins, A., K. W. Nicholls, and H. F. J. Corr, 2010: Observation and Parameterization of Ablation at the Base of Ronne Ice Shelf, Antarctica. *Journal of Physical Oceanography*, **40**, 2298–2312.

Johnson, H. L., A. Münchow, K. K. Falkner, and H. Melling, 2011: Ocean circulation and properties in Petermann Fjord, Greenland. *Journal of Geophysical Research: Oceans*, **116**, 1–18.

Jordan, J. R., P. R. Holland, A. Jenkins, M. D. Piggott, and S. Kimura, 2014: Modeling ice-ocean interaction in ice-shelf crevasses. *Journal of Geophysical Research: Oceans*, **119**, 995–1008, doi: 10.1002/2013JC009208.

Josberger, E. G. and S. Neshyba, 1980: Iceberg melt-driven convection inferred from field measurements of temperature. *Annals of Glaciology*, **1**, 113–117.

Joughin, I., B. E. Smith, D. E. Shean, and D. Floricioiu, 2014: Brief Communication: Further summer speedup of Jakobshavn Isbræ. *The Cryosphere*, **8**, 209–214.

Kanna, N., S. Sugiyama, Y. Fukamachi, D. Nomura, and J. Nishioka, 2020: Iron Supply by Subglacial Discharge Into a Fjord Near the Front of a Marine-Terminating Glacier in Northwestern Greenland. *Global Biogeochemical Cycles*, **34**.

Kerr, R. C. and C. D. McConnochie, 2015: Dissolution of a vertical solid surface by turbulent compositional convection. *Journal of Fluid Mechanics*, **765**, 211–228.

Khan, S. A., K. H. Kjær, M. Bevis, J. L. Bamber, J. Wahr, K. K. Kjeldsen, A. A. Bjørk, N. J. Korsgaard, L. A. Stearns, M. R. van den Broeke, L. Liu, N. K. Larsen, and I. S. Muresan, 2014: Sustained mass loss of the northeast Greenland ice sheet triggered by regional warming. *Nature Climate Change*, **4**, 292–299.

King, M. D., I. M. Howat, S. G. Candela, M. J. Noh, S. Jeong, B. P. Y. Noël, M. R. van den Broeke, B. Wouters, and A. Negrete, 2020: Dynamic ice loss from the Greenland Ice Sheet driven by sustained glacier retreat. *Communications Earth and Environment*, **1**.

Krause, J., M. J. Hopwood, J. Höfer, S. Krisch, E. P. Achterberg, E. Alarcón, D. Carroll, H. E. González, T. Juul-Pedersen, T. Liu, P. Lodeiro, L. Meire, and M. T. Rosing, 2021: Trace Element (Fe, Co, Ni and Cu) Dynamics Across the Salinity Gradient in Arctic and Antarctic Glacier Fjords. *Frontiers in Earth Science*, **9**.

Lamborg, C. H., C. R. Hammerschmidt, and K. L. Bowman, 2016: An examination of the role of particles in oceanic mercury cycling. *Philosophical Transactions of the Royal Society A: Mathematical, Physical and Engineering Sciences*, **374**.

Langley, K., J. Kohler, A. Sinisalo, M. J. Øyan, S. E. Hamran, T. Hattermann, K. Matsuoka, O. A. Nøst, and E. Isaksson, 2014: Low melt rates with seasonal variability at the base of Fimbul Ice Shelf, East Antarctica, revealed by in situ interferometric radar measurements. *Geophysical Research Letters*, **41**, 8138–8146, doi: 10.1002/2014GL061782.

Lavoie, R. A., T. D. Jardine, M. M. Chumchal, K. A. Kidd, and L. M. Campbell, 2013: Biomagnification of mercury in aquatic food webs: A worldwide meta-analysis. *Environmental Science and Technology*, **47**, 13385–13394.

Le Bras, I. A.-A., F. Straneo, J. Holte, and N. P. Holliday, 2018: Seasonality of Freshwater in the East Greenland Current System From 2014 to 2016. *Journal of Geophysical Research: Oceans*, **123**, 8828–8848.

Leppi, J. C., C. D. Arp, and M. S. Whitman, 2016: Predicting Late Winter Dissolved Oxygen Levels in Arctic Lakes Using Morphology and Landscape Metrics. *Environmental Management*, **57**, 463–473.

Lerczak, J. A., W. R. Geyer, and R. J. Chant, 2006: Mechanisms Driving the Time-Dependent Salt Flux in a Partially Stratified Estuary. *Journal of Physical Oceanography*, **36**, 2296–2311, doi: 10.1175/JPO2959.1.

MacFerrin, M., H. Machguth, D. van As, C. Charalampidis, C. M. Stevens, A. Heilig, B. Vandecrux, P. L. Langen, R. Mottram, X. Fettweis, M. R. van den Broeke, W. T. Pfeffer, M. S. Moussavi, and W. Abdalati, 2019: Rapid expansion of Greenland's low-permeability ice slabs. *Nature*, **573**, 403–407.

Magorrian, S. J. and A. J. Wells, 2016: Turbulent plumes from a glacier terminus melting in a stratified ocean. *Journal of Geophysical Research: Oceans*, **121**, 4670–4696, doi: 10.1002/2015JC011160.

Marnela, M., B. Rudels, M.-N. Houssais, A. Beszczynska-Möller, and P. B. Eriksson, 2013: Recirculation in the Fram Strait and transports of water in and north of the Fram Strait derived from CTD data. *Ocean Science*, **9**, 499–519.

Martinerie, P., D. Raynaud, D. M. Etheridge, J.-M. Barnola, and D. Mazaudier, 1992: Physical and climatic parameters which influence the air content in polar ice. *Earth and Planetary Science Letters*, **112**, 1–13.

Mason, R. P., W. F. Fitzgerald, J. Hurley, A. K. Hanson, P. L. Donaghay, and J. M. Sieburth, 1993: Mercury biogeochemical cycling in a stratified estuary. *Limnol. Oceanogr*, **38**, 1227–1241.

Mawji, E., R. Schlitzer, E. M. Dodas, C. Abadie, W. Abouchami, R. F. Anderson, O. Baars, K. Bakker, M. Baskaran, N. R. Bates, K. Bluhm, A. Bowie, J. Bown, M. Boye, E. A. Boyle, P. Branellec, K. W. Bruland, M. A. Brzezinski, E. Bucciarelli, K. Buesseler, E. Butler, P. Cai, D. Cardinal, K. Casciotti, J. Chaves, H. Cheng, F. Chever, T. M. Church, A. S. Colman, T. M. Conway, P. L. Croot, G. A. Cutter, H. J. W. de Baar, G. F. de Souza, F. Dehairs, F. Deng, H. T. Dieu, G. Dulaquais, Y. Echegoyen-Sanz, R. L. Edwards, E. Fahrbach, J. Fitzsimmons, M. Fleisher, M. Frank, J. Friedrich, F. Fripiat, S. J. G. Galer, T. Gamo, E. G. Solsona, L. J. A. Gerringa, J. M. Godoy, S. Gonzalez, E. Grossteffan, M. Hatta, C. T. Hayes, M. I. Heller, G. Henderson, K.-F. Huang, C. Jeandel, W. J. Jenkins, S. John, T. C. Kenna, M. Klunder, S. Kretschmer, Y. Kumamoto, P. Laan, M. Labatut, F. Lacan, P. J. Lam, D. Lannuzel, F. le Moigne, O. J. Lechtenfeld, M. C. Lohan, Y. Lu, P. Masqué, C. R. McClain, C. Measures, R. Middag, J. Moffett, A. Navidad, J. Nishioka, A. Noble, H. Obata, D. C. Ohnemus, S. Owens, F. Planchon, C. Pradoux, V. Puigcorbé, P. Quay, A. Radic, M. Rehkämper, T. Remenyi, M. J. A. Rijkenberg, S. Rintoul, L. F. Robinson, T. Roeske, M. Rosenberg, M. R. van der Loeff, E. Ryabenko, M. A. Saito, S. Roshan, L. Salt, G. Sarthou, U. Schauer, P. Scott, P. N. Sedwick, L. Sha, A. M. Shiller, D. M. Sigman, W. Smethie, G. J. Smith, Y. Sohrin, S. Speich, T. Stichel, J. Stutsman, J. H. Swift, A. Tagliabue, A. Thomas, U. Tsunogai, B. S. Twining, H. M. van Aken, S. van Heuven, J. van Ooijen, E. van Weerlee, C. Venchiarutti, A. H. L. Voelker, B. Wake, M. J. Warner, E. M. S. Woodward, J. Wu, N. Wyatt, H. Yoshikawa, X.-Y. Zheng, Z. Xue, M. Zieringer, and L. A. Zimmer, 2015: The GEOTRACES Intermediate Data Product 2014. *Marine Chemistry*, **177**, 1–8.

Mayer, C., N. Reeh, F. Jung-Rothenhäusler, P. Huybrechts, and H. Oerter, 2000: The subglacial cavity and implied dynamics under Nioghalvfjerdsfjorden Glacier, NE-Greenland. *Geophysical Research Letters*, **27**, 2289–2292, doi: 10.1029/2000GL011514.

Mayer, C., J. Schaffer, T. Hattermann, D. Floricioiu, L. Krieger, P. A. Dodd, T. Kanzow, C. Licciulli, and C. Schannwell, 2018: Large ice loss variability at Nioghalvfjerdsfjorden Glacier, Northeast-Greenland. *Nature Communications*, **9**, 2768.

McConnochie, C. D. and R. C. Kerr, 2017: Testing a common ice-ocean parameterization with laboratory experiments. *Journal of Geophysical Research: Oceans*, **122**, 5905–5915.

McDougall, T. J. and P. M. Barker, 2011: Getting started with TEOS-10 and the Gibbs Seawater (GSW) Oceanographic Toolbox.

Meire, L., J. Mortensen, P. Meire, T. Juul-Pedersen, M. K. Sejr, S. Rysgaard, R. Nygaard, P. Huybrechts, and F. J. Meysman, 2017: Marine-terminating glaciers sustain high productivity in Greenland fjords. *Global Change Biology*, **23**, 5344–5357.

Meroni, A. N., C. D. McConnochie, C. Cenedese, B. Sutherland, and K. Snow, 2019: Nonlinear influence of the Earth's rotation on iceberg melting. *Journal of Fluid Mechanics*, **858**, 832–851.

Millgate, T., P. R. Holland, A. Jenkins, and H. L. Johnson, 2013: The effect of basal channels on oceanic ice-shelf melting. *Journal of Geophysical Research: Oceans*, **118**, 6951–6964.

Moon, T., D. A. Sutherland, D. Carroll, D. Felikson, L. Kehrl, and F. Straneo, 2018: Subsurface iceberg melt key to Greenland fjord freshwater budget. *Nature Geoscience*, **11**, 49–54.

Morlighem, M., E. Rignot, J. Mouginot, H. Seroussi, and E. Larour, 2014: Deeply incised submarine glacial valleys beneath the Greenland ice sheet. *Nature Geoscience*, **7**, 418–422.

Morlighem, M., C. Williams, E. Rignot, L. An, J. E. Arndt, J. L. Bamber, G. Catania, N. Chauché, J. A. Dowdeswell, B. Dorschel, I. Fenty, K. Hogan, I. Howat, A. Hubbard, M. Jakobsson, T. M. Jordan, K. K. Kjeldsen, R. Millan, L. Mayer, J. Mouginot, B. P. Y. Noël, C. O'Cofaigh, S. Palmer, S. Rysgaard, H. Seroussi, M. J. Siegert, P. Slabon, F. Straneo, M. R. van den Broeke, W. Weinrebe, M. Wood, and K. B. Zinglersen, 2017a: BedMachine v3: Complete Bed Topography and Ocean Bathymetry Mapping of Greenland From Multibeam Echo Sounding Combined With Mass Conservation. *Geophysical Research Letters*, 11051–11061.

—, 2017b: IceBridge BedMachine Greenland, Version 3.

Morton, B. R., G. I. Taylor, and J. S. Turner, 1956: Turbulent gravitational convection from maintained and instantaneous sources. *Proceedings of the Royal Society of London. Series A. Mathematical and Physical Sciences*, **234**, 1–23.

Motyka, R. J., M. Truffer, M. Fahnestock, J. Mortensen, S. Rysgaard, and I. Howat, 2011: Submarine melting of the 1985 Jakobshavn Isbræ floating tongue and the triggering of the current retreat. *Journal of Geophysical Research: Earth Surface*, **116**, doi: 10.1029/2009JF001632.

Mouginot, J., E. Rignot, A. A. Bjørk, M. van den Broeke, R. Millan, M. Morlighem, B. Noël, B. Scheuchl, and M. Wood, 2019: Forty-six years of Greenland Ice Sheet mass balance from 1972 to 2018. *Proceedings of the National Academy of Sciences*, **116**, 9239 LP – 9244.

Mouginot, J., E. Rignot, B. Scheuchl, I. Fenty, A. Khazendar, M. Morlighem, A. Buzzi, and J. Paden, 2015: Fast retreat of Zachariæ Isstrøm, northeast Greenland. *Science*, **350**, 1357 LP – 1361.

Moyer, A. N., D. A. Sutherland, P. W. Nienow, and A. J. Sole, 2019: Seasonal Variations in Iceberg Freshwater Flux in Sermilik Fjord, Southeast Greenland From Sentinel-2 Imagery. *Geophysical Research Letters*, **0**.

Mugford, R. I. and J. A. Dowdeswell, 2011: Modeling glacial meltwater plume dynamics and sedimentation in high-latitude fjords. *Journal of Geophysical Research: Earth Surface*, **116**.

Munson, K. M., D. Babi, and C. H. Lamborg, 2014: Determination of monomethylmercury from seawater with ascorbic acid-assisted direct ethylation. *Limnology and Oceanography: Methods*, **12**, 1–9.

Muntjewerf, L., M. Petrini, M. Vizcaino, C. da Silva, R. Sellevold, M. D. W. Scherrenberg, K. Thayer-Calder, S. L. Bradley, J. T. M. Lenaerts, W. H. Lipscomb, and M. Lofverstrom, 2020: Greenland Ice Sheet Contribution to 21st Century Sea Level Rise as Simulated by the Coupled CESM2.1-CISM2.1. *Geophysical Research Letters*, **47**, e2019GL086836, e2019GL086836 10.1029/2019GL086836.

Münchow, A., L. Padman, and H. A. Fricker, 2014: Interannual changes of the floating ice shelf of Petermann Gletscher, North Greenland, from 2000 to 2012. *Journal of Glaciology*, **60**, 489–499.

Münchow, A., J. Schaffer, and T. Kanzow, 2020: Ocean Circulation Connecting Fram Strait to Glaciers off Northeast Greenland: Mean Flows, Topographic Rossby Waves, and Their Forcing. *Journal of Physical Oceanography*, **50**, 509–530.

Noël, B., W. J. van de Berg, J. M. van Wessem, E. van Meijgaard, D. van As, J. T. M. Lenaerts, S. Lhermitte, P. K. Munneke, C. J. P. P. Smeets, L. H. van Ulft, R. S. W. van de Wal, and M. R. van den Broeke, 2018: Modelling the climate and surface mass balance of polar ice sheets using RACMO2 – Part 1: Greenland (1958 – 2016). *The Cryosphere*, **12**, 811–831.

Oltmanns, M., F. Straneo, G. W. Moore, and S. H. Mernild, 2014: Strong downslope wind events in Ammassalik, Southeast Greenland. *Journal of Climate*, **27**, 977–993.

Padman, L., M. R. Siegfried, and H. A. Fricker, 2018: Ocean Tide Influences on the Antarctic and Greenland Ice Sheets. *Reviews of Geophysics*, **56**, 142–184, doi: 10.1002/2016RG000546.

Pawlowicz, R., B. Beardsley, and S. Lentz, 2002: Classical tidal harmonic analysis including error estimates in MATLAB using T_TIDE. *Computers and Geosciences*, **28**, 929–937.

Pickhardt, P. C. and N. S. Fisher, 2007: Accumulation of inorganic and methylmercury by freshwater phytoplankton in two contrasting water bodies. *Environmental Science and Technology*, **41**, 125–131.

Reeh, N., H. H. Thomsen, A. K. Higgins, and A. Weidick, 2001: Sea ice and the stability of north and northeast Greenland floating glaciers. *Annals of Glaciology*, **33**, 474–480.

Rezvanbehbahani, S., L. A. Stearns, R. Keramati, S. Shankar, and C. J. van der Veen, 2020: Significant contribution of small icebergs to the freshwater budget in Greenland fjords. *Communications Earth and Environment*, **1**.

Rosevear, M. G., G. Bishakhdatta, and G.-F. B. Keith, 2021a: The role of double-diffusive convection in basal melting of Antarctic ice shelves. *Proceedings of the National Academy of Sciences*, **118**, e2007541118, doi: 10.1073/pnas.2007541118.

Rosevear, M. G., B. K. Galton-Fenzi, and C. Stevens, 2021b: Evaluation of basal melting parameterisations using in situ ocean and melting observations from the Amery Ice Shelf, East Antarctica. *Ocean Science Discussions*, **2021**, 1–31.

Sanchez, R., F. Straneo, and M. Andres, 2021: Using Acoustic Travel Time to Monitor the Heat Variability of Glacial Fjords. *Journal of Atmospheric and Oceanic Technology*, **38**, 1535–1550.

Schaffer, J., T. Kanzow, W.-J. von Appen, L. von Albedyll, J. E. Arndt, and D. H. Roberts, 2020: Bathymetry constrains ocean heat supply to Greenland's largest glacier tongue. *Nature Geoscience*, **13**, 227–231.

Schaffer, J. and C. Mayer, 2018: Physical oceanography during NE-Greenland expeditions 1997/98.

Schaffer, J., W. J. von Appen, P. A. Dodd, C. Hofstede, C. Mayer, L. de Steur, and T. Kanzow, 2017: Warm water pathways toward Nioghalvfjerdsfjorden Glacier, Northeast Greenland. *Journal of Geophysical Research: Oceans*, **122**, 4004–4020.

Schaffer, J., W.-J. von Appen, and T. Kanzow, 2019: Physical oceanography and current meter data from mooring 79N1-1 at the continental shelf off Northeast Greenland.

Schartup, A. T., R. P. Mason, P. H. Balcom, T. A. Hollweg, and C. Y. Chen, 2013: Methylmercury production in estuarine sediments: Role of organic matter. *Environmental Science and Technology*, **47**, 695–700.

Schartup, A. T., A. Qureshi, C. Dassuncao, C. P. Thackray, G. Harding, and E. M. Sunderland, 2018: A Model for Methylmercury Uptake and Trophic Transfer by Marine Plankton. *Environmental Science and Technology*, **52**, 654–662.

Schartup, A. T., A. L. Soerensen, and L. E. Heimbürger-Boavida, 2020: Influence of the Arctic Sea-Ice Regime Shift on Sea-Ice Methylated Mercury Trends. *Environmental Science and Technology Letters*, **7**, 708–713.

Schild, K. M., D. A. Sutherland, P. Elosegui, and D. Duncan, 2021: Measurements of Iceberg Melt Rates Using High-Resolution GPS and Iceberg Surface Scans. *Geophysical Research Letters*, **48**, e2020GL089765, e2020GL089765 2020GL089765.

Selin, N. E., 2009: Global biogeochemical cycling of mercury: A review. *Annual Review of Environment and Resources*, **34**, 43–63.

Slater, D. A., D. N. Goldberg, P. W. Nienow, and T. R. Cowton, 2016: Scalings for Submarine Melting at Tidewater Glaciers from Buoyant Plume Theory. *Journal of Physical Oceanography*, **46**, 1839–1855.

Slater, D. A., P. W. Nienow, D. N. Goldberg, T. R. Cowton, and A. J. Sole, 2017: A model for tidewater glacier undercutting by submarine melting. *Geophysical Research Letters*, **44**, 2360–2368, doi: 10.1002/2016GL072374.

Slater, D. A., F. Straneo, D. Felikson, C. M. Little, H. Goelzer, X. Fettweis, and J. Holte, 2019: Estimating Greenland tidewater glacier retreat driven by submarine melting. *The Cryosphere*, **13**, 2489–2509.

Smith, B., H. A. Fricker, A. S. Gardner, B. Medley, J. Nilsson, F. S. Paolo, N. Holschuh, S. Adusumilli, K. Brunt, B. Csatho, K. Harbeck, T. Markus, T. Neumann, M. R. Siegfried, and H. J. Zwally, 2020: Pervasive ice sheet mass loss reflects competing ocean and atmosphere processes. *Science*, **368**, 1239–1242.

Smith, K. L., A. D. Sherman, T. J. Shaw, and J. Sprintall, 2013: Icebergs as Unique Lagrangian Ecosystems in Polar Seas. *Annual Review of Marine Science*, **5**, 269–287, pMID: 22809193.

Sneed, W. A. and G. S. Hamilton, 2016: Recent changes in the Norske Oer Ice Barrier, coastal Northeast Greenland. *Annals of Glaciology*, **57**, 47–55.

Soerensen, A. L., D. J. Jacob, A. T. Schartup, J. A. Fisher, I. Lehnherr, V. L. S. Louis, L. E. Heimbürger, J. E. Sonke, D. P. Krabbenhoft, and E. M. Sunderland, 2016: A mass budget for mercury and methylmercury in the Arctic Ocean. *Global Biogeochemical Cycles*, **30**, 560–575.

Stanton, T. P., W. J. Shaw, M. Truffer, H. F. J. Corr, L. E. Peters, K. L. Riverman, R. Bindschadler, D. M. Holland, and S. Anandakrishnan, 2013: Channelized Ice Melting in the Ocean Boundary Layer Beneath Pine Island Glacier, Antarctica. *Science*, **341**, 1236–1239.

Stephenson, G. R., J. Sprintall, S. T. Gille, M. Vernet, J. J. Helly, and R. S. Kaufmann, 2011: Subsurface melting of a free-floating Antarctic iceberg. *Deep Sea Research Part II: Topical Studies in Oceanography*, **58**, 1336–1345.

Stern, G. A., R. W. Macdonald, P. M. Outridge, S. Wilson, J. Chételat, A. Cole, H. Hintelmann, L. L. Loseto, A. Steffen, F. Wang, and C. Zdanowicz, 2012: How does climate change influence arctic mercury?

Stevens, C., C. Hulbe, M. Brewer, C. Stewart, N. Robinson, C. Ohneiser, and S. Jendersie, 2020: Ocean mixing and heat transport processes observed under the Ross Ice Shelf control its basal melting. *Proceedings of the National Academy of Sciences*, **117**, 16799 LP – 16804.

Stewart, C. L., P. Christoffersen, K. W. Nicholls, M. J. M. Williams, and J. A. Dowdeswell, 2019: Basal melting of Ross Ice Shelf from solar heat absorption in an ice-front polynya. *Nature Geoscience*, **12**, 435–440.

Straneo, F., 2020: Water temperature and salinity taken by CTD and XBT from vessel Arctic Sunrise in Kangerdlugssuaq Fjord and Nioghalvfjerdsfjorden, Greenland, from 2009-08-28 to 2009-09-08 (NCEI Accession 0210954).

Straneo, F. and C. Cenedese, 2015: The Dynamics of Greenland's Glacial Fjords and Their Role in Climate. *Annual Review of Marine Science*, **7**, 89–112.

Straneo, F., R. G. Curry, D. A. Sutherland, G. S. Hamilton, C. Cenedese, K. Våge, and L. A. Stearns, 2011: Impact of fjord dynamics and glacial runoff on the circulation near Helheim Glacier. *Nature Geoscience*, **4**, 322–327.

Straneo, F., G. S. Hamilton, L. A. Stearns, and D. A. Sutherland, 2016: Connecting the Greenland Ice Sheet and the ocean: A case study of Helheim Glacier and Sermilik Fjord. *Oceanography*, **29**, 34–45.

Straneo, F., G. S. Hamilton, D. A. Sutherland, L. A. Stearns, F. Davidson, M. O. Hammill, G. B. Stenson, and A. Rosing-Asvid, 2010: Rapid circulation of warm subtropical waters in a major glacial fjord in East Greenland. *Nature Geoscience*, **3**, 182–186.

Straneo, F., P. Heimbach, O. Sergienko, G. Hamilton, G. Catania, S. Griffies, R. Hallberg, A. Jenkins, I. Joughin, R. Motyka, W. T. Pfeffer, S. F. Price, E. Rignot, T. Scambos, M. Truffer, and A. Vieli, 2013: Challenges to Understanding the Dynamic Response of Greenland's Marine Terminating Glaciers to Oceanic and Atmospheric Forcing. *Bulletin of the American Meteorological Society*, **94**, 1131–1144.

Straneo, F., D. A. Sutherland, D. Holland, C. Gladish, G. S. Hamilton, H. L. Johnson, E. Rignot, Y. Xu, and M. Koppes, 2012: Characteristics of ocean waters reaching

Greenland's glaciers. *Annals of Glaciology*, **53**, 202–210.

Straneo, F. and N. Wilson, 2020: Water temperature and salinity taken by expandable CTD from ice edge in Nioghalvfjerdsfjorden, Northeast Greenland, on 2016-08-23 (NCEI Accession 0210955).

Sulak, D. J., D. A. Sutherland, E. M. Enderlin, L. A. Stearns, and G. S. Hamilton, 2017: Iceberg properties and distributions in three Greenlandic fjords using satellite imagery. *Annals of Glaciology*, **58**, 92–106.

Sutherland, B. R., M. G. Rosevear, and C. Cenedese, 2020: Laboratory experiments modeling the transport and deposition of sediments by glacial plumes rising under an ice shelf. *Physical Review Fluids*, **5**.

Sutherland, D. A., R. H. Jackson, C. Kienholz, J. M. Amundson, W. P. Dryer, D. Duncan, E. F. Eidam, R. J. Motyka, and J. D. Nash, 2019: Direct observations of submarine melt and subsurface geometry at a tidewater glacier. *Science*, **365**, 369–374.

Sutherland, D. A. and R. S. Pickart, 2008: The East Greenland Coastal Current: Structure, variability, and forcing. *Progress in Oceanography*, **78**, 58–77.

Sutherland, D. A., G. E. Roth, G. S. Hamilton, S. H. Mernild, L. A. Stearns, and F. Straneo, 2014: Quantifying flow regimes in a Greenland glacial fjord using iceberg drifters. *Geophysical Research Letters*, **41**, 8411–8420, doi: 10.1002/2014GL062256.

Søndergaard, J., F. Rigét, M. P. Tamstorf, and M. M. Larsen, 2012: Mercury transport in a low-arctic river in Kobbefjord, West Greenland (64° N). *Water, Air, and Soil Pollution*, **223**, 4333–4342.

Søndergaard, J., M. Tamstorf, B. Elberling, M. M. Larsen, M. R. Mylius, M. Lund, J. Abermann, and F. Rigét, 2015: Mercury exports from a High-Arctic river basin in Northeast Greenland (74°N) largely controlled by glacial lake outburst floods. *Science of the Total Environment*, **514**, 83–91.

Tabone, I., A. Robinson, J. Alvarez-Solas, and M. Montoya, 2019: Submarine melt as a potential trigger of the North East Greenland Ice Stream margin retreat during Marine Isotope Stage 3. *The Cryosphere*, **13**, 1911–1923.

Tomczak, M., 1981: A multi-parameter extension of temperature/salinity diagram techniques for the analysis of non-isopycnal mixing. *Progress in Oceanography*, **10**, 147–171.

Toole, J. M., R. Krishfield, and W. H. O. I. I.-T. P. Program, 2016: Oceanographic profile observations collected from station ITM-5 by Woods Hole Oceanographic Institution (WHOI) in the 79 North Glacier, Greenland, from 2016-08-23 to 2018-12-22 (NCEI

Accession 0157557).

US Environmental Protection Agency, 1998: Method 1630, Methyl mercury in water by distillation, aqueous ethylation, purge and trap, and cold vapor atomic fluorescence spectrometry.

—, 2002: Method 1631, Revision E: Mercury in water by oxidation, purge and trap, and cold vapor atomic fluorescence spectrometry.

Valle-Levinson, A., 2008: Density-driven exchange flow in terms of the Kelvin and Ekman numbers. *Journal of Geophysical Research: Oceans*, **113**.

von Storch, H. and F. W. Zwiers, 1999: Specific Statistical Concepts in Climate Research.

Våge, K., R. S. Pickart, A. Sarafanov, Øyvind Knutsen, H. Mercier, P. Lherminier, H. M. van Aken, J. Meincke, D. Quadfasel, and S. Bacon, 2011: The Irminger Gyre: Circulation, convection, and interannual variability. *Deep-Sea Research Part I: Oceanographic Research Papers*, **58**, 590–614.

Wadham, J. L., J. R. Hawkings, L. Tarasov, L. J. Gregoire, R. G. Spencer, M. Gutjahr, A. Ridgwell, and K. E. Kohfeld, 2019: Ice sheets matter for the global carbon cycle.

Wagner, T. J. W., R. W. Dell, and I. Eisenman, 2017: An Analytical Model of Iceberg Drift. *Journal of Physical Oceanography*, **47**, 1605–1616.

Washam, P., A. Münchow, and K. W. Nicholls, 2018: A Decade of Ocean Changes Impacting the Ice Shelf of Petermann Gletscher , Greenland. *Journal of Physical Oceanography*, **48**, 2477–2493.

Washam, P., K. W. Nicholls, A. Münchow, and L. Padman, 2019: Summer surface melt thins Petermann Gletscher Ice Shelf by enhancing channelized basal melt. *Journal of Glaciology*, **65**, 662–674.

Wells, A. J. and M. G. Worster, 2008: A geophysical-scale model of vertical natural convection boundary layers. *Journal of Fluid Mechanics*, **609**, 111–137.

Wilson, N. J. and F. Straneo, 2015: Water exchange between the continental shelf and the cavity beneath Nioghalvfjerdsbræ (79 North Glacier). *Geophysical Research Letters*, **42**, 7648–7654.

Wilson, N. J., F. Straneo, and P. Heimbach, 2017: Satellite-derived submarine melt rates and mass balance (2011-2015) for Greenland's largest remaining ice tongues. *Cryosphere*, **11**, 2773–2782.

Yankovsky, A. E. and I. Yashayaev, 2014: Surface buoyant plumes from melting icebergs in the Labrador Sea. *Deep Sea Research Part I: Oceanographic Research Papers*, **91**, 1–9.

Zhao, K. X., A. L. Stewart, and J. C. McWilliams, 2019: Sill-Influenced Exchange Flows in Ice Shelf Cavities. *Journal of Physical Oceanography*, **49**, 163–191.